CHARGE STORAGE IN ORGANIC ELECTRODES FOR ENERGY & ELECTROCHEMICAL APPLICATIONS

A Dissertation

by

JU WON JEON

Submitted to the Office of Graduate and Professional Studies of
Texas A&M University
in partial fulfillment of the requirements for the degree of

DOCTOR OF PHILOSOPHY

Chair of Committee,	Jodie L. Lutkenhaus
Committee Members,	Perla Balbuena
	Jamie Grunlan
	Karen L. Wooley
Head of Department,	M. Nazmul Karim

December 2014

Major Subject: Chemical Engineering

ABSTRACT

Energy storage has been emerging as an important research topic because of the lack of fossil fuels and growing energy consumption. This thesis focuses on synthesis and characterization of electrode materials such as polyaniline, graphene, and nitrogen-doped porous carbon for use in energy storage applications.

Polyaniline (PANI), a conjugated polymer, has been widely investigated as an electrode material for energy storage. In order to enhance its oxidative stability, polyaniline:poly(2-acrylamido-2-methyl-1-propanesulfonic acid) (PANI:PAAMPSA) complex was synthesized using template polymerization. PANI:PAAMPSA possessed significantly increased oxidative stability up to 4.5 V (vs. Li/Li^+) due to electrostatic and hydrogen bonding interactions between PANI and PAAMPSA. This polyacid-doped PANI showed a reversible capacity of 230 mAh/g_{PANI} for over 800 cycles.

Three different polyaniline-based layer-by-layer (LbL) electrodes, PANI/PAAMPSA, PANI/PANI:PAAMPSA, and linear poly(ethylenimine)/PANI:PAAMPSA were fabricated and their charge storage natures were assessed in non-aqueous energy storage systems. PANI:PAAMPSA retained its oxidative stability within LbL electrodes. The PANI/PAAMPSA LbL electrode did not show enhanced oxidative stability as compared to PANI:PAAMPSA complexes, which indicates that the interactions between PANI and PAAMPSA are not as strong as in PANI:PAAMPSA complexes.

Porous PANI nanofiber/graphene hybrid electrodes were prepared by electrochemical reduction of PANI nanofiber/graphene oxide (PANI NF/GO) LbL assemblies at 1.5 V (vs. Li/Li^+). The limited processibility of reduced graphene oxide was circumvented by using GO to build up PANI NF/GO LbL films followed by electrochemical reduction. PANI NF/electrochemically reduced graphene oxide (ERGO) LbL electrodes show high capacity and enhanced cycling stability. Its performance is strongly dependent on electrode thickness.

Nitrogen-doped porous carbon was synthesized by one-step carbonization of isorecticular metal-organic frameworks (IRMOF-3). Porous IRMOF-3 itself acts as a self-sacrificial template to provide porous structure. Furthermore, additional carbon and nitrogen sources were not required. The nitrogen content can be easily controlled by varying carbonization temperature. Nitrogen-doped porous carbon possessed significantly higher capacitance due to additional pseudocapacitance originating from nitrogen as compared to analogous nitrogen-free porous carbons.

ACKNOWLEDGEMENTS

First of all, I would like to thank my advisor, Prof. Jodie L. Lutkenhaus for the guidance and support throughout the course of this research. It was a great opportunity for me to carry out research in Dr. Lutkenhaus‟s group. Without her help and support, I could not have conducted meaningful research. I would also like to thank my thesis committee members Prof. Perla Balbuena, Prof. Jaime Grunlan, and Prof. Karen Wooley for their interest and valuable advice. I also thank members of the Lutkenhaus group including Ajay Vidyasagar, Lu Zhang, Jared Mike, Lin Shao, Jing Zhou, Choonghyun Sung, Dariya Reid, Joe Puhr, Se Ra Kwon, Yanpu Zhang, Hyosung An, and Josh O‟Neal.

I would like to thank Dr. Satish Nune for giving me an opportunity to do summer and fall internships at Pacific Northwest National Laboratory. With his support and advice, I could conduct valuable research and extend my research scope. I thank Dr. Daiwon Choi for his help and support. I would also like to thank Dr. Radha Motkuri, Dr. Carlos Fernandez, Dr. Jian Liu, Dr. Peter McGrail, Dr. Daniel Gaspar, and Dr. Timothy Bays.

Finally, thanks to my family; my wife Hyunjoo Hong, my daughter Seohyun Jeon, my mother and father for their patience and love. I would like to give special thanks to my grandmother in heaven.

TABLE OF CONTENTS

Page

LIST OF FIGURES

Page

LIST OF TABLES

Page

CHAPTER I

INTRODUCTION

1.1 INTRODUCTORY REMARKS

Due to increasing energy consumption and lack of fossil fuels, energy has become one of the most important issues in the world.[1] In response to those challenges, great efforts have been made to develop more efficient energy storage systems as well as renewable energy conversion systems.[1, 2] This thesis deals with rechargeable energy storage systems, especially focusing on electrode materials.

This chapter introduces general concepts and working principles of commonly used energy storage systems, such as batteries, conventional capacitors, and electrochemical capacitors (also called supercapacitors). Several electrode materials and precursors including polyaniline (PANI), graphene, metal-organic frameworks (MOFs) used in this thesis are also introduced. The properties and characteristics of these materials are discussed for its potential use in energy storage. The layer-by-layer (LbL) assembly technique, one fabrication method for electrodes, is also discussed

1.2 ELECTROCHEMICAL ENERGY STORAGE

Global warming and pollution have become important and pressing issues over the last few decades. To mitigate these problems, the development of sustainable and renewable technologies is urgently required. The development of efficient energy storage systems is essential to achieve this goal and meet the requirement of future clean

technologies. For example, energy storage systems play crucial roles in hybrid electric vehicles, portable electronics, and even large industrial equipment.[3] Electrochemical energy storage systems can be classified into three different categories depending upon their energy storage mechanisms and performances; batteries, conventional capacitors, and electrochemical capacitors (also called supercapacitors).[2, 3] Batteries exhibit high energy density and a lower power density than capacitors.[3, 4] On the contrary, traditional capacitors can provide high power density although its energy density is low.[5] Electrochemical capacitors bridge the gap between batteries and capacitors; they possess higher power density than batteries, and higher energy density than conventional dielectric capacitors.[6]

1.2.1 BATTERIES

Lithium-ion batteries are among the most widely used electrochemical energy storage systems in portable electronics such as lap tops, cell phones, etc. due to their high energy density, and were commercialized by Sony in 1990.[1, 7] Lithium-ion batteries mainly consist of a cathode, an anode, and an electrolyte containing lithium salts.[7-9] A variety of materials have been examined as cathodes in lithium-ion batteries.

In Figure 1.1, various positive (cathode) and negative (anode) electrodes along with their performance metrics are illustrated.[10-14] Materials having a high redox potential are used as cathodes, whereas materials with low redox potential are used as anodes. Diverse metal oxides including lithium cobalt oxide, lithium manganese oxide, lithium iron phosphate, and vanadium oxide have been widely investigated as active

materials for cathodes. Among them, lithium cobalt oxide is dominantly used in commercial lithium-ion batteries.[15] In the case of anodes, a variety of materials including graphite, tin, and silicon have been studied.[14, 16] Even though lithium metal has the highest capacity, graphite is most commonly used as the anode due to its good intercalation properties and safety.[17] For the preparation of electrodes, active cathode materials are often mixed with a binder (e.g. polyvinylidene fluoride) and conductive additive (e.g. carbon black), and then coated onto a current collector.[15] As for the electrolyte, lithium salt such as $LiPF_6$ in a mixture of dimethyl carbonate and ethylene carbonate is widely used.[15] To prevent short circuits, separators such as polypropyelene carbonate are employed in lithium-ion battery cells.[7]

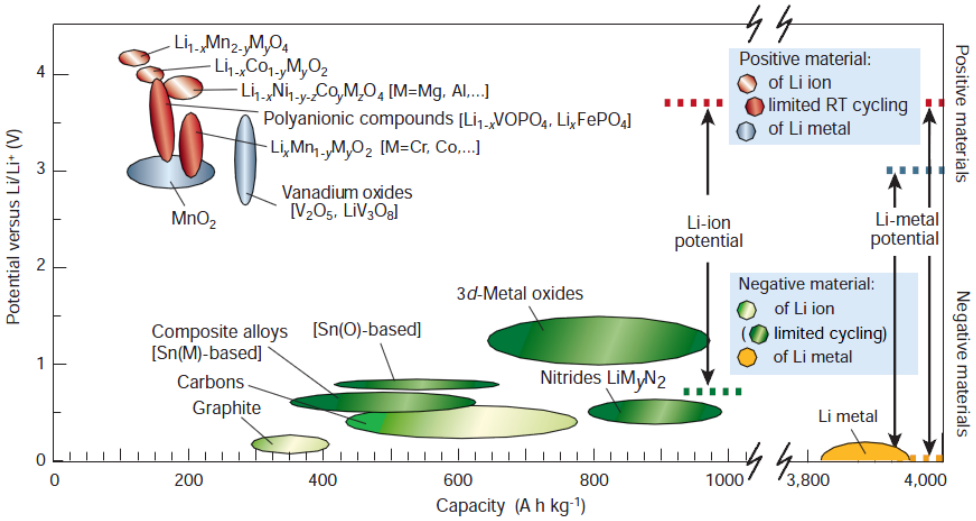

Figure 1.1. Various cathode and anode materials with their potential and capacity. Reproduced with permission.[16] Copyright 2001, Nature Publishing Group.

The schematic illustration of lithium ion batteries is represented in Figure 1.2. In order for a battery to work, the redox potential of a cathode should be higher than that of an anode. The reactions of a typical lithium cobalt oxide cathode and a graphite anode are shown in following equations:[18]

$$LiCoO_2 \underset{\text{Discharge}}{\overset{\text{Charge}}{\rightleftharpoons}} Li_{(1-x)}CoO_2 + xLi^+ + xe^- \quad (1.1)$$

$$Li_xC_6 + xLi^+ + xe^- \underset{\text{Discharge}}{\overset{\text{Charge}}{\rightleftharpoons}} LiC_6 \quad (1.2)$$

Overall:

$$LiCoO_2 + Li_xC_6 \underset{\text{Discharge}}{\overset{\text{Charge}}{\rightleftharpoons}} Li_{(1-x)}CoO_2 + LiC_6 \quad (1.3)$$

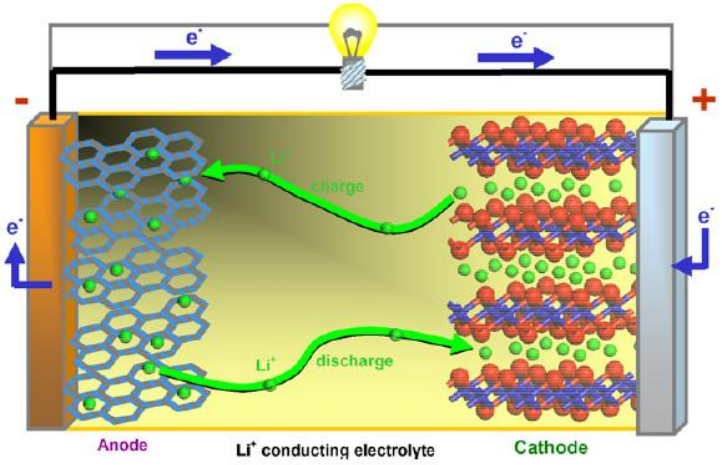

Figure 1.2. Schematic illustration of the discharge and charge processes of a lithium rechargeable battery. Reproduced with permission.[19] Copyright 2008, Elsevier.

During the discharge process, a cathode undergoes reduction, obtaining electrons and lithium ions while an anode is oxidized, losing electrons and lithium ions. These spontaneous processes enable the flow of electrons through the connected external circuit. On the contrary, when the battery is charged, a cathode is oxidized whereas an anode is reduced. During the charge and discharge processes, electrolyte provides and transfers lithium ions between the cathode and the anode.

1.2.2 CONVENTIONAL CAPACITORS

Conventional capacitors can deliver energy very quickly even if the amount of energy that can be delivered is small compared to batteries. The basic construction of conventional dielectric capacitors is depicted in Figure 1.3. Capacitors are traditionally composed of two parallel conducting electrodes separated by a dielectric material (insulator).[20] Typically, aluminum and aluminum oxide are used as the electrode and dielectric, respectively.[5] When a capacitor is connected to other power supplies such as batteries, electrons are accumulated on one electrode (a negative electrode).[21] As a consequence, the other electrode (a positive electrode) is deficient in electrons. In this manner, capacitors can store charge, which is capable of doing work. When this charged capacitor is disconnected to power supplies and connected to other equipment, electrons rapidly flow from a negative electrode (electron surplus) to a positive electrode (electron deficiency).[21]

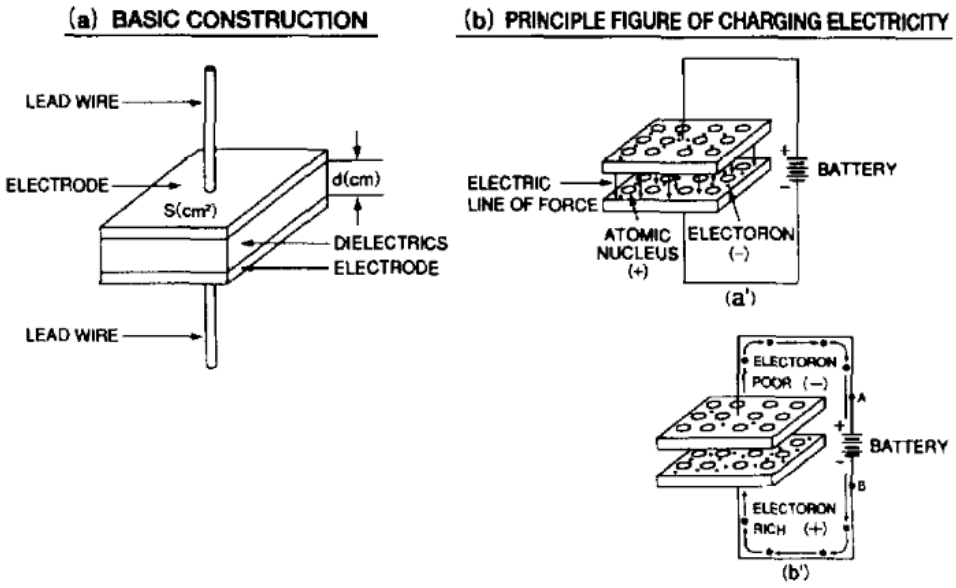

Figure 1.3. Basic construction of capacitors and their charging principles. Reproduced with permission.[21] Copyright 1996, Elsevier.

1.2.3 ELECTROCHEMICAL CAPACITORS (SUPERCAPACITORS)

Electrochemical capacitors, which can also be called supercapacitors, deliver more energy than traditional capacitors and their power is higher than batteries. They play important roles in complementing batteries in the energy storage field.[3] Supercapacitors can be used in consumer electronics, back-up power supplies, emergency doors, and even industrial power, providing safety and reliability.[3, 22] Supercapacitors can be divided into two different systems depending upon their charge storage mechanisms: electrical double layer capacitors (EDLCs) and pseudocapacitors.[3, 22, 23]

In EDLCs, energy is stored solely by adsorption of electrolyte ions onto the electrode surface.[24] A schematic diagram of EDLCs is depicted in Figure 1.4. It functions in a similar way to a conventional dielectric capacitor. When it connected to a power supply, charges are accumulated electrostatically in the electrodes, and each electrode is surrounded with its counter ions from the electrolyte. An ion-permeable separator is placed between electrodes to prevent a short circuit. In EDLCs, there is no Faradaic reaction involved.[3] Various carbon materials with a high surface area such as activated carbon, carbon black, carbon fiber, carbon nanotube, and graphene are used as electrode materials.[25-27] For electrolytes, both aqueous (e.g. H_2SO_4, HCl, KOH, NaCl etc.) and nonaqueous solutions (e.g. 1M tetraethylamonium teterafluoroborate in acetonitrile) can be used as the electrolyte solution.[25, 28]

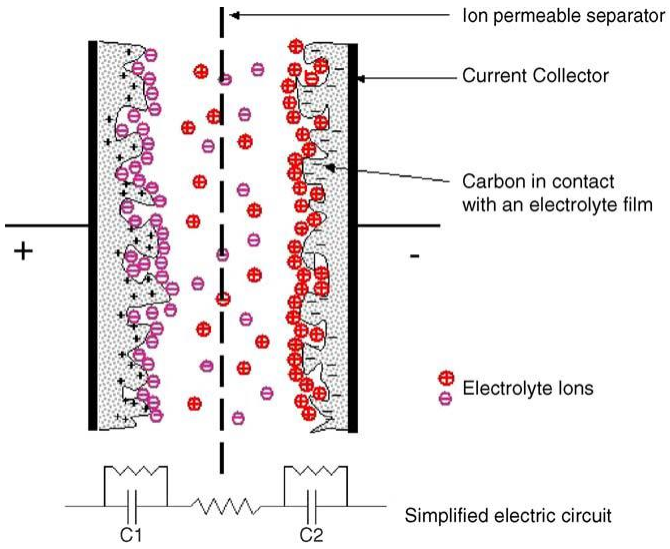

Figure 1.4. Schematic diagram of EDLC cells. Reproduced with permission.[25] Copyright 2006, Elsevier.

Some electrochemical capacitors utilize reversible oxidation and reduction reactions to store charge unlike EDLCs. This category of supercapacitor is called a "pseudocapacitor". While EDLCs store charge by physical adsorption of electrolyte ions on electrodes, pseudocapacitors directly participate in Faradaic reactions.[20] Pseudocapacitors can store more energy than EDLCs due to its chemical redox reaction. However, its cycling stability is not as good as EDLCs.[20] A variety of inorganic and organic materials can be utilized as electrode materials for pseudocapacitors. Among metal oxides, RuO_2 [29, 30], MnO_2 [31, 32], and Fe_3O_4 [33] are widely investigated as active electrode materials. In addition, various conducting polymers such as polyaniline,[34-36] polypyrrole,[35, 37] and poly(3,4-ethylenedioxythiophene)[38, 39] have been proposed due to their unique redox properties. For electrolytes, similarly, aqueous (e.g., H_2SO_4, KCl etc.) and nonaqueous electrolytes (e.g., $LiPF_6$ in ethylene carbonate/dimethyl carbonate) can be used. [40, 41, 20, 42, 43]

1.3 POLYANILINE

Polyaniline (PANI), a conjugated polymer, has been widely investigated in a variety of applications because of its good chemical stability, good conductivity, redox properties, and ease of synthesis.[44, 45] PANI can exist in five different oxidation states, which are pernigraniline base (PB), pernigraniline salt (PS), emeraldine base (EB), emeraldine salt (ES), and leucoemeraldine base (LB). These oxidation states are presented in Figure 1.5. Pernigraniline and emeraldine forms can exist as a salt or base depending upon its chemical environment. Pernigraniline is the fully oxidized form of PANI, and

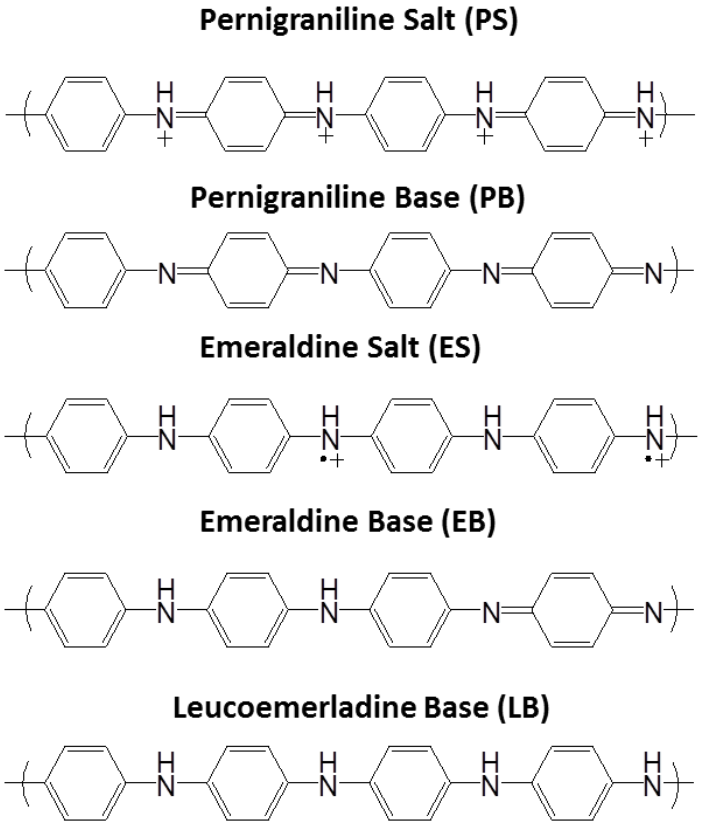

Figure 1.5. Oxidation states for PANI.

leucoemeraldine is the fully reduced form of PANI. Between pernigraniline and leucoemeraldine oxidation, there are ES and EB states which are half oxidized/half reduced.[44] Among them, the ES form is known to be conductive.[46]

PANI can be easily synthesized via conventional free radical polymerization method.[13, 46] As synthesized, PANI exists as conductive ES form with unreacted monomer, oligomer and other impurities from the initiator. Impurities can be removed using washing/filtration or dialysis.[13] Instead of irregularly shaped conventional PANI,

several methods were developed to synthesize one-dimensional PANI nanofibers.[47-49] Many research groups used additional templates to produce one-dimensional PANI nanofiber.[47-49] Dr. Kaner's group successfully synthesized PANI nanofibers without an additional template using interfacial polymerization.[50] In this method, they dissolved aniline monomer in organic solvents such as benzene and toluene.[50] Ammonium peroxydisulfate initiator was dissolved in water with acid.[50] When one solution was poured into the other, the two solutions were immiscible. Hence, the polymerization reaction only occurred at the water/organic interface.[50] Because the synthesized PANI nanofibers diffused into the water phase, secondary growth and aggregation of PANI were successfully suppressed.[50] As a result, PANI nanofibers were obtained. Afterwards, they also reported that PANI nanofibers can also be synthesized using rapid mixing.[51] When initiator was rapidly added to aniline monomer, many nucleation sites were created and all monomers were consumed, resulting in PANI nanofiber formation.[50]

PANI has also been extensively investigated as an electrode material in energy storage systems owing to its good electrochemical activity and relatively high conductivity.[20] In nonaqueous electrolytes, PANI showed a good capacity of 147 mAh/g and specific energy of 539.2 mWh/g.[46] However, PANI often suffers from poor cycle life above 3.5 V (vs. Li/Li^+).[13, 20, 52]

1.4 GRAPHENE

Graphene, a two dimensional monolayer graphitic carbon, has attracted significant interest since it was isolated from graphite in 2004.[53, 54] To date, graphene has

been extensively studied on account of its interesting properties such as its high modulus, electron mobility, thermal conductivity, chemical stability, and theoretical surface area (~2630 m^2/g).[55-58] There have been a number of studies on graphene for various applications, including field-effect transistors, memory devices, solar cells, energy storage, and sensors.[53, 57, 59-61]

Graphene has been synthesized through a variety of routes. In 2004, graphene was achieved from highly-oriented pyrolytic graphite through repeated mechanical exfoliation using tape.[53] Afterwards, it attracted great attention, and researchers suggested a number of methods to synthesize graphene. Graphene was also synthesized from carbon-containing gases such as methane or ethane on metal substrates, using chemical vapor deposition (CVD).[62-64] Thermal decomposition of silicon carbide (SiC) was also reported for production of graphene.[65, 66] Currently, a solution-based method is the most widely used procedure for large-scale synthesis.[67] In this method, graphite precursor was oxidized to graphite oxide using the Hummers method. Then, graphite oxide was exfoliated to graphene oxide via ultrasonication, and graphene oxide was converted to reduced graphene oxide (graphene) using hydrazine as a reducing agent.[67] This reduced graphene oxide can be dispersible in basic aqueous conditions because of remaining carboxylic acid groups.[67] To date, various chemical reducing agents including hydroiodic acid (HI), vitamin C, hydroquinone, and sodium borohydride ($NaBH_4$) were also demonstrated.[67, 69-71] To reduce graphene oxide to graphene, other reduction methods were also investigated such as photochemical reduction, thermal reduction, and electrochemical reduction.[72-74]

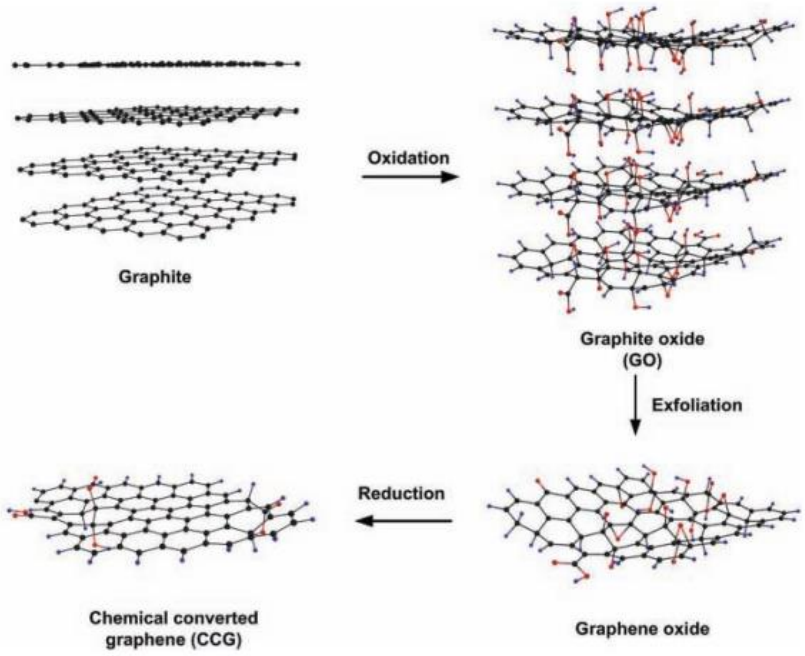

Figure 1.6. Preparation of chemically converted graphene by reduction of graphene oxide. Reproduced with permission.[68] Copyright, 2011, John Wiley and Sons.

1.5 METAL ORGANIC FRAMEWORKS

Metal organic frameworks (MOFs) are hybrid organic-inorganic materials, in which metal ions/clusters are connected with organic linkers.[75, 76] MOFs have become one of the most actively studied materials because of their interesting properties and a variety of advantages.[76] One of the strengths of MOFs is their versatility. Their properties such as pore size, shape, surface area, and functionality can be fine-tuned by combining various metal ions and organic linkers.[75, 77, 78] For example, pore size was successfully controlled by altering the ligand, leading to different gas storage

performances.[79] To date, hundreds of different MOFs with various structures have been synthesized and studied.[78, 80] Several different MOFs are displayed in Figure 1.7.[80]

Generally, MOFs are synthesized using simple solvothermal methods.[78] In a typical synthesis, metal salt and organic ligand are dissolved in a polar organic solvent. MOFs are synthesized by self-assembly of the metal precursor and ligand within a few hours.[78] During the synthesis, MOFs are crystallized and precipitated. Unreacted metal salts and ligands can be removed by filtering and washing.[78]

Due to their aforementioned advantages and diversity, there has been a tremendous effort to use MOFs in various applications including purification, catalysis, gas storage, and gas separation.[78, 81-84] MOFs were also used as a template to produce

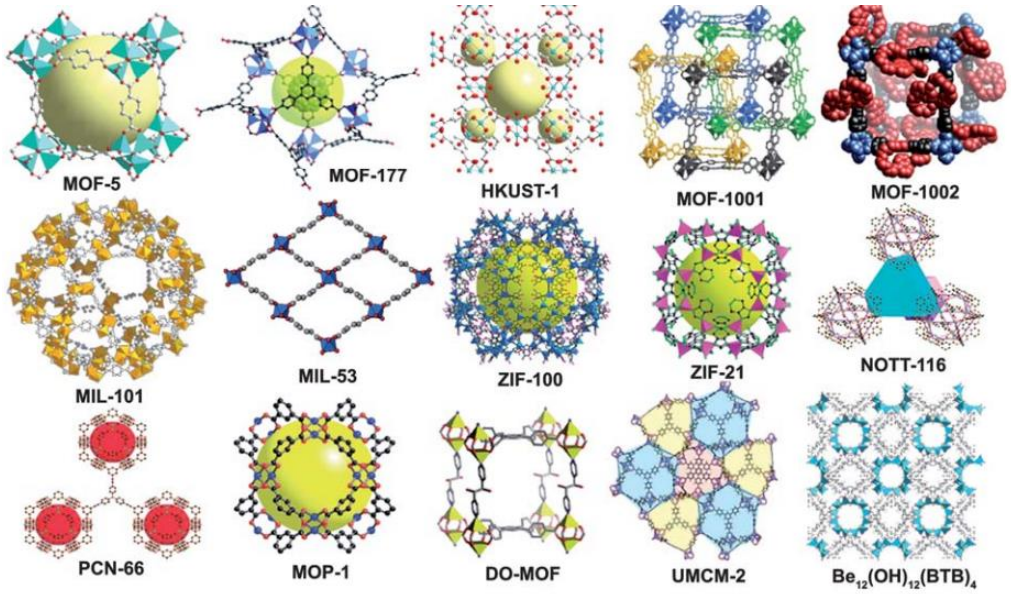

Figure 1.7. Three dimensional structures of several different MOFs. Reproduced with permission.[80] Copyright, 2010, Royal Society of Chemistry.

porous materials such as porous carbon.[85-87] In this approach, carbon precursor such as furfuryl alcohol infiltrated the MOFs‟ channels and both were carbonized at high temperature, which resulted in porous carbons. It was also reported that porous carbon can be prepared through direct carbonization of MOFs.[88, 89] In this case, MOFs act as a carbon precursor and self-sacrificial template.

1.6 LAYER-BY-LAYER ASSEMBLY

Layer-by-layer (LbL) assembly is a versatile technique to build multilayer composite films. The LbL technique was first introduced by Decher and coworkers in 1992.[90, 91] Since then, LbL assembly has attracted great attention.[92] The typical LbL assembly process is shown in Figure 1.8. In a typical procedure, for instance, a positively charged substrate is immersed in a solution containing negatively charged species.

The substrate‟s surface charge is reversed by the adsorption of negatively charged species from the solution.[92] Excessively adsorbed species are removed by washing steps. When the substrate is dipped in the next solution containing positively charged species, the surface charge of the substrate is reversed again. By repeating these steps, a multilayer film is obtained. LbL assembly can be carried out using dip-coating, spin-coating, and spraying.[93-95]

Polyelectrolytes have been widely employed to build up LbL films. However, materials that can be used in LbL assembly are not limited to polyelectrolytes. A number of materials can be used to fabricate LbL films including clays, graphene oxide,

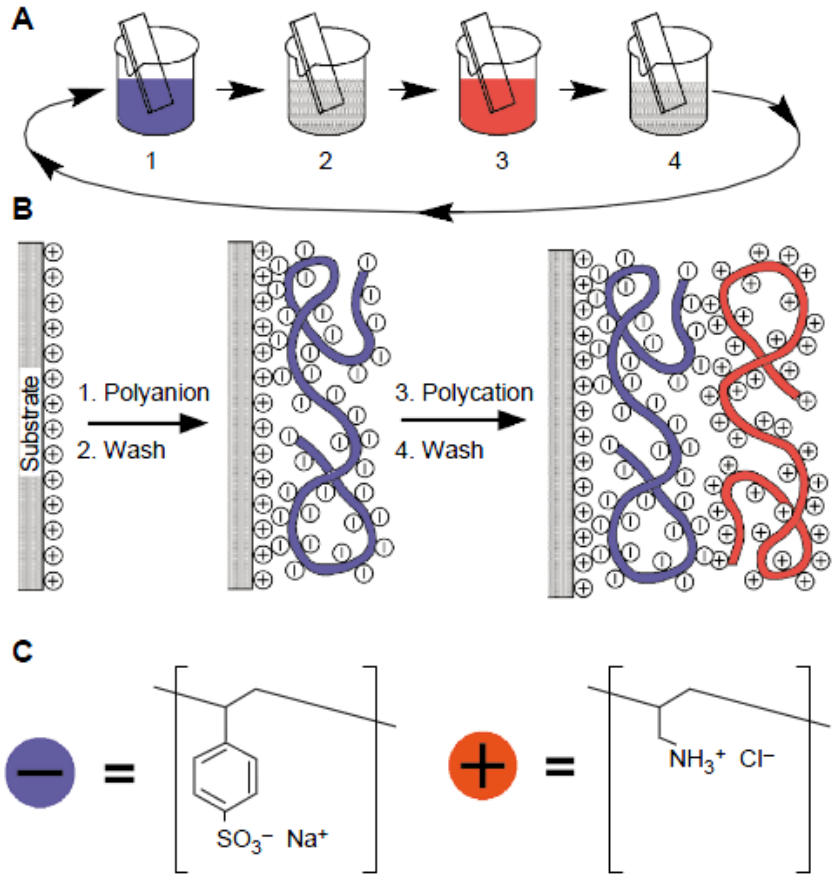

Figure 1.8. (a) Layer-by-layer assembly process, (b) simplified molecular adsorption step, and (c) chemical structures of two typical polyions, the sodium salt of poly(styrene sulfonate) and poly(allylamine hydrochloride).Reproduced with permission.[96] Copyright, 1997, The American Association for the Advancement of Science.

nanoparticles, dendrimers, proteins, DNA, colloids, quantum dots, metal oxides, and carbon nanotubes. [75, 97-106] The driving force of LbL assembly can be various interactions

such as electrostatic interactions, hydrogen bonding, charge transfer, and hydrophobic interactions.[91, 107-109]

LbL assembly has a number of advantages. LbL assembly is a very simple and easy way to build up thin films.[110] Various substrates can be chosen including silicones, glasses, and metals.[91] Substrates can be conformally coated by LbL aasembly.[111] The thickness of LbL films can be easily contolled by the number of sequential adsorption steps.[110] The properties of LbL films can also be fine-tuned by changing the assembly pH and ionic strength.[111] For example, the degree of charge of weak polyelectrolytes such as poly(allylamine hydrochloride) and poly(acrylic acid) is strongly dependent on pH.[112-114] Therefore, changing pH of polyelectrolytes leads to different film growth.[112, 113]

The LbL technique has been widely employed in a variety of research fields including drug delivery,[115, 116] sensors, [117, 118] antifogging coating,[119, 120] antimicrobial coating,[121] light-emitting diodes,[122] anticorrosion coating,[123, 124] and energy storage systems.[63, 94, 95, 125-127]

For energy storage, Hammond‟s group successfully fabricated porous multiwalled carbon nanotubes (MWNT) LbL electrodes.[63, 127] They functionalized MWNTs to prepare positively charged MWNTs and negatively charged MWNTs for LbL assembly.[127] The MWNT LbL electrode showed a high capacity (~200 mAh/g), specific energy and specific power (200 mWh/g at 100 mW/g).[63] The oxygen-containing functional groups on the MWNT surface participated in redox reaction during the charge-discharge processes, leading to high electrochemical performance.[63]

Porous PANI nanofiber/MWNT LbL electrode was also created using positively charged PANI nanofibers and negatively charged MWNTs.[94] This porous PANI nanofiber/MWNT LbL electrode delivered high volumetric capacity (~210 mAh/cm^3) as well as high energy density and power density (~220 mWh/L at ~100 W/L). Faradaic redox reactions of both MWNT and PANI nanofiber provided charge storage.[94]

1.7 THESIS SCOPE

This thesis focuses on a variety of electrode materials for energy storage. Various electrode materials such as PANI, graphene, and porous carbons were synthesized. The properties of electrode materials were thoroughly studied and their electrochemical performance was assessed for energy storage.

In chapter 2, oxidatively stable PANI:PAAMPSA electrodes were demonstrated. Even though PANI has been extensively investigated as electrode materials, its low cycling stability hampers its wide applications. This is mostly probably due to irreversible oxidation of PANI to pernigraniline based at high potentials. In order prevent irreversible oxidation of PANI and enhance its cycling stability, PANI:PAAMAPSA complex was synthesized via template polymerization. PANI:PAAMPSA can be dispersed in water due to its negative surface charge originating from excess sulfonic acid groups of PAAMPSA. This polyacid doped PANI exhibited high reversible capacity (~230 mAh/g of PANI) as well as significantly enhanced cycle life due to the strong interactions between PANI and PAAMPSA.

In chapter 3, PANI:PAAMPSA was successfully employed to fabricate LbL films on ITO substrates for the first time. Three different LbL films were created; PANI/PAAMPSA, PANI/PANI:PAAMPSA, and poly(ethylenimine)/PANI:PAAMPSA. Their film growth, composition, and charge storage were characterized and compared. The capacities of PANI/PAAMPSA and PANI/PANI:PAAMPSA were higher than that of poly(ethylenimine)/PANI:PAAMPSA while poly(ethylenimine)/PANI:PAAMPSA showed the best cycling performance. It was found that PANI:PAAMPSA could retain its oxidative stability within poly(ethylenimine)/PANI:PAAMPSA LbL films.

In chapter 4, the porous PANI nanofiber/electrochemically reduced graphene oxide (PANI NF/ERGO) hybrid electrodes were demonstrated for energy storage. To fabricate PANI NF/ERGO electrodes, first, the PANI nanofiber/graphene oxide (PANI NF/GO) films were created using LbL assembly followed by an electrochemical reduction. By using the electrochemical reduction in place of chemical reduction methods, we could take advantage of great processability of GO. The PANI NF/ERGO exhibited great electrochemical performances in terms of capacity as well as cyclability. It was found that electrode thickness affects their electrochemical performances.

In chapter 5, nitrogen-doped porous carbon was synthesized through direct carbonization of nitrogen-containing MOF (IRMOF-3) for supercapacitor applications. A variety of methods have been suggested to synthesize nitrogen-doped porous carbons. However, most of them are complex and require multiple steps. Here, the one step synthesis of nitrogen-doped porous carbon was demonstrated through carbonization of MOFs. During carbonization, MOFs acts as carbon, nitrogen precursors as well as a self-

sacrificial template. Furthermore, nitrogen content can be tuned by changing carbonization temperature. Nitrogen-doped porous carbon showed excellent performances as supercapacitor electrodes.

CHAPTER II

OXIDATIVELY STABLE POLYANILINE:POLYACID ELECTRODES FOR ELECTROCHEMICAL ENERGY STORAGE*

2.1 INTRODUCTION

Polyaniline (PANI), a conductive polymer, has been extensively studied in various application systems such as sensors,[128] memory devices,[129] fuel cells,[130] and energy storage systems[41, 131] owing to PANI's unique redox properties, good conductivity, low cost, and ease of synthesis.[45] PANI has several oxidation states (leucoemeraldine base, emeraldine salt, emeraldine base, pernigraniline base, and pernigraniline salt) that can be accessed through reaction pathways shown in Figure 2.1a PANI can be employed as an electrode in aqueous[20, 35, 132-134] as well as non-aqueous energy storage systems.[46, 131, 135, 136] In aqueous conditions, the average operating voltage of PANI electrodes is limited (usually up to 0.9 V vs. saturated calomel electrode) because of electrochemical degradation.[137, 138] On the other hand, in non-aqueous conditions, the average operating voltage for PANI electrodes is much higher.[46, 139-141] Therefore, PANI has been widely studied as a cathode material in PANI|Li batteries on account of its relatively good capacity and redox reversibility under moderately

*Reprinted with permission from "Oxidatively stable polyaniline:polyacid electrodes for electrochemical energy storage" by Ju-Won Jeon, Yuguang Ma, Jared F. Mike, Lin Shao, Perla B. Balbuena and Jodie L. Lutkenhaus, Phys. Chem. Chem. Phys. 2013, 15, 9654-9662, Copyright (2013), Royal Society of Chemistry.

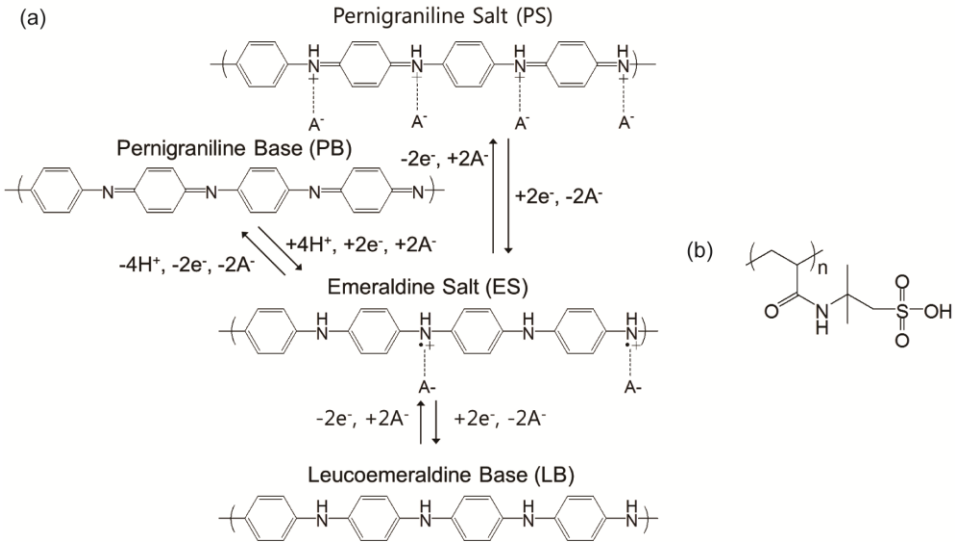

Figure 2.1. Chemical structures of PANI and PAAMPASA. (a) Several PANI oxidation states discussed in this work, and (b) the chemical structure of PAAMPSA.

oxidizing potentials (~3.5 V vs. Li/Li).[20, 142, 143] In non-aqueous conditions, polyaniline favors an aprotic reaction pathway; therefore, reversible switching between leucoemeraldine base and emeraldine salt forms is commonly observed for PANI electrodes. At more oxidizing potentials, emeraldine salt irreversibly oxidizes to pernigraniline base due to a lack of protons in the electrolyte,[13] which ultimately limits the capacity of the electrode as well as its cycle life. For this reason, it is important to consider a reversible reaction pathway devoid of protons.

If one could reversibly access the leucoemeraldine base, emeraldine salt, and pernigraniline salt forms of polyaniline via an aprotic pathway, then the reversible capacity of polyaniline could essentially double, storing four electrons per monomer unit

instead of two. Unfortunately, pernigraniline salt is highly unstable owing to its susceptibility to nucleophilic attack. There have been few reports on the stabilization of pernigraniline salt under specialized conditions. D"Aprano et al. reported that N-alkyl-substituted PANI could be converted to pernigraniline salt owing to increased basicity of the imine units by electrondonating alkyl groups in highly acidic environments.[144] Lu *et al*.and Bazito *et al*. also successfully stabilized the pernigraniline salt form of PANI using a hydrophobic ionic liquid.[145, 146] In neither case was the electrochemical energy storage performance studied. Tsutsumi *et al*. showed that a PANI exchanged with a polyacid could be cycled 40 times from2 to 4.3 V vs. Li/Li^+ in a nonaqueous system,[147]

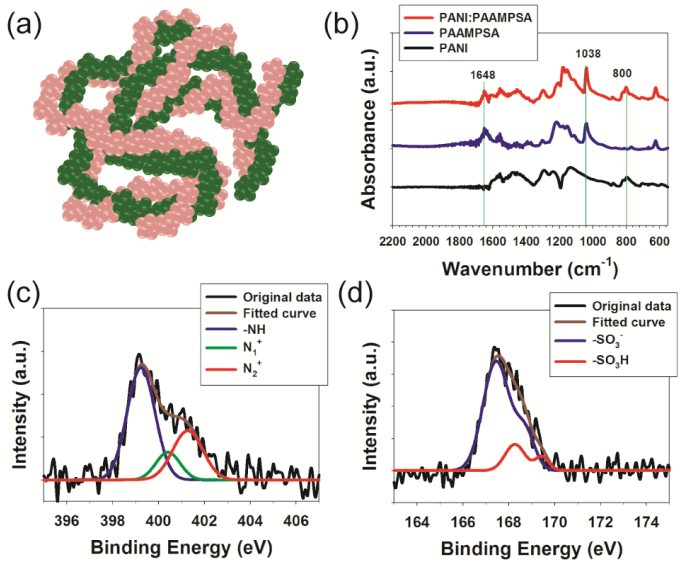

Figure 2.2. (a) A simplified rendering of a PAIN:PAAMPSA colloid. (b) FTIR spectra of PANI:PAAMPSA, PAAMPSA, and PANI, (from top to bottom). (c) Nitrogen and (d) sulphur XPS spectra of PANI:PAAMPSA.

which was suggestive of polyacid‟s ability to boost PANI‟s oxidative stability; however, the origin of this stability remained unclear.

Of particular interest, is the recent demonstration of pH-stable polyaniline derivatives made via template polymerization.[148] In this approach, aniline monomer is oxidatively polymerized in the presence of a polyacid template, poly(2-acrylamido-2-methyl-1-propanesulfonic acid) (PAAMPSA, Figure 2.1b), resulting in a water-dispersible "PANI:PAAMPSA" Colloid, Figure 2.2a.[148-158] Easily processable via spin-casting, ink-jetting printing and more, the resultant film has exceptional conductivity (up to 50 S cm^{-1}),[158] finding applications in thin film transistors. In aqueous conditions, PANI:PAAMPSA switches reversibly between leucoemeraldine base, emeraldine salt, and pernigraniline base states.[158] It has been suggested that the pH-stability and aqueous electrochemical reversibility arises from specific interactions such as hydrogen bonding between PANI and PAAMPSA.[148, 154]

Motivated by PANI:PAAMPSA‟s exceptional stability and reversibility in aqueous conditions, we hypothesized that this material would perform similarly well under non-aqueous conditions, perhaps suitably stabilizing pernigraniline salt under highly oxidizing potentials. Using a combination of experimental and computational approaches, we demonstrate that PAAMPSA indeed acts as a stabilizing agent that allows PANI:PAAMPSA electrodes to reversibly store charge under extremely oxidizing potentials (4.5 vs. Li/Li^+). To the best of our knowledge, this is the first report of the pernigraniline salt form in PANI:PAAMPSA electrodes, and its subsequent use in an energy storage system.

2.2 EXPERIMENTAL SECTION

PANI:PAAMPSA was synthesized using a published approach.[154] PAAMPSA (5.8 g, 0.028 mol, Mw = 800 kg mol^{-1}, Scientific Polymer Products) was dissolved in 375 ml of deionized water. Aniline (2.6 g, 0.028 mol, Sigma Aldrich) was added to the PAAMPSA solution, and it was stirred for 1 h at room temperature. Ammonium peroxydisulfate (5.8 g, 0.025 mol, Sigma Aldrich) was dissolved in 25 ml deionized water separately. Both solutions were purged using nitrogen gas for 1 h at 5 ^{o}C. After purging, ammonium peroxydisulfate solution was added drop wise to aniline–PAAMPSA solution. The polymerization reaction was carried out for 24 h. Acetone was then added to the PANI:PAAMPSA dispersion to recover the polymer complex. The supernatant was removed, and then the resulting PANI:PAAMPSA was washed and filtered with copious amounts of acetone to remove low molecular weight material. After washing, PANI:PAAMPSA complex was dried under vacuum at room temperature.

The emeraldine salt state of polyaniline was synthesized using conventional oxidative polymerization.[159, 160] Aniline (2.321 g, 0.025 mol) was dissolved in 50 ml of 1 M HCl aqueous solution and cooled to 5 1C. Ammonium peroxydisulfate (5.8 g, 0.025 mol) was also dissolved in 50 ml 1 M HCl solution, separately. Both solutions were stirred under nitrogen for 1 h. Polymerization was initiated by slowly adding the ammonium peroxydisulfate solution to the aniline solution. After stirring for 1 h, the resultant material was filtered and washed repeatedly with 1 M HCl until the filtrate became colorless. The powder was dried under vacuum at room temperature.

PANI:PAAMPSA and PANI electrodes were prepared. For PANI:PAAMPSA electrodes, ITO-coated glass (Delta Technologies) was first cleaned using subsequent sonication in dichloromethane, acetone, methanol and deionized water for 15 minutes each. After drying in a convection oven, plasma treatment was carried out on the ITO substrates. To render the substrate‟s surface positively charged, APTES ((3-aminopropyl)triethoxysilane, Sigma Aldrich) treatment was carried out on the clean ITO-coated glass substrates. Substrates were immersed in 2 v% APTES in anhydrous toluene for 30 min at 75 ^{o}C, and washed sequentially with toluene, ethanol, and deionized water. Finally, the substrates were heated at 110 ^{o}C for 15 min.[13, 161] PANI:PAAMPSA (3 wt%) was sonicated for 8–10 hours in deionized water to form a stable dispersion without aggregation. The PANI:PAAMPSA dispersion was then spin-cast onto APTEStreated ITO-coated glass.

For polyaniline electrodes, PANI dispersions were first prepared using a previously reported method.[102] 0.5 g of emeraldine base PANI was slowly added to dimethylacetamide (DMAc) and stirred overnight, followed by sonication for 8–10 hours. The emeraldine base PANI solution was slowly added to pH 3–3.5 1 : 9(v/v) DMAc : water solution. The pH of the PANI dispersion was then adjusted to pH 2.5–2.6 by adding 1 M HCl to convert PANI from the emeraldine base to the emeraldine salt form. Finally, the 0.5 wt%PANI dispersion was spin-cast onto clean ITO-coated glass (without APTES treatment).

For Fourier transform infrared (FTIR) spectroscopy, PANI:PAAMPSA, PANI dispersion and PAAMPSA solutions were drop-cast onto ZnSe substrates, and dried

under vacuum. FTIR spectra were obtained using a Bruker Optics Spectrometer (ALPHA-P 10098-4) with 2 cm^{-1} resolution, and 1024 scans. X-ray photoelectron spectroscopy (XPS) was performed using a Kratos Axis Ultra Imaging X-ray photoelectron spectrometer with a resolution of 0.1 eV. Monochromatic Al (10 mA, 12 kV) was used as the X-ray source. The binding energy of C 1s at 284.5 eV was used as a reference to exclude charging effects. UV-Vis spectra were recorded using a Hitachi U-4100 spectrometer. The zeta potential (Nano ZS90, Malvern) was measured for PANI:PAAMPSA and PANI dispersions. The thickness of casted films was measured at five locations using a P-6 profilometer (KLA-Tencor), and the results were averaged. The films‟ conductivity was measured using a home-built four-point probe at five locations.

The mass of each film was obtained using a quartz crystal microbalance (Maxtek). A polished Ti/Au-coated quartz crystal was blown with nitrogen, and then measurements were carried out on a bare substrate for 30 min to obtain a baseline. Afterwards, the crystal was treated using oxygen-plasma for 5 min, and then a dispersion of PANI:PAAMPSA or PANI was deposited. Data was recorded for 5 min and averaged. The mass of each film was calculated based on the Sauerbrey equation.

Density functional theory (DFT) with the Becke three parameter hybrid exchange functional[162] and the Lee–Yang–Parr correlation functional[163] (B3LYP) was employed for geometry optimization and vibrational frequency computations. All calculations were performed using GAUSSIAN 09 programs with a 6-31G(d) basis set. The local minima on the potential energy surface were verified by vibrational frequency analysis. The

interaction energy between PAAMPSA and diphenylamine (DPA) was evaluated using the following equation: $E_{int} = E_{complex} - E_{PAAMPSA} - E_{DPA}$, in which $E_{complex}$ is the total energy of the PAAMPSA:DPA complexes with adsorbed gas molecule(s), and $E_{PAAMPSA}$ and E_{DPA} are the energies of PAAMPSA and DPA clusters, either in neutral or in ionic states. The basis set superposition error (BSSE) was corrected by the counterpoise method. Partial atomic charges were produced using the CHelpG method.[164] Simulated annealing techniques[165] were used to determine the binding sites of PANI and PAAMPSA chains. Each simulation was composed of 10 cycles and each cycle consists of 2×10^6 steps. In each cycle, the system was heated up to 10^5 K and then slowly cooled down to 298 K. The LJ potentials were taken from the generic DREIDING force field.[166] Partial point charges for framework atoms were calculated using QEq method. A spherical cutoff of 18.5 Å was applied to the LJ and Coulomb potentials with a cubic spline truncation.

All electrochemical testing was performed in a water-free (<2 ppm), oxygen-free (<2 ppm), argon-filled MBraun glove box. The electrochemical properties of films prepared on ITO were examined using a three-electrode cell and a sandwich-type cell. For the three-electrode cell, PANI:PAAMPSA and PANI films casted onto ITO-coated glass acted as the working electrode, and two lithium ribbons were utilized as the counter and reference electrodes. The working electrode area was 3–3.5 cm^2, and the mass loading was 0.02 to 0.025 mg cm^{-2}. 0.5 M $LiClO_4$ dissolved in propylene carbonate was used as the electrolyte. All prepared films were washed with electrolyte solution prior to electrochemical testing. For the sandwich-type cell, PANI:PAAMPSA and

PANI on ITO-coated glass were used as the cathode, whereas lithium ribbon was used as the anode. 1 M $LiClO_4$ dissolved in propylene carbonate was used as the electrolyte in the cell. All electrochemical measurements were carried out using a Solartron SI 1287 at room temperature over 1.5 to 4.5 V vs. Li/Li^+. Properties were calculated using the weight of the active material (PANI) as a basis.

2.3 RESULTS AND DISCUSSION

We first synthesized PANI:PAAMPSA using the method of Yoo *et al*.[154] and PANI using the method of Huang *et al*.[160] The resulting PANI:PAAMPSA powder was dispersed in water to yield a green dispersion that was water-stable for over two weeks. A comparable PANI dispersion was highly unstable, producing aggregates within hours after sonication (Figure 2.3). At pH 2.5, the zeta potentials of PANI:PAAMPSA and PANI were _33 and 42 mV, respectively. The negative charge suggests that the colloid contains more PAAMPSA units than PANI units. The conductivity of a PANI:PAAMPSA film was 0.38 S cm^{-1}, in agreement with prior reports.[154, 158]

FTIR spectra confirmed the successful synthesis of PANI:PAAMPSA and PANI, Figure 2.2b–d, respectively. PANI:PAAMPSA FTIR spectra possess features of both PAAMPSA and emeraldine salt PANI. For example, peaks at 1038 cm^{-1} ($–SO_3H$ vibration)[167] and 1648 cm^{-1} (secondary amide C=O stretch)[168] were present in both PAAMPSA and PANI:PAAMPSA spectra, and a peak at 800 cm^{-1} (C–H out of plane vibration)[169, 170] were present in both PANI and PANI:PAAMPSA spectra. In addition

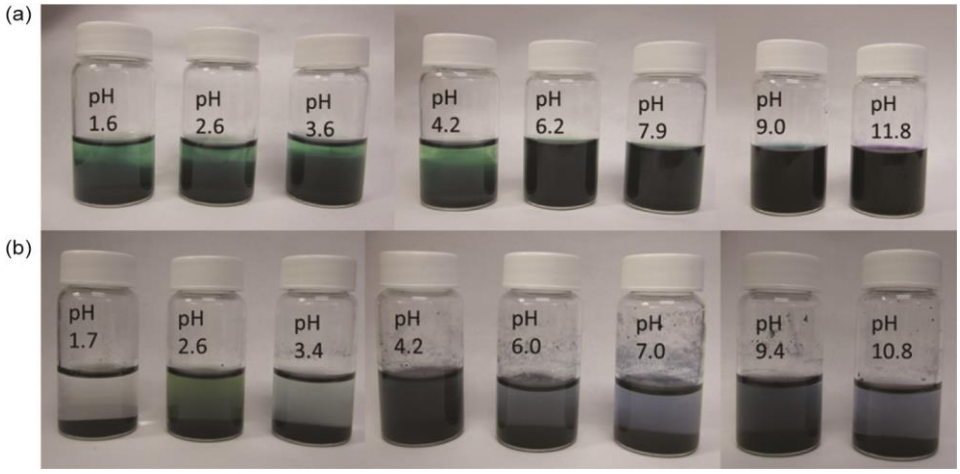

Figure 2.3. 0.05 wt% PANI:PAAMPSA in pH-adjusted water (a) 7 days after 10 hours of sonication. 0.05 wt% PANI in pH-adjusted water (b) 24 hours after 10 hours sonication.

hydronium sulfonate salts (1100–1250 cm^{-1}) were also observed in PANI:PAAMPSA spectra.[171]

The PANI content, as well as the chemical and electronic state of the elements within the PANI:PAAMPSA colloid, was determined using XPS. PANI:PAAMPSA yielded a nitrogen to sulfur molar ratio of 1.76 to 1, meaning that PANI comprised 25 wt% of the colloid. For the calculation, number of sulfur was designated as X. Then, the molar ratio of nitrogen to sulfur was equal to (4+X)/X, which is 1.76. The calculated X value was 5.26, which means there are 5.26 PAAMPSA units per four anline units. The molar mass of four aniline units and a PAAMPSA unit was 362.4 and 207.2 g/mol, respectively. Therefore, the weight percent of PANI in PANI:PAAMPSA is equal to 362.4/(362.4+5.26 x 207.2). The calculated weight percent of PANI in

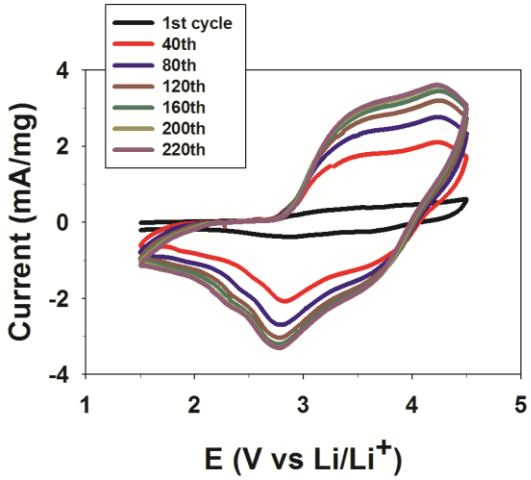

Figure 2.4. Cyclic voltammograms of PANI-PAAMPSA during pre-conditioning. The scan rate was 10 mV/s.

PANI:PAAMPSA was approximately 25wt%.

Both the nitrogen and sulfur XPS peaks were deconvoluted as a collection of Gaussian peaks using published approaches.[158, 172, 173] The nitrogen XPS peak was modeled as three Gaussian peaks centered at 399.2, 400.4, and 401.3 eV, which represent neutral nitrogen groups (NH – such as amine and imine groups in PANI and amide groups in PAAMPSA), protonated nitrogens associated with polarons (N_1^+), and protonated nitrogens interacting with sulfonic acid groups of PAAMPSA (N_2^+), respectively.[158, 172] Based on the integrated area of the peaks, the percentages of NH, N_1^+, and N_2^+ were 59.2%, 12.7%, and 28.1%, respectively. This result indicates that PANI‟s protonated amine groups preferentially interact with PAAMPSA‟s sulfonic acid groups. The sulfur XPS peak was also deconvoluted into two separate Gaussian doublet peaks to determine the state of PAAMPSA within the PANI:PAAMPSA colloid.[173] The doublet

at 167.5 and 168.7 eV was assigned to deprotonated sulfonic acid groups (SO_3^-), while another doublet at 168.3 and 169.5 eV was ascribed to the protonated version (SO_3H). Based on the integrated area of each doublet, the percentages of SO_3^- and SO_3H groups were 83.5% and 16.5%, respectively.

Having successfully synthesized PANI:PAAMPSA, we then evaluated its non-aqueous electrochemistry in a three-electrode cell using separate lithium ribbons as reference and counter electrodes and using non-aqueous propylene carbonate solution containing 0.5 M $LiClO_4$ as the electrolyte. Cyclic voltammetry was first performed on PANI:PAAMPSA films (250 to 540 nm thick) on ITO-coated glass as the working electrode. Surprisingly, the current increased with each subsequent cycle, indicating that PANI:PAAMPSA was becoming more and more electrochemically active, Figure 2.4. Such a phenomenon has been previously reported[174-176] and has been attributed to the displacement of hydronium ions (associated with sulfonic acid groups) with lithium ions and solvent. After multiple cycles, the cyclic voltammograms eventually stabilized. We found that this „„preconditioning"""step could be performed using a combination of cyclic voltammetry and galvanostatic cycling (50 cycles at 10 mV s^{-1} and 200 cycles at 50 C, 1.5–4.5 V vs. Li/Li^+ cut-offs) to achieve an enhanced PANI:PAAMPSA electrode performance. This finding suggests that water, although present despite thorough drying, does not interfere with PANI:PAAMPSA"s non-aqueous electrochemistry if a pre-conditioning step is applied. Spectroelectrochemistry of a PANI:PAAMPSA electrode prior to preconditioning suggests that, initially, very little of the material is electrochemically active, confirming that pre-conditioning is an essential step in the

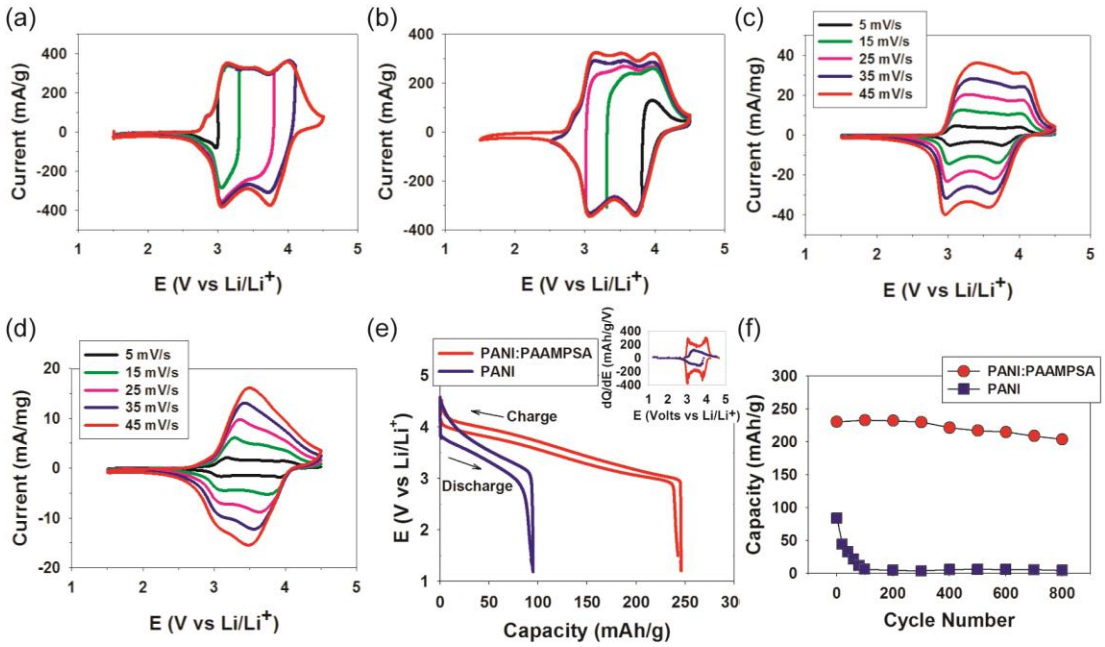

Figure 2.5. Cyclic voltammetry and galvanostatic cycling of PANI:PAAMPSA and PANI electrode. Cyclic voltammograms of pre-conditioned PANI:PAAMPSA electrodes in (a) an increasing potential window and in (b) a decreasing potential window. The scan rate is (1mV/s). Cyclic voltammograms of (c) preconditioned PANI:PAAMPSA and (d) un-preconditioned PANI electrodes under varying scan rates. (e) Galvanostatic charging and discharging of PANI:PAAMPSA and PANI electrodes at a rate of 20 C, and (f) resultant capacities for those electrodes cycled at a rate of 50 C.

preparation of PANI:PAAMPSA electrodes. In contrast, PANI homopolymer severely degraded under an identical preconditioning procedure; therefore, pre-conditioning was applied only to PANI:PAAMPSA electrodes.

The reversibility of a preconditioned PANI:PAAMPSA electrode was demonstrated by cyclingwithin potential windows expanding from high and low

potentials, Figure 2.5a and b. In cathodic scans, two distinctive peaks around 3.1 V and 3.8 V were observed, which were attributed to two separate reversible reactions. On the other hand in anodic scans, the peaks were less distinct and plateaus in the range of 3 to 4 V were present, where the plateau has been previously attributed to continuous faradaic charge transfer.[177, 178] In addition, all cathodic and anodic scans overlapped, and the peaks at 3.1 and 3.8 V vs. Li/Li^+ were nearly symmetric. As the scan rate increased from 5 to 45 mV s^{-1} (Figure 2.5c), the cathodic peaks shifted slightly to lower potentials (by -70 mV for 3.1 V and by -185 mV for 3.8 V). Both peaks‟ current value showed a linear dependence on scan rate, which is a typical response for an electroactive film without concentration gradients.[179] In comparison, cyclic voltammograms of electrodes made from PANI exhibited two peaks at 3.2 and 4 V; however, the cathodic peak at 4 V shifted by -429 mV as scan rate increased (Figure. 2.5d), which indicated that the redox process was less reversible than that of PANI:PAAMPSA.

The electrodes were then cycled galvanostatically between 1.5 and 4.5 V vs. Li/Li+ using a three-electrode cell, Figure 2.5e and f. A plot of dQ/dE vs. E mimicked that of the cyclic voltammograms, as expected, (Figure 2.5e inset). The cycling behavior of preconditioned PANI:PAAMPSA was strikingly different from that of (un-preconditioned) PANI. When cycled at the same rate of 20 C, PANI:PAAMPSA‟s capacity (243 mAh g^{-1}) was more than twice that of PANI (93 mAh g^{-1}), Figure 2.5e. Here, the C rate was calculated using the mass of polyaniline as a basis, as was the capacity. After 800 cycles at a rate of 50 C, PANI:PAAMPSA retained 88.5% of its initial capacity, whereas PANI‟s capacity rapidly faded, retaining only 5.5%, Figure 2.5f.

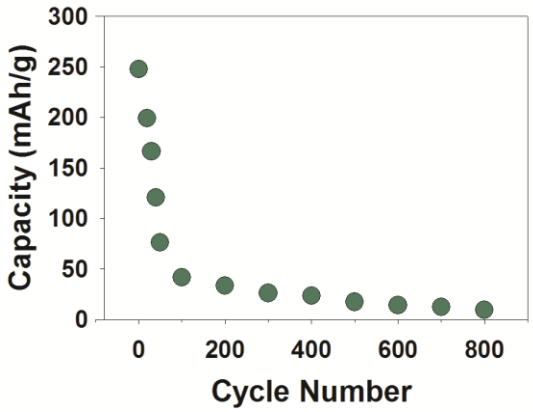

Figure 2.6. Galvanostatic charging and discharging cycles of dichloroacetic acid annealed-PANI:PAAMPSA.

For a theoretical capacity of 294 mAh g^{-1} (assuming four electrons passed and neglecting the anion), PANI:PAAMPSA‟s capacity was 69.3% of theoretical at the conclusion of the cycling experiment.

If one accounts for the mass of PAAMPSA, then the capacity becomes 61 mAh g^{-1} of PANI:PAAMPSA. Even if PAAMPSA diminishes the initial capacity of PANI:PAAMPSA by “diluting” the polyaniline, the capacity after 800 cycles far exceeds that of polyaniline homopolymer. These results indicate that for applications requiring highly oxidizing conditions, PANI:PAAMPSA may be more suitable choice than polyaniline. Furthermore, because PANI:PAAMPSA is able to retain its performance over a wide range of potentials, it is a promising candidate for hybrid composite electrodes.

In an attempt to further improve the capacity, solvent annealing was performed using dicholoracetic acid, which has been shown to increase PANI:PAAMPSA‟s

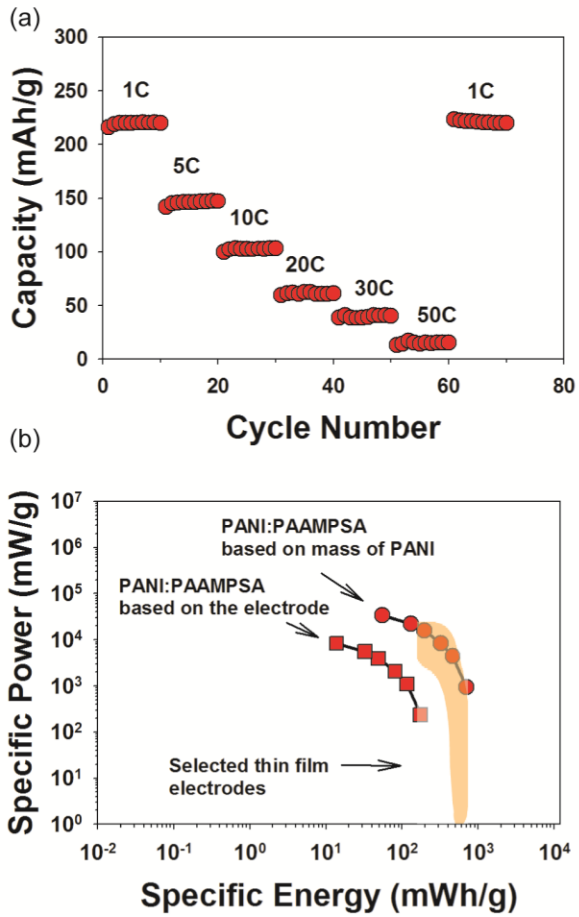

Figure 2.7. Capacity, specific energy, and specific power of PANI:PAAMPSA electrodes in a sandwich cell configuration. (a) Capacities of a PANI:PAAMPSA|Li sandwich cell cycled under various C rates, and (b) the corresponding Ragone plot. Shaded regions adapted from ref.[63, 180, 181]

conductivity and performance as a transistor.[158] However after solvent annealing, the cycle life greatly decreased (Figure 2.6) possibly because the interactions between PANI and PAAMPSA were altered such that oxidative stability was reduced.[158]

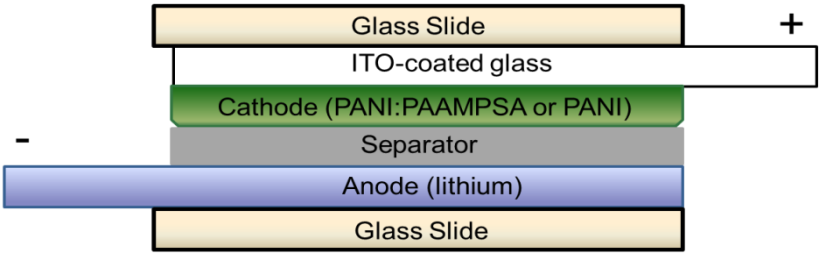

Figure 2.8. Schematic of the sandwich cell used in Figure 2.7. The electrolyte was 1 M $LiClO_4$ in propylene carbonate.

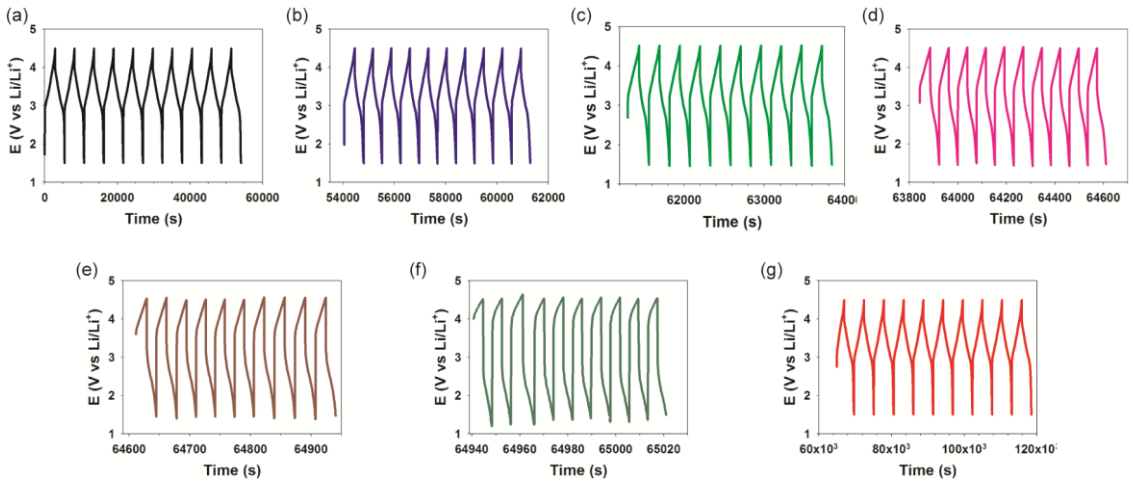

Figure 2.9. Charging and discharging cycles of PANI:PAAMPSA|Li sandwich cell cycled under various C rates. (a) 1C, (b) 5C, (c) 10C, (d) 20C, (e) 30C, (f) 50C, and (g) 1C again.

To demonstrate PANI:PAAMPSA‟s suitability as an electrode for energy storage, we performed galvanostatic cycling on a sandwich cell containing a PANI:PAAMPSA cathode and lithium metal anode (Figure 2.7 and Figure 2.8 and Figure 2.9). The cell

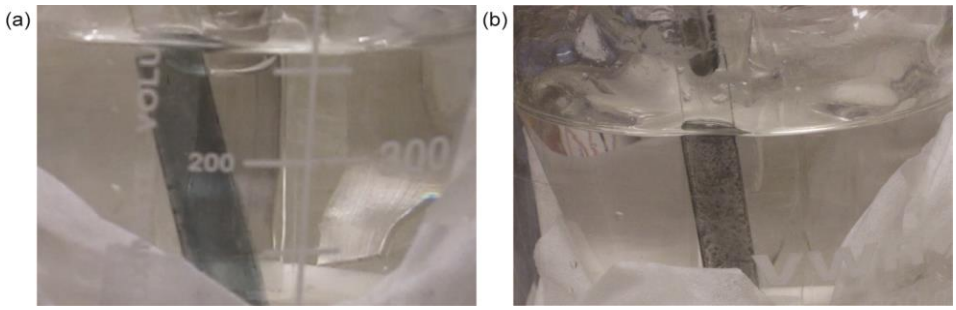

Figure 2.10. (a) PANI:PAAMPSA and (b) PANI on ITO-coated glass at 4.5 V vs. Li/Li^+.

was cycled at various C rates, where 1 C denotes the amount of current required to discharge the cell in one hour and where the C rate is based on the mass of polyaniline in the cathode. As the discharge rate increased from 1 C to 50 C, the capacity decreased from 220 to 17 mAh g^{-1}. The capacity showed good recovery upon cycling again at 1 C. The capacity of the sandwich cell was less than that of the three-electrode cell most likely because of differences in internal resistance.

From these experiments, the specific power and energy were calculated based on the mass of polyaniline as well as the mass of the whole electrode, and summarized in a Ragone plot, (Figure 2.7b). Based on the mass of polyaniline, the maximum specific power was 33600 mW g^{-1} at a rate of 50 C, and the maximum specific energy was 700 mWh g^{-1} at a rate of 1 C. These values are comparable to other thin film cathodes composed of inorganic materials.[63, 181, 182]

To explain this stark contrast in cycling behavior between PANI:PAAMPSA and PANI, we must reconsider the reaction scheme shown in Figure 2.1a. For both materials,

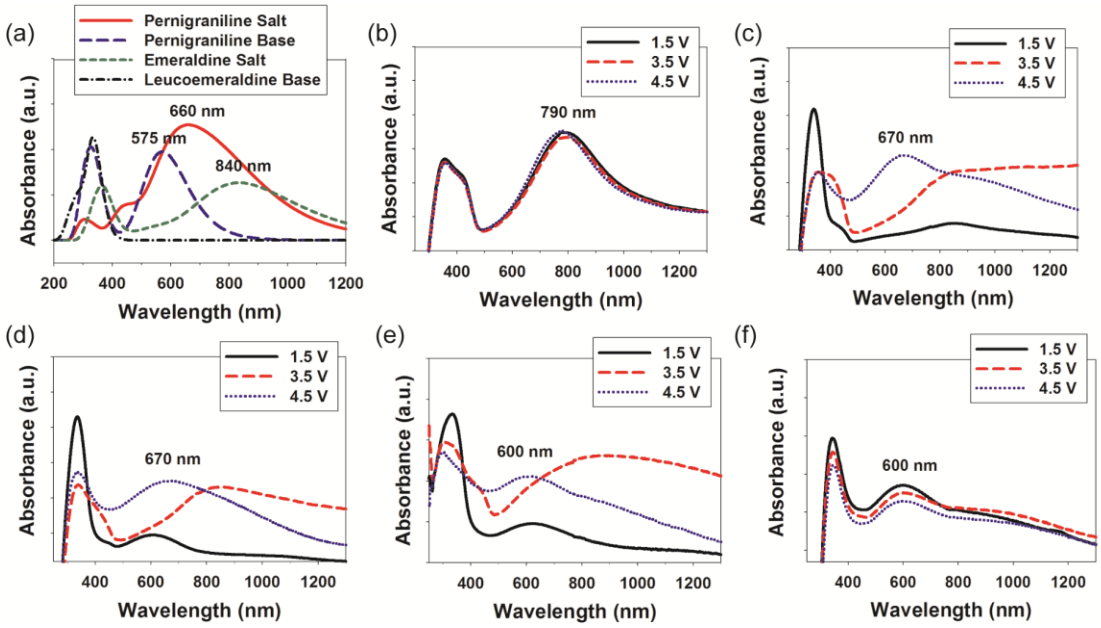

Figure 2.11. UV-vis spectra of PANI:PAAMPSA and PANI. (a) UV-vis spectra of simulated PANI, (b) un-preconditioned PANI:PAAMPSA, (c) preconditioned PANI:PAAMPSA before and (d) after galvanostatic cycling, and un-preconditioned PANI (e) before and (f) after cycling.

the redox reaction at 3.1 to 3.2 V is leucoemeraldine base oxidizing to emeraldine salt, changing in color from clear to emerald green. However, upon further oxidation at 3.7 to 4 V, PANI:PAAMPSA became midnight blue in color, and PANI became blue-violet (Figure 2.10), suggesting that the two materials oxidized to yield two different forms of polyaniline. Violet coloration is typical of pernigraniline base, and midnight blue is the reported coloration of pernigraniline salt.[145, 183] Based upon color, PANI:PAAMPSA oxidized along a fully aprotic pathway to form pernigraniline salt, whereas PANI oxidized to form pernigraniline base.

Both simulated and experimental UV-vis spectra provide evidence of the formation of pernigraniline salt and pernigraniline base for PANI:PAAMPSA and PANI electrodes, respectively, under highly oxidizing potentials, (Figure 2.11). Simulated UV-vis spectra based on first-principle calculations showed that emeraldine salt, pernigraniline salt, and pernigraniline base forms of polyaniline have peak maxima at 840 nm, 660 nm, and 575 nm, respectively, (Figure 2.11a). PANI:PAAMPSA electrodes were also examined experimentally after being held at 1.5, 3.5 and 4.5 V vs. Li/Li^+ and results agree quite well with the simulations. Before preconditioning (Figure 2.11b), PANI:PAAMPSA existed as emeraldine salt regardless of voltage, which indicates that very little PANI:PAAMPSA was electrochemically active. After preconditioning (Figure 2.11c), both spectra for 1.5 and 3.5 V showed characteristics typical of leucoemeraldine base and emeraldine salt forms,[148, 184] where leucoemeraldine base had increased absorbance in the UV region (340 nm, p–p* transition) and emeraldine salt had a peak at 780 nm and extended near-IR absorption (polaron interband transition). At 4.5 V, PANI:PAAMPSA was midnight blue in coloration and a peak at 670 nm was present along with near-IR absorption which was consistent with prior reports of the pernigraniline salt and with our simulated UV-vis spectra of pernigraniline salt.[144-146, 183] After cycling, the peaks were relatively unchanged, although a small peak at 627 nm appeared at 1.5 V for a fraction of the samples (Figure 2.11d). Some have attributed this peak to donor–acceptor interactions between PANI and its counter ions,[145, 185] but it is also possibly related to unreactive PANI.

On the other hand, PANI homopolymer‟s spectra before cycling were similar to

that of PANI:PAAMPSA with the exception of a peak at 600 nm for 4.5 V, which matched prior reports of pernigraniline base,[148, 183, 186] (Figure 2.11e). After 800 cycles (Figure 2.11f), all spectra showed characteristics of pernigraniline base, suggesting that the oxidation to pernigraniline base was irreversible, which explains PANI homopolymer‟s poor cycling behavior. In contrast, PANI:PAAMPSA‟s UV-vis spectra changed only slightly upon repeated cycling, demonstrating that PANI:PAAMPSA electrodes are far more reversible than PANI electrodes.

The origin of PANI:PAAMPSA‟s exceptional stability relative to PANI homopolymer possibly originates from specific interactions between PANI and PAAMPSA that dominate over side reactions that would otherwise lead to PANI‟s degradation. UV-vis spectra, in combination with cyclic voltammetry, demonstrated that PANI homopolymer converted from emeraldine salt to pernigraniline base between 3.5 and 4.5 V, losing protons in the process. As the potential decreased back from 4.5 V, pernigraniline base was unable to convert back to emeraldine salt because of the lack of protons available in the electrolyte. Upon subsequent cycling, more and more PANI homopolymer irreversibly oxidized to pernigraniline base, resulting in UV-vis spectra such as Fiure 2.11f. On the other hand, PANI:PAAMPSA did not show irreversible degradation within the voltages explored, nor did it show the formation of pernigraniline base. Rather, PAAMPSA, which acts as a dopant to PANI, interacted with PANI via hydrogen bonding and electrostatic interactions. By virtue of template polymerization, PANI and PAAMPSA appear to be so intimately entangled that repeated reduction and

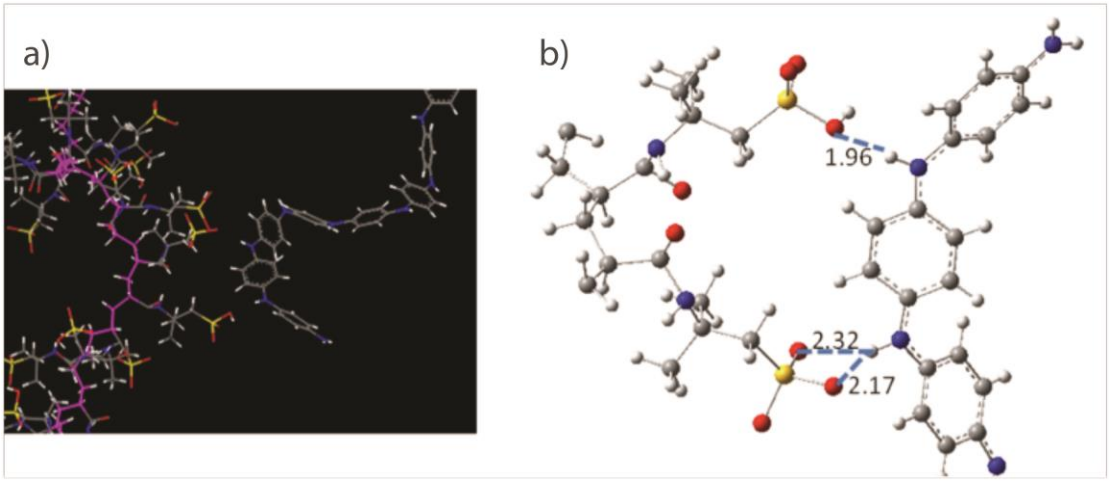

Figure 2.12. Binding sites of PANI and PAAMPSA chains by simulated annealing techniques. Marked distances, in Å, show close contact of the two chains. Yellow, red, blue, grey and silver denote sulfur, oxygen, nitrogen, carbon and hydrogen, respectively.

oxidation do not degrade the electrode‟s structure or performance, as evidenced by PANI:PAAMPSA‟s unchanged reversible capacity and UV-vis spectra.

To support the idea that PAAMPSA stabilized PANI in the pernigraniline salt state, we performed simulations of PANI‟s interactions with PAAMPSA. Our simulated annealing results show close contact between the sulfonic acid groups of PAMMPSA and the amine group of PANI chains, indicative of the formation of hydrogen bonds (Figure 2.12). This is in agreement with previous experimental studies.[148, 154] To further examine the hydrogen bond‟s strength, we performed first principles calculations using cluster models constructed on the basis of the structures of the simulated annealing

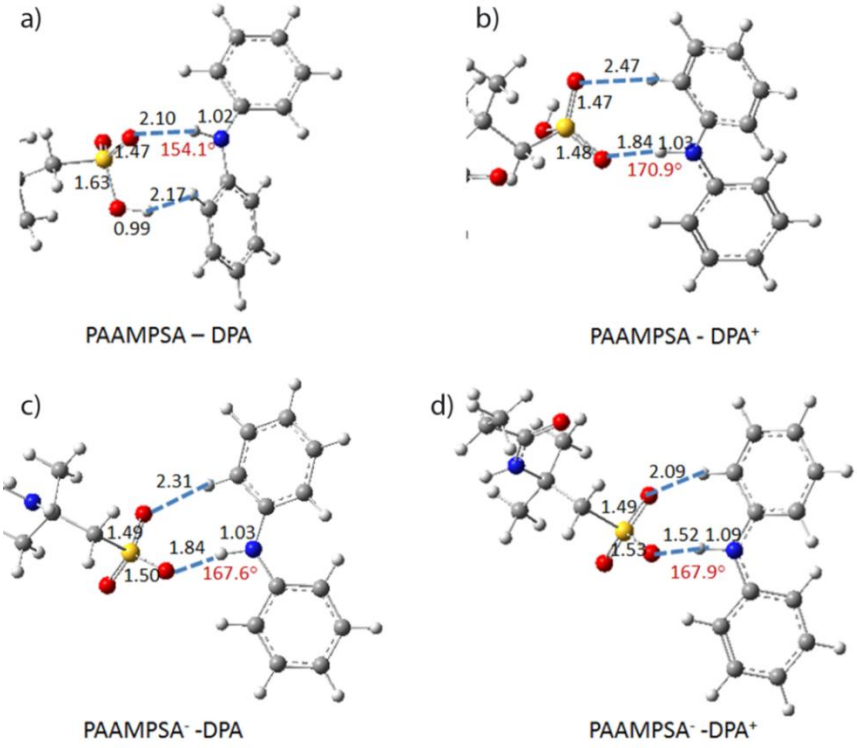

Figure 2.13. Optimized structures of PAAMPSA:DPA complexes. Yellow, red, blue, grey and silver spheres represent sulphur, oxygen, nitrogen, carbon and hydrogen atoms, respectively. The marked distances are in units of Å .

calculations. Because both SO_3^- and SO_3H were observed in XPS spectra, we investigated cluster models that included a single unit of neutral PAAMPSA and its anionic form, $PAAMPSA^-$.Similarly, PANI was modeled using both neutral diphenylamine (DPA) and its cationic form (DPA^+) to emulate the leucoemeraldine base, emeraldine salt, and pernigraniline salt forms. (Emeraldine salt was approximated as a mixture of neutral and cationic forms.)

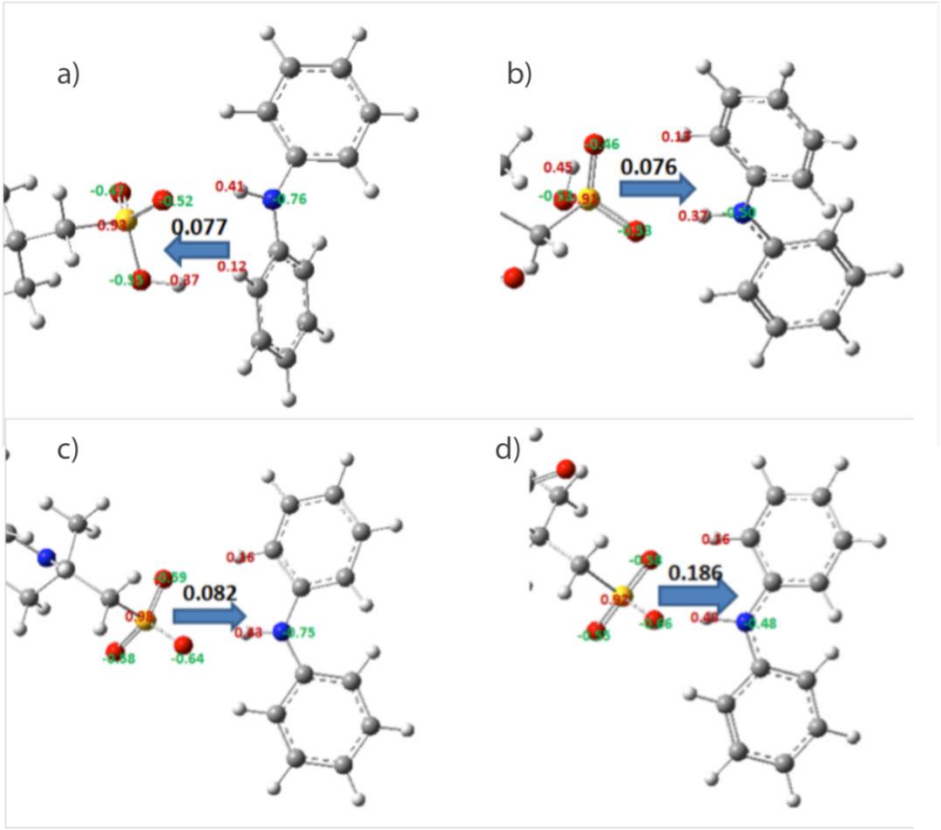

Figure 2.14. CHelpG charges of each PAAMPSA:DPA complex bearing the lowest total energy for (a) PAAMPSA:DPA, (b) PAAMPSA:DPA^+, (c) $PAAMPSA^-$:DPA, and (d) $PAAMPSA^-$:DPA^+. The arrows show the direction and magnitude of charge transfer.

Table 2. 1. Interaction energies of model cluster pairs.

E_{int} (kcal/mol)			
	PAAMPSA	$PAAMPSA^-$	EC
DPA	-10.3	-17.5	-4.3
DPA^+	-22.5	-94.7	-18.9

The optimized complex structures with lowest total energy are depicted in Figure 2.13. Hydrogen bonds were formed in all of the pairs. In the PAAMPSA:DPA pair, a relatively weak hydrogen bond was found, where the bond length was 2.10 Å and the angle (∠OHN) was 154.11°. When one of the species was charged, as for $PAAMPSA^-$:DPA and PAAMPSA:DPA^+, the bond length decreased to 1.84 Å. When both species were charged, as for $PAAMPSA^-$:DPA^+, the bond length further shrank to 1.52 Å, suggesting a significant enhancement in bonding strength; the origin of this enhancement can be attributed to complementary ion pairing between negatively charged $PAAMPSA^-$ and positively charged DPA^+.

The stabilization of PANI via specific interactions with PAAMPSA and $PAAMPSA^-$ was verified by calculating the corresponding interaction energies (E_{int}) (Table 2.1). To compare possible interactions with the electrolyte that might lead to undesired side-reactions, the interaction energy of PANI with an aprotic solvent (ethylene carbonate, EC) was also estimated. The calculated interaction energies of DPA and DPA^+ with PAAMPSA and $PAAMPSA^-$ were all higher than those with ethylene carbonate; thus, polyaniline"s amine hydrogen atoms favorably bind with PAAMPSA rather than the electrolyte. $PAAMPSA^-$:DPA^+ possessed the highest interaction energy, -94.7 kcal mol^{-1}, which we attribute to the charge–charge interaction of the ion pair. This interaction is much stronger than normal hydrogen bonding, and significant charge transfer (0.19 e) was observed from $PAAMPSA^-$ to DPA^+ (Figure 2.14). In particular, this pair is expected to be extremely stable for cases where polyaniline carries a positive charge, as in the emeraldine salt and pernigraniline salt states.

2.4 CONCLUSIONS

In conclusion, PANI:PAAMPSA is a promising electrode material for electrochemical energy storage because of its ability to withstand highly oxidizing conditions. This feature is facilitated by a polyacid that essentially stabilizes PANI via specific interactions. Of significance, the pernigraniline salt form of polyaniline, which is normally highly unstable, was prepared, characterized, and shown to be stable even under highly oxidizing potentials. We envision that PANI:PAAMPSA‟s oxidative stability will enable many other applications, where PANI homopolymer was previously utilized such as fuel cells, sensors, energy storage systems, organic electronics, electrochromics, and antistatics. Also being water-dispersible and water-stable, PANI:PAAMPSA can be processed in water using a variety of techniques (i.e. spin-casting, ink jet printing, layer-by-layer assembly) that were inaccessible or challenging for PANI homopolymer. Its stable performance over hundreds of cycles suggests that PANI:PAAMPSA could be a suitable electrode material for composites with electrochemically active inorganics ($LiCoO_2$, $LiFePO_4$). Our future work will investigate the layer-by-layer assembly of PANI:PAAMPSA as well as composites with graphene.

CHAPTER III

CHARGE STORAGE IN POLYMER ACID-DOPED POLYANILINE-BASED LAYER-BY-LAYER ELECTRODES*

3.1 INTRODUCTION

Conjugated polymers, such as polypyrrole,[37, 187] polythiophene,[20, 188] polyacetylene,[189] and polyaniline,[190, 191] have been extensively studied as electrode materials in electrochemical energy storage systems. Among them, polyaniline (PANI) has attracted significant interest as an electrode material because of its high capacity,[46, 192] good conductivity,[193] unique doping/dedoping process,[194] and ease of synthesis.[195] PANI stores charge through reduction and oxidation, or dedoping and doping, respectively. In non-aqueous electrolyte systems, polyaniline reversibly switches between leucoemeraldine base and half-doped emeraldine salt oxidation states. However, even at moderately oxidizing potentials (~3.5 V vs. Li/Li^+), PANI gradually loses its electrochemical activity during cycling due to irreversible oxidation to pernigraniline base.[196, 44] Accordingly, there is significant interest in electroactive polymers that are capable of achieving reversible charge storage at potentials greater than 3.5 V vs. Li/Li^+ so that higher doping levels, capacities, and energies can be achieved.[197]

One such promising candidate to emerge is polyaniline:poly(2-acrylamido-2-methyl-1-propane sulfonic acid) (PANI:PAAMPSA) complex. It was recently

*Reprinted with permission from "Charge storage in polymer acid-doped polyaniline-based layer-by-layer electrodes" by Ju-Won Jeon, Josh O'Neal, Lin Shao, and Jodie L. Lutkenhaus, ACS Appl. Mater. Interfaces 2013, 5, 10127-10136, Copyright (2013) American Chemical Society

demonstrated that PANI:PAAMPSA could reversibly store charge even at highly oxidizing potentials (~4.5 V vs. Li/Li^+), which led to doping levels near 0.8 and enhanced cycle life relative to PANI homopolymer.[44] It was proposed that the origin of PANI:PAAMPSA‟s stability arose from electrostatic and hydrogen bonding interactions between protonated amines and sulfonic acid groups. This complex, previously explored for transistors,[158] electrochromic devices,[158] and sensors,[198] was formed by the polymerization of aniline monomer in the presence of PAAMPSA. The resulting PANI:PAAMPSA product was a negatively charged, water dispersible colloid.[44, 155] In a cast film, PANI:PAAMPSA exhibited a conductivity of 0.4 S/cm, which could be enhanced to 40 S/cm with dichloroacetic acid treatment.[158]

Motivated by these previous results, we hypothesized that PANI:PAAMPSA could be adapted for layer-by-layer (LbL) assembly to form thin film electrodes for energy storage. To fully leverage PANI:PAAMPSA‟s ability to reversibly store charge at elevated voltages, it is desirable to pursue alternative processing methods, such as LbL assembly. This technique, which is based on the alternate adsorption of oppositely charged species, is a versatile method for fabricating thin films and coatings.[96, 111] Film thickness can be easily controlled, and properties can be finely tuned by controlling pH and ionic strength.[92, 199, 200] The process is generally water-based and can proceed via dipping, spin-coating,[201] or spraying.[202] One unique feature of LbL assembly is that it can conformally deposit films onto a variety of surfaces (silicon, ITO-coated glass,[196] carbon paper, etc.).

LbL assembly has been widely applied to form electrodes for electrochemical energy storage. Kim et al. fabricated LbL electrodes of multi-wall carbon nanotubes (MWNTs), which resulted in a high surface area electrode that delivered the highest energy per unit area among reported LbL electrodes (300 μW h cm^{-2} at 0.4 mW cm^{-2}). Electrodes for microbatteries or electrochemical capacitors were assembled from PANI nanofibers and MWNTs, which maintained 75% of its initial capacity (160 mAh/cm^3) at 7.2 A/cm^3.[94] Interestingly, the PANI nanofiber/MWNT LbL electrodes were reversible up to 4.5 V vs. Li/Li^+, but extensive thermal treatment was required. Intimate mixing of cathode materials such as V_2O_5 and PANI has been demonstrated via LbL assembly.[196] If PANI:PAAMPSA were to be incorporated into similar electrodes, one might be able to enhance conductivity and attain reversible charge storage at high potentials, without the need for thermal treatment.

To date, there are no prior existing reports of PANI:PAAMPSA in LbL assemblies, so it is not immediately clear whether PANI:PAAMPSA can be assembled or processed via this technique. Earlier work with poly(3,4-ethylenedioxythiophene) (PEDOT):PSS, which is synthesized in a fashion similar to PANI:PAAMPSA, demonstrated its successful incorporation into an LbL assembly.[203, 204] The electrochromic activity of PEDOT:PSS was retained in the LbL assembly and good contrast between bleached and colored states was demonstrated. These results suggested that PANI:PAAMPSA, because it is structurally similar to PEDOT:PSS, might be suitable for LbL assembly; however, even if assembled into an LbL electrode, it is not known if PANI:PAAMPSA would retain its stability and reversible charge storage.

Here, the successful LbL assembly of PANI:PAAMPSA with complementary polycations is presented for the first time, as is the retention of its reversible charge storage. To assess the nature charge storage, three different polyaniline-based LbL electrodes comprised of PANI/PAAMPSA, PANI/PANI:PAAMPSA, and linear poly(ethylenimine)/PANI:PAAMPSA are compared. The first system is proposed as an LbL mimic of the PANI:PAAMPSA complex and the second is proposed as an electrode with high PANI-content. The last electrode isolates the performance of the PANI:PAAMPSA alone within the LbL assembly because poly(ethylenimine) is not electrochemically active. The growth and structure of the LbL electrodes are characterized using profilometry, zeta potential, UV-vis spectroscopy, Fourier transform infrared (FTIR) spectroscopy, and quartz crystal microbalance (QCM). Charge storage is assessed using cyclic voltammetry, and galvanostatic charge-discharge cycling. These results provide general guidelines for the assembly of PANI:PAAMPSA in LbL films and also demonstrate their potential as electrochemically active components in electrodes.

3.2 EXPERIMENTAL SECTION

For materials, PANI, dimethylacetamide (DMAc), hydrochloric acid, aniline, (3-aminopropyl)triethoxysilane (APTES), propylene carbonate, lithium perchlorate, and ammonium peroxydisulfate were purchased from Sigma Aldrich. Poly(2-acrylamido-2-methyl-1-propanesulfonic acid) (PAAMPSA, 10.36 wt% in water, Mw ~ 800 kg/mol) was purchased from Scientific Polymer Products. Linear poly(ethylenimine) (LPEI)

(Mw ~ 25,000) was obtained from Polysciences. Indium-tin oxide (ITO)-coated glass was obtained from Delta Technologies. Lithium metal was obtained from Alfa Aesar.

PANI:PAAMPSA was synthesized according to previous reports.[44, 154] Briefly, 5.8 g PAAMPSA (0.028 mol) was dissolved in 375 ml deionized water. Aniline (2.6 g, 0.028 mol) was mixed with the PAAMPSA solution and stirred for 1 h. Ammonium peroxydisulfate (5.8 g, 0.025 mol) was also dissolved in 25 ml deionized water separately. Both aniline-PAAMPSA and ammonium peroxydisulfate solutions were purged with nitrogen. Ammonium peroxydisulfate solution was added drop-wise to aniline-PAAMPSA solution, and polymerization was carried out at 5 °C for 24 h. Then, acetone was added to precipitate the PANI:PAAMPSA, which was filtered and washed with acetone to remove unreacted monomer and oligomer. The isolated PANI:PAAMPSA colloid was dried under vacuum at room temperature overnight.

PANI:PAAMPSA (0.2 g) was dispersed in 400 ml of deionized water by 10 h mild sonication. To prevent overheating during sonication, ice was added to the bath. After sonication, the pH of the PANI:PAAMPSA dispersion was adjusted to 2.5 using dilute HCl.

PANI dispersion was prepared as described by previously.[102, 196] The emeraldine base form of PANI (0.2 g) was dissolved in 40 ml of DMAc, stirred for 12 h and sonicated for 10 h. The resulting solution was then filtered through a 0.7 μm glass filter. The filtrate was slowly added to pH 3.0-3.5 deionized water (360 ml). The resulting mixture was then quickly adjusted to pH 2.5, and filtered again before use.

For the PAAMPSA solution, PAAMPSA (0.2 g) was mixed with 400 mL DI water. For the LPEI solution, LPEI (0.2 g) was also dissolved in 400 mL DI water, and the pH was adjusted to 2.5. PANI/PAAMPSA, PANI/PANI:PAAMPSA and LPEI/PANI:PAAMPSA LbL films were built onto APTES-treated, ITO-coated glass substrates. First, ITO-coated glass was sonicated sequentially in dicholoromethane, acetone, methanol and deionized water for 15 min each. After washing, the ITO-coated glass was then stored in deionized water before use. When ready for use, the washed ITO-coated glass was then blown dry using nitrogen gas and placed in a convection oven at 50 °C. The substrates were then exposed to oxygen plasma (Harrick PDC-32G) for 5 min, and then immediately immersed in 2 vol % APTES in toluene for 30 min at 75 °C.[44, 161] APTES-treated substrates were washed with toluene, ethanol, and finally deionized water. The substrates were then blown with nitrogen gas to remove remaining deionized water and placed in an oven at 110 °C for 15 min.

LbL assembly was carried out using an automated slide stainer (HMS Series, Carl Zeiss, Inc.). The APTES-treated substrates were immersed in the dispersion (or solution) containing the negatively charged species (PANI:PAAMPSA or PAAMPSA) for 15 min and rinsed in three different deionized water baths for 2 min, 1 min and 1 min. The substrates then were immersed in the dispersion (or solution) containing the positively charged species (PANI or LPEI) for 15 min, followed by rinsing again as before. This cycle was repeated until the desired number of layer pairs was achieved. For LbL assembly, the pH of all solutions and dispersions was adjusted to 2.5. The

assembled film is denoted as (cationic species/anionic species)$_n$, where n is number of layer pairs.

Profilometry (P-6, KLA-Tencor) was used to measure the thickness of the LbL film. Five locations per sample were measured, and the average value was taken as its thickness. UV-Vis spectroscopy of the assembled films was measured using a Hitachi U-4100 spectrometer. For the measurement, bare ITO-coated glass was used as a baseline. To obtain the density and composition of each LbL film, quartz crystal microbalance (QCM, Inficon) was employed. A 5 MHz Ti/Au quartz crystal was washed and exposed to oxygen plasma for 5 min. Then, the bare crystal was measured as the baseline. LbL assembly was carried out on the quartz crystal as described earlier. Before the QCM measurement, the LbL-coated quartz crystal was dried under nitrogen for 10 min in order to remove remaining water. Fourier transform infrared (FTIR) spectroscopy was performed using a Bruker Optics Spectrometer (ALPHA-P 10098-4) with 2 cm^{-1} resolution; samples were scanned 1,024 times, and bare ITO-coated glass was used as a baseline. Zeta potential and dynamic light scattering (DLS) measurements were carried out using a Zetasizer (Nano ZS90, Malvern Instruments); for the measurement, the concentration of the dispersion was adjusted to 0.005 wt%. The electrochemical properties of the LbL films were assessed in a three-electrode cell. LbL-coated ITO-coated glass was used as the working electrode, and lithium ribbon was used as the counter and reference electrodes. 0.5 M $LiClO_4$ dissolved in propylene carbonate was used as an electrolyte. All electrochemical measurements were performed using a Solartron SI 1287 at room temperature in a water-free, oxygen-free glovebox (< 2 ppm

each, MBraun). Before electrochemical tests, LbL films were placed under vacuum and then immersed in electrolyte solution for 12 h. Prior to electrochemical experiments, LbL films were conditioned via repeated cycling. For conditioning, cyclic voltammetry (1.5 V to 3.5 V) was performed 20 times and 30 times for PANI/PAAMPSA and PANI/PANI:PAAMPSA LbL electrodes, respectively. For LPEI/PANI:PAAMPSA LbL films, cyclic voltammetry (1.5 V to 4.5 V) was carried out 250 times as conditioning. Discussed later, these voltages were selected based on the relative observed cyclability of the LbL electrodes. All voltages reported are reported vs. Li/Li^+. Conductivity was measured using a home-built four point probe.

From QCM and profilometry data, the density of each LbL film was calculated. For 40 layer pairs, the mass per unit area was obtained using QCM. Then, a portion of the film was removed from the QCM crystal using a wet cotton swab. The step change in thickness between coated and coated regions was then recorded using profilometry. The density of the LbL film was calculated from the mass per unit area divided by thickness. For example, the areal mass and thickness of a $(PANI/PANI:PAAMPSA)_{40}$ LbL film were 32 ug/cm^2 and 302.2 nm, respectively. The density of this film was calculated as $\frac{32\ ug/cm^2}{302.2\ nm} \times \frac{1\ g}{10^6\ ug} \times \frac{10^7\ nm}{1\ cm} = 1.06\ g/cm^3$.

3.3 RESULTS AND DISCUSSION

Three different LbL electrodes were assembled: PANI/PAAMPSA, PANI/PANI:PAAMPSA and LPEI/PANI:PAAMPSA. The motivation was to incorporate electrochemically inactive components (PAAMPSA and LPEI) so as to

isolate the individual contributions of electrochemically active components (PANI and PANI:PAAMPSA). At pH 2.5, the zeta potentials of PANI and PANI:PAAMPSA colloids were +30 mV and -33 mV, respectively, which indicated that both species were sufficiently charged for successful LbL assembly. As expected, the PANI:PAAMPSA colloid was negatively charged due to excess sulfonic acid groups, whereas PANI was positively charged due to protonated nitrogens along the PANI backbone. Hydrodynamic diameters of PANI and PANI:PAAMPSA were measured using DLS and were 174 nm and 574 nm in pH 2.5 water, respectively.

Growth profiles for each LbL system exhibited very different behavior (Figure 3.1a). PANI/PAAMPSA and PANI/PANI:PAAMPSA LbL films grew linearly by 5.1 nm and 4.8 nm per layer pair, respectively. On the other hand, the LPEI/PANI:PAAMPSA LbL films grew slowly for the first fifteen bilayers, and then grew rapidly after fifteen bilayers (about 63 nm per layer pair). This type of growth profile was similar to those previously observed for other LbL systems such as poly(ethylene oxide)/poly(acrylic acid) and poly(ethylene oxide)/poly(methacrylic acid),[205, 206] where growth proceeded regularly following an induction period during which growth is non-uniform and characterized by island-like growth.

The roughness of each system was investigated by comparing the root-mean-square (RMS) roughness measured using profilometry. For LbL films consisting of 40

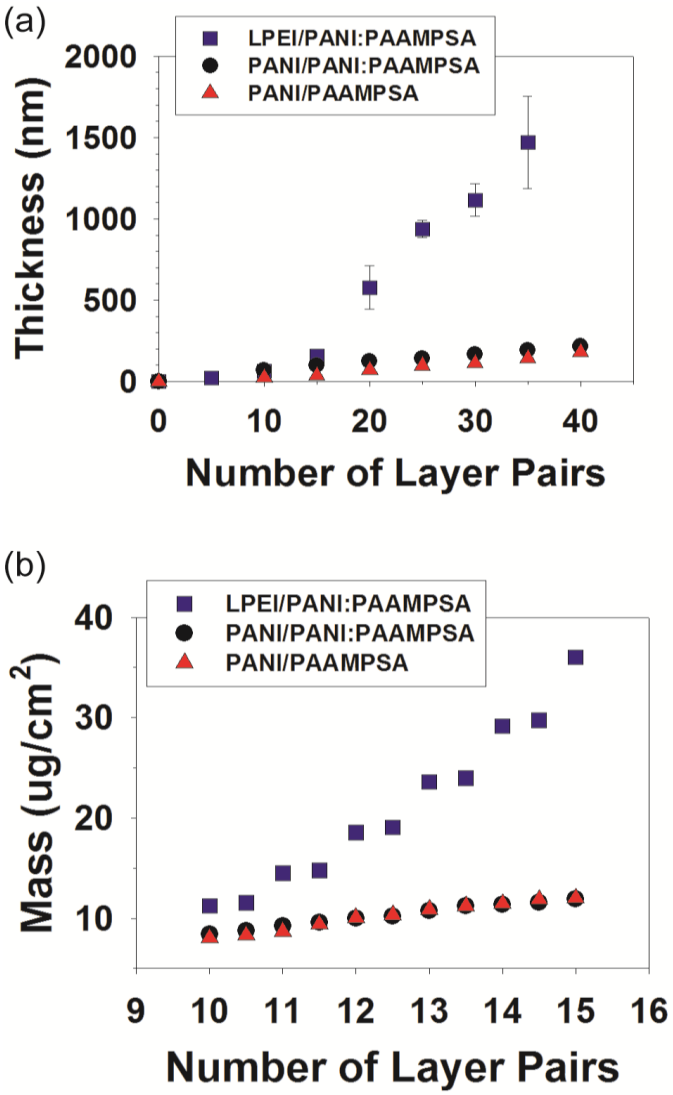

Figure 3.1. (a) Growth profiles and (b) adsorbed mass of LPEI/PANI:PAAMPSA, PANI/PANI:PAAMPSA, and PANI/PAAMPSA LbL films and obtained using profilometry and QCM, respectively. Error bars indicate standard deviation. In most cases, the error was smaller than the plotted data symbol.

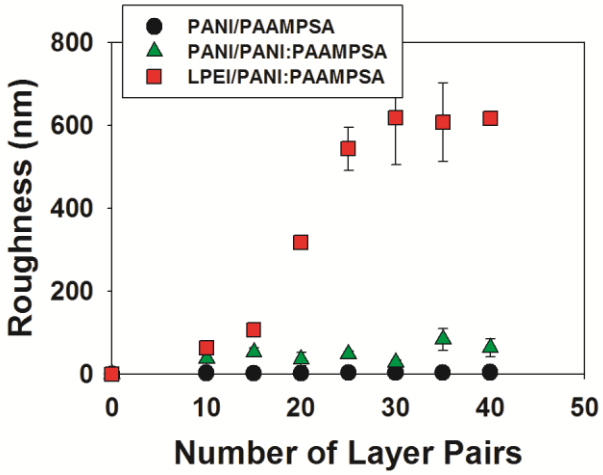

Figure 3.2. Root mean square roughness of PANI/PAAMPSA, PANI/PANI:PAAMPSA, and LPEI/PANI:PAAMPSA LbL films.

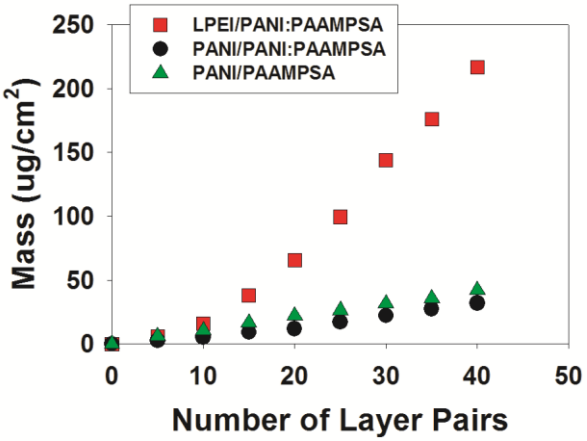

Figure 3.3. Growth profile of (a) PANI/PAAMPSA, (b) PANI/PANI:PAAMPSA, and (c) LPEI/PANI:PAAMPSA LbL films using QCM.

Table 3.1. Cationic Species, Anionic Species, and Total PANI Content in PANI/PAAMPSA, PANI/PANI:PAAMPSA, and LPEI/PANI:PAAMPSA LbL films.

	Cationic Species (wt%)	Anionic Species (wt%)	Total PANI (wt%)
PANI/PAAMPSA	51	49	51
PANI/PANI:PAAMPSA	46	53	59
LPEI/PANI:PAAMPSA	8	92	23

layer pairs, $(LPEI/PANI:PAAMPSA)_{40}$, $(PANI/PAAMPSA)_{40}$, and $(PANI/PANI:PAAMPSA)_{40}$ LbL films had RMS roughnesses of 600, 4.4 and 63.3 nm, respectively (Figure 3.2). Interestingly, the RMS roughness of $(LPEI/PANI:PAAMPSA)_{40}$ LbL films was similar to that of the hydrodynamic diameter of PANI:PAAMPSA complex (574 nm, measured using DLS). The exceptionally rough LPEI/PANI:PAAMPSA LbL surface is possibly linked to the film‟s non-linear growth and the relatively large size of PANI:PAAMPSA colloids. It is known that globular polyelectrolytes and colloids can engender non-linear growth due to increasing surface roughness, which induces fractal-like growth. For example, LbL assemblies of poly(hexylviologen) and poly(3,4 – ethylenedioxythiophene):poly(styrene sulfonate) showed behavior much like what was observed here (non-linear growth, large RMS roughness that increased with number of layer pairs).[203]

The composition of the LbL films, obtained using QCM,[207, 208] allowed for an accurate determination of the films‟ PANI content, Figure 3.1b, 3.3, and Table 3.1. The

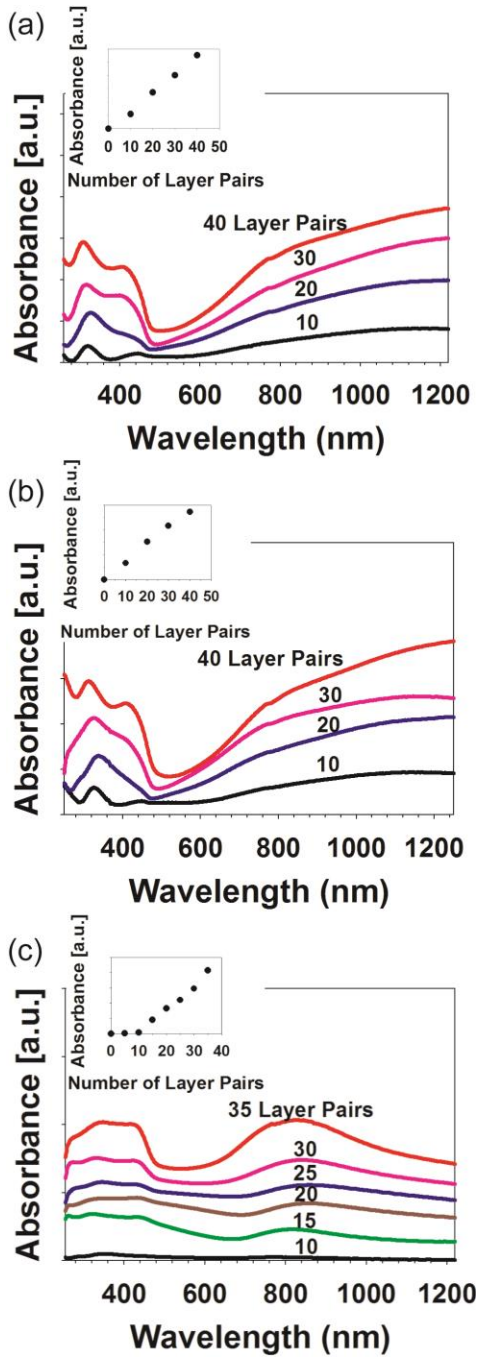

Figure 3.4. UV-vis spectra of (a) PANI/PAAMPSA, (b) PANI/PANI:PAAMPSA, and (c) LPEI/PANI:PAAMPSA LbL films. The insets are UV-vis absorbance intensity at 830 nm versus number of layer pairs.

mass adsorbed was measured every layer from ten to fifteen layer pairs for dry LbL films, enabling the calculation of the weight fraction of anionic and cationic species adsorbed. For PANI/PAAMPSA and PANI/PANI:PAAMPSA LbL films, the weight ratio of cationic to anionic species was nearly 1:1. However, in the case of LPEI/PANI:PAAMPSA LbL films, PANI:PAAMPSA was the dominant species (92 wt% of PANI:PAAMPSA and 8 wt% of LPEI). This phenomenon might be explained by considering the fact that PANI:PAAMPSA colloids (574 nm) are much larger than LPEI polymer chains (here, Mw ~ 25,000), so the sizes are severely mismatched. A similar mismatch in composition was observed for LbL films composed of SiO_2 and TiO_2, where the particles sizes were highly dissimilar (22 vs. 7 nm, respectively).[105]

To improve our understanding of the high degree of asymmetry in composition, the ratio of surface area to volume was also calculated for both PANI:PAAMPSA and LPEI. This quantity represents the area and volume over which charge is distributed. Using hydrodynamic radii of 287 nm (measured here using DLS) and 6.4 nm (from ref [209]) for PANI:PAAMPSA and LPEI, respectively, R^2/R^3 could be roughly estimated to be 0.0035 and 0.16 nm^{-1}. Assuming that charge is distributed uniformly along the surface, that PANI:PAAMPSA and LPEI have equal densities, and that charge neutrality holds within the LbL film, one can roughly state that the charge on an individual PANI:PAAMPSA complex is much more diffuse than the charge on an LPEI chain. Following this reasoning, more PANI:PAAMPSA is adsorbed than LPEI, which maintains charge neutrality, leading to a film composition with a high degree of asymmetry.

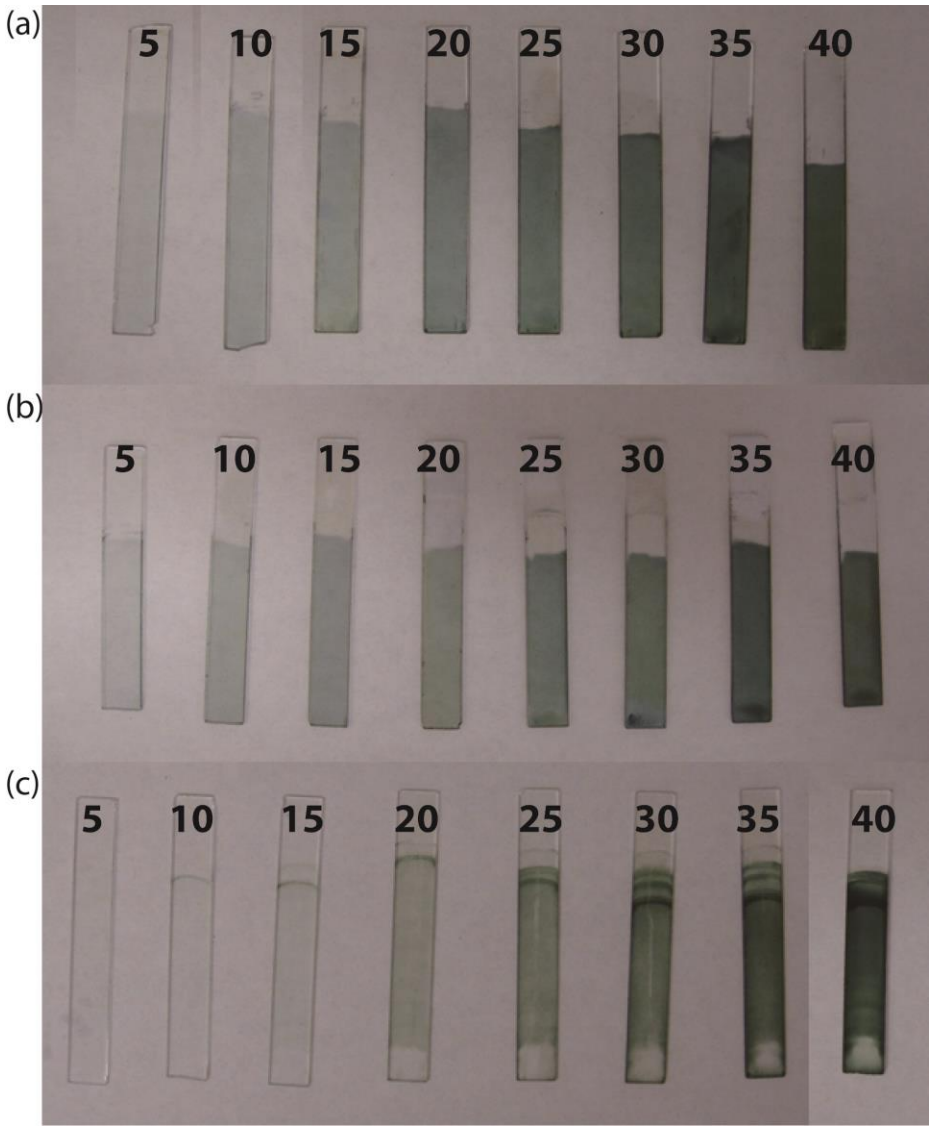

Figure 3.5. Digital images of (a) PANI/PAAMPSA, (b) PANI/PANI:PAAMPSA, and (c) LPEI/PANI:PAAMPSA LbL films with increasing number of layer pairs.

Because PANI:PAAMPSA contains 25 wt% PANI,[44] the LbL films‟ total PANI content could also be estimated, Table 1. Here, it was assumed that PANI:PAAMPSA

remains intact during the LbL assembly process because of the strong interactions between PANI and PAAMPSA.[44] Electrochemical characterization presented later support the validity of this assumption. Of the three systems investigated, PANI/PANI:PAAMPSA LbL films contained the highest weight fraction of PANI (59 wt%), of which 78 wt% originated from PANI layers and 22 wt% originated from PANI:PAAMPSA layers.

Using data from QCM and profilometry, the density of each LbL system was estimated. Details regarding the density calculation are available in the Supporting Information. The PANI/PAAMPSA LbL film was the densest, at 1.28 g/cm^3, followed by LPEI/PANI:PAAMPSA at 1.2 g/cm^3. PANI/PANI:PAAMPSA LbL films were the least dense, at 1.06 g/cm^3; this lower density presumably arises from the nature of the adsorbing species, where both are colloidal particles and pack less efficiently. In contrast, the other denser LbL films consisted of colloidal particles and polyelectrolytes, which perhaps packed more efficiently due to the flexibility of PAAMPSA or LPEI chains.

UV-vis spectra indicate that PANI exists as conductive emeraldine salt in each of the as-assembled LbL electrodes investigated, Figure 3.4. In PANI/PAAMPSA and PANI/PANI:PAAMPSA LbL systems, peaks near 310 nm and 420 nm were observed as well as a long absorption band (600~1200 nm). The 310 nm peak is attributed to the π-π^* transition of PANI"s benzenoid ring.[44, 148, 154, 155, 158, 210-212] The peak at 420 nm and long absorption band in the near-IR region are ascribed to polaron bands, which are characteristic of conductive emeraldine salt.[158, 167, 212] The trend in absorbance at 830 nm vs. the number of layer pairs (Figure 3.4 insets) of mimicked the growth profiles

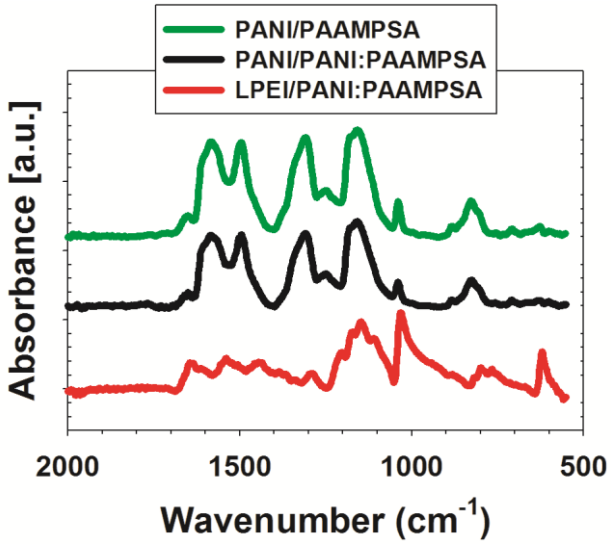

Figure 3.6. FTIR spectra of PANI/PAAMPSA, PANI/PANI:PAAMPSA, and LPEI/PANI:PAAMPSA LbL films.

obtained via profilometry. As the number of layer pairs increased, each LbL electrode investigated became a darker shade of green (Figure 3.5), consistent with film growth.

In the case of LPEI/PANI:PAAMPSA LbL films, the behavior slightly deviates from the other two LbL systems. A maximum peak at 825 nm was observed as well as peaks at 340 nm and 430 nm. The red-shift of the benzenoid π-π* transition peak can be ascribed to interactions between PANI:PAAMPSA and LPEI. It has been reported that electron-withdrawing groups lower the energy level of the lowest unoccupied molecular orbital (LUMO), which leads to redshifted absorption bands.[211, 213] Also, the absorbance value from 1000 to 1200 nm for LPEI/PANI:PAAMPSA LbL films significantly decreased as compared to PANI/PAAMPSA and PANI/PANI:PAAMPSA LbL films.

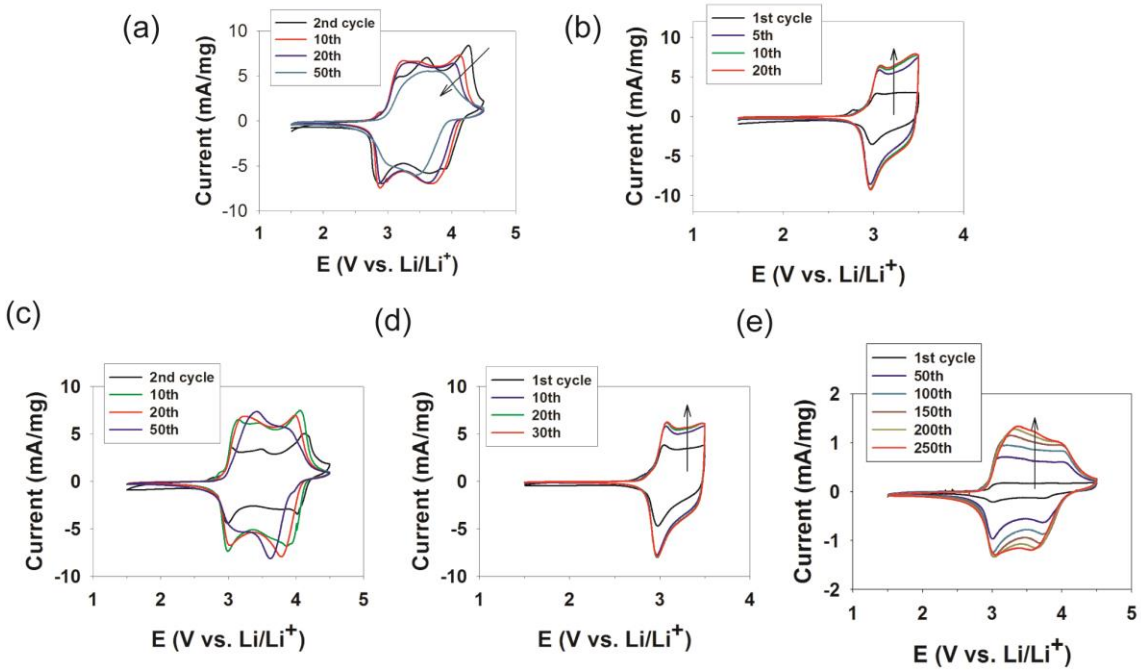

Figure 3.7. Cyclic voltammograms of a PANI/PAAMPSA LbL electrode (a) from 1.5 V to 4.5 V and (b) from 1.5 V to 3.5 V; a PANI/PANI:PAAMPSA LbL electrode (c) from 1.5 V to 4.5 V and (d) from 1.5 V to 3.5 V; and an LPEI/PANI:PAAMPSA LbL electrode (e) from 1.5 V to 4.5 V. All films were about 200 nm thick. The current was reported per mg of PANI, and the scan rate was 10 mV/s.

This decrease in absorbance suggests that PANI chains residing in PANI:PAAMPSA colloid are more coiled as compared to PANI chains residing in as-synthesized PANI homopolymer.[154, 158, 214, 215] This finding compliments prior work, which has demonstrated that PANI chains residing within a PANI:PAAMPSA complex have an intrinsically coiled confirmation.[92, 158]

FTIR spectroscopy confirmed the chemical structure of the LbL films (Figure 3.6). PANI/PAAMPSA and PANI/PANI:PAAMPSA FTIR spectra were similar to that of spectra for polyaniline homopolymer.[44, 186, 216-218] Peaks at 1585 cm^{-1} and 1480 cm^{-1} are ascribed to quinoid and benzenoid ring structures, respectively.[186, 216, 218,] Several peaks at 1648 cm^{-1}, 1038 cm^{-1}, and 625 cm^{-1} are attributed to S=O, SO_3H, and N-H (amide), respectively, originating from PAAMPSA.[44, 167] In addition, the peak around 1155 cm^{-1} indicates the presence of hydronium sulfonate salts.[219] In the case of LPEI/PANI:PAAMPSA LbL films, FTIR spectra were very similar to spectra from the other two systems but with a notable exception. Peaks associated with benzenoid (1440 cm^{-1}) and quinoid (1540 cm^{-1}) rings shifted to lower wavenumbers as compared the other systems, which may be explained by interactions between PANI:PAAMPSA and LPEI.[220, 221]

Our prior work with PANI:PAAMPSA has shown that charge can be reversibly stored up to 4.5 V vs. Li/Li^+.[44] By extension, the PANI/PAAMPSA LbL film, representing the LbL analogue of the PANI:PAAMPSA complex obtained via template polymerization, could presumably possess similar exceptional reversibility at high voltages. To test this hypothesis, cyclic voltammetry was carried out for 200 nm thick $(PANI/PAAMPSA)_{40}$, $(PANI/PANI:PAAMPSA)_{40}$, and $(LPEI/PANI:PAAMPSA)_{16}$ LbL films in a three-electrode cell, Figure 3.7. Of the three electrodes investigated, only the LPEI/PANI:PAAMPSA LbL electrode demonstrated reversibility when cycled between 1.5 and 4.5 V vs. Li/Li^+, Figure 3.7e. For the other two systems, the current decreased as the electrode was cycled (Figure 3.7a and c), indicating a decrease in the electrochemical

activity of electrodes likely attributed to the irreversible oxidation of emeraldine salt to pernigraniline base.[44] On the other hand, for LPEI/PANI:PAAMPSA LbL films, the current continuously increased up to 250 cycles and then stabilized (Figure 3.7e). This phenomenon is termed conditioning, and is discussed later. However, the current (per mass of PANI) was much smaller than those of PANI/PAAMPSA and PANI/PANI:PAAMPSA LbL electrodes. This fact suggests that the electrochemical activity of LPEI/PANI:PAAMPSA LbL films was much smaller than those of PANI/PAAMPSA and PANI/PANI:PAAMPSA LbL films. We attribute the low electrochemical activity of LPEI/PANI:PAAMPSA LbL electrodes to its low PANI content, which perhaps leads to difficulty in forming electronically percolative domains. This idea is supported by the fact that a four point probe was unable to measure the conductivity of an LPEI/PANI:PAAMPSA LbL electrode. In contrast, the conductivities of PANI/PANI:PAAMPSA and PANI/PAAMPSA LbL electrodes were measureable, having values of 0.067 S/cm and 8.4×10^{-5} S/cm, respectively.

These findings show that reversible charge storage at high voltages is retained for PANI:PAAMPSA complex within an LbL film. On the other hand, the PANI/PAAMPSA LbL film, which was intended to mimic the PANI:PAAMPSA complex did not possess good reversibility. We can infer from these results that the stability arises from the structure of the complex itself and not the LbL assembly. Within the PANI:PAAMPSA complex, PANI is intimately intertwined with PAAMPSA as a result of template polymerization. Within the PANI/PAAMPSA LbL assembly, PANI

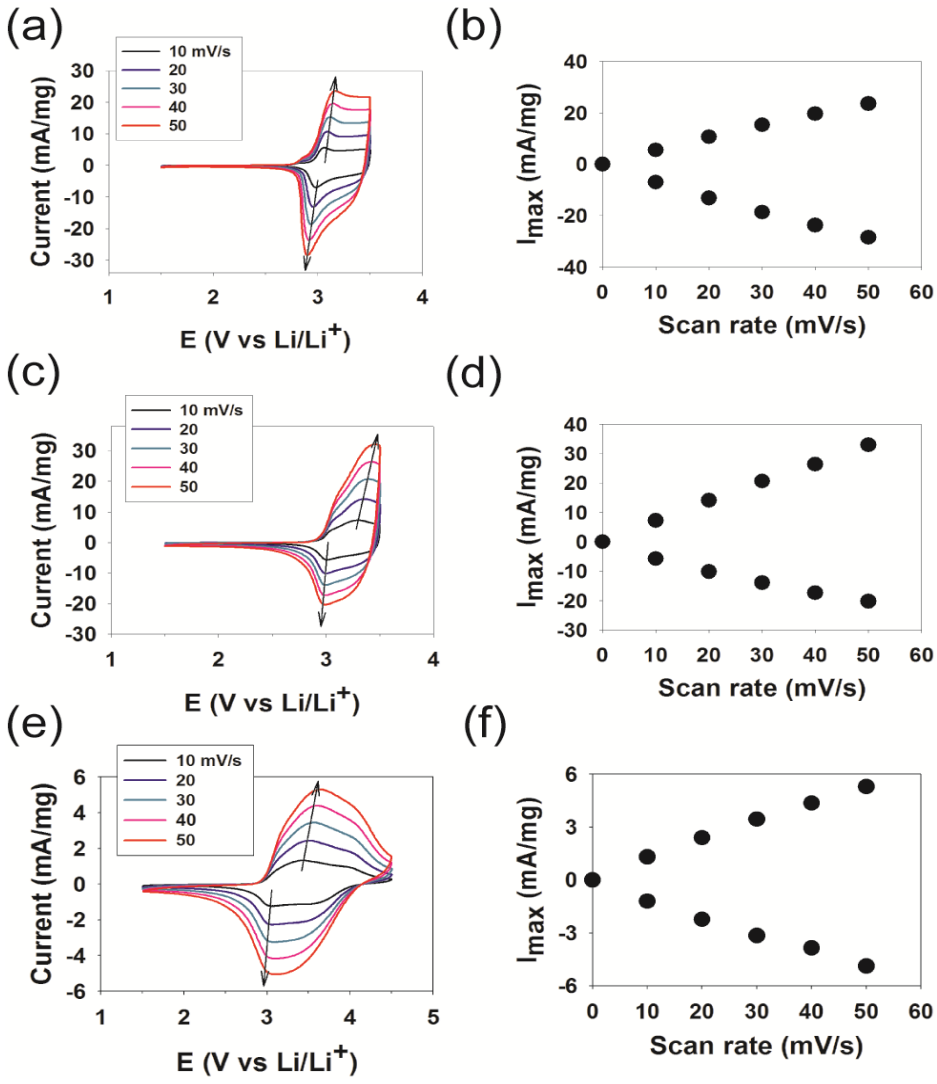

Figure 3.8. Cyclic voltammograms of (a) PANI/PAAMPSA, (c) PANI/PANI:PAAMPSA, and (e) LPEI/PANI:PAAMPSA LbL electrodes. (b, d, and f) Plots of the first peak"s current versus scan rate using data from cyclic voltammograms (a, c, and e, respectively). The current was reported per mg of PANI. Each of the electrodes had been conditioned as described in the Experimental Section.

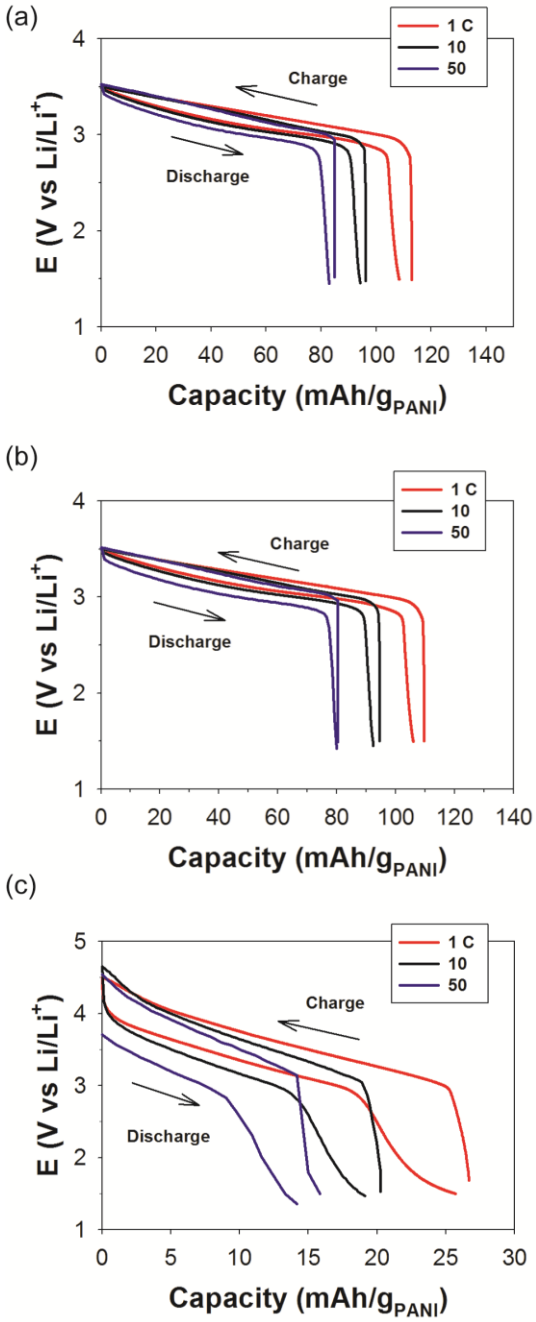

Figure 3.9. Galvanostatic charging and discharging of (a) PANI/PAAMPSA, (b) PANI/PANI:PAAMPSA, and (c) LPEI/PANI:PAAMPSA LbL electrodes after conditioning. The capacity is based on the mass of PANI in the electrode. Each of the electrodes had been conditioned as described in the Experimental Section.

exists as a colloidal particle rather than an individual polyelectrolyte chain and there are fewer PANI-PAAMPSA interactions as compared to the analogous complex.

When the upper voltage was decreased from 4.5 to 3.5 V versus Li/Li^+, PANI/PAAMPSA and PANI/PANI:PAAMPSA LbL electrodes exhibited a greater degree of reversibility and stability (Figure 3.7b, d). For the former, the current increased and then saturated after 20 cycles, and for the latter, 30 cycles were required to reach saturation. The gradual increase in current with cycling is termed "conditioning," and has been observed on several other occasions.[44, 174-176, 196, 222] According to those reports, this phenomenon results from (1) the displacement of hydronium ions (associated with sulfonic acid groups) with lithium ions and solvent[44, 174-176] and/or (2) gradual penetration of the electrolyte into the electrode during cycle.[196, 222]

Having identified the optimum operating voltages and conditioning treatment for each LbL electrode, cyclic voltammetry was carried out to determine the types of electrochemical reactions present and whether they are reaction- or diffusion-controlled, Figure 3.8. For PANI/PAAMPSA and PANI/PANI:PAAMPSA LbL films, the maximum cutoff voltage was 3.5 V because rapid degradation was observed at higher voltages for those LbL films. For LPEI/PANI:PAAMPSA LbL films, the maximum voltage was 4.5 V vs. Li/Li^+. A pair of redox peaks associated with the conversion of fully reduced leucoemeraldine base to emeraldine salt around 3 V consistently appeared for all systems,. From 3 V to 3.5 V, a plateau region, arising from continuous faradaic charge transfer, was also observed.[44, 177] In the case of LPEI/PANI:PAAMPSA LbL films, a pair of redox peaks at 3.8 V appeared, which was assigned to the conversion of

Table 3.2. Capacity (mAh/g_{PANI}) of PANI/PAAMPSA, PANI/PANI:PAAMPSA, and LPEI/PANI:PAAMPSA LbL films at different C rates.

	1 C	2 C	5 C	10 C	20 C	50 C
PANI/PAAMPSA	109	104	99	94	89	84
PANI/PANI:PAAMPSA	106	102	97	92	87	80
LPEI/PANI:PAAMPSA	26	23	21	19	18	16

emeraldine salt to fully oxidized pernigraniline salt.[44] Plots of the maximum current vs. the scan rate displayed a linear relationship, which was indicative of a surface-confined redox process.[196, 223] This finding was reasonable considering that the electrodes tested in this study were approximately 200 nm thick.

The capacity and cycle life were assessed for each type of conditioned LbL electrode at various C rates using galvanostatic charging and discharging within the previously determined voltage windows (Figure 3.9 and Table 2). The C rate was calculated as the current required to discharge the theoretical capacity of the electrode in 1 h, represented as 1 C; a C rate of 5 C represents discharge in 1/5 h and so forth. Both PANI/PAAMPSA and PANI/PANI:PAAMPSA LbL electrodes stored far more energy than the LPEI/PANI:PAAMPSA electrode on a per gram of polyaniline basis. The former two electrodes‟ capacity declined by 23−25% as the discharge rate increased from 1 to 50 C, and the later electrode‟s capacity declined by 38%.

When compared against polyaniline‟s theoretical capacity, difference in charge storage among the electrodes becomes even more apparent. For cycling between 1.5 and

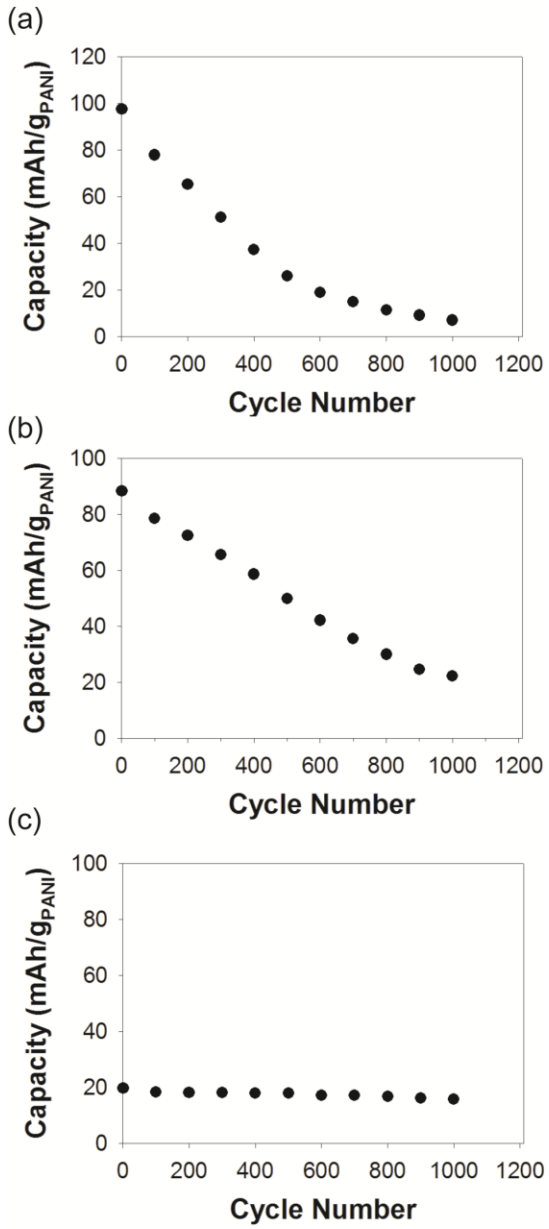

Figure 3.10. Cycling tests of (a) PANI/PAAMPSA, (b) PANI/PANI:PAAMPSA, and (c) LPEI/PANI:PAAMPSA LbL electrodes. Electrodes from (a) and (b) were cycled between 1.5 and 3.5 V and (c) was cycled between 1.5 and 4.5 V vs. Li/Li^+. Capacity is reported on a basis of the mass of PANI in the electrode. Each of the electrodes had been conditioned as described in the Experimental Section.

3.5 V, as was done for PANI/PAAMPSA and PANI/PANI:PAAMPSA LbL electrodes, PANI switches between leucoemeraldine base and emeraldine salt forms (theoretical capacity of 147 mAh/g_{PANI});[44] between 1.5 and 4.5 V, as was done for LPEI/PANI:PAAMPSA LbL electrodes, PANI switches between leucoemeraldine base and pernigraniline salt forms (theoretical capacity of 294 mAh/g_{PANI}).[44] At low C rates, both PANI/PAAMPSA and PANI/PANI:PAAMPSA LbL electrodes have capacities slightly above 100 mAh/g_{PANI}, or two-thirds of their theoretical capacity. In comparison, LPEI/PANI:PAAMPSA LbL electrodes had a capacity of 26 mAh/g_{PANI}, or less than one-tenth of its theoretical capacity. This low capacity is most likely a result of the electrode‟s low conductivity.

Galvanostatic cycling at a rate of 10 C between voltages of 1.5 and 3.5 V for PANI/PAAMPSA and PANI/PANI:PAAMPSA and 1.5 and 4.5 V for LPEI/PANI:PAAMPSA LbL electrodes was performed to characterize each system‟s cyclability. Panels a and b of Figure 3.10 show that PANI/PAAMPSA and PANI/PANI:PAAMPSA LbL electrodes have high initial capacities but poor cycle lives. The initial capacity of the PANI/PAAMPSA LbL electrode was 97 mAh/g of PANI (Figure 3.10a), which gradually declined with continued cycling. Approximately half of the initial capacity was lost after 300 cycles, and then after 1000 cycles, the capacity of the PANI/PAAMPSA LbL electrode was around 7 mAh/g of PANI. Similarly, the initial capacity of PANI/PANI:PAAMPSA LbL films was 88 mAh/g, and then after 550 cycles, its capacity decreased by half (Figure 3.10b). After 1000 cycles, only 20 mAh/g of PANI of capacity was retained.

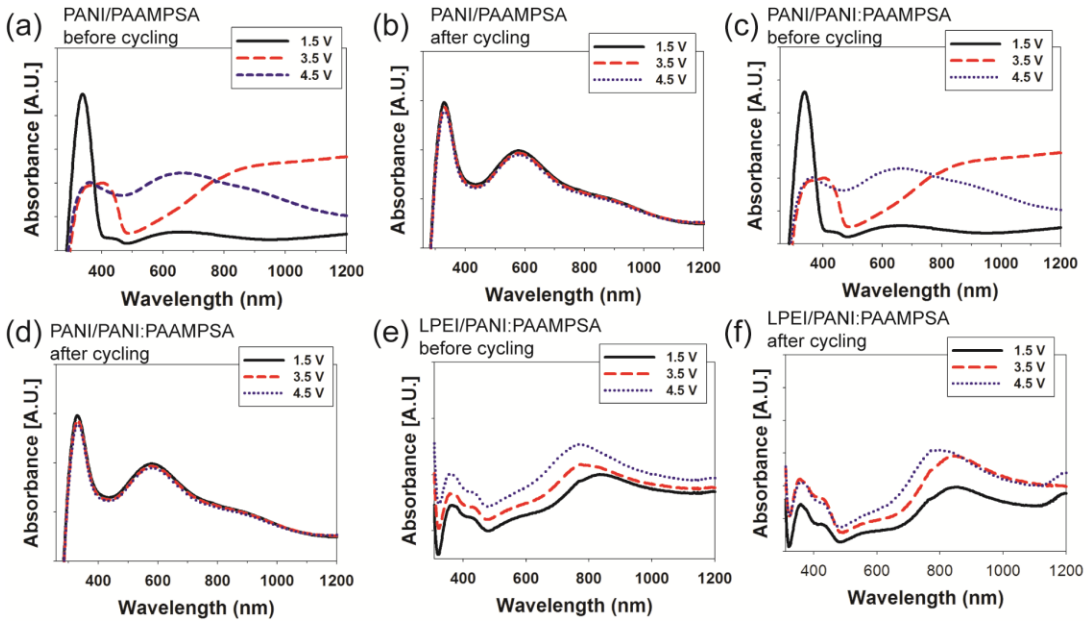

Figure 3.11. UV-vis spectra of PANI/PAAMPSA LbL electrodes (a) before and (b) after cycling; PANI/PANI:PAAMPSA LbL electrodes (c) before and (d) after cycling; and LPEI/PANI:PAAMPSA LbL electrodes (e) before cycling and (f) after cycling. All electrodes were cycled from 1.5 V to 4.5 V at a rate of 10 C.

We had initially hypothesized that PANI/PAAMPSA LbL electrodes would possess reversibility on par with PANI:PAAMPSA complex, but galvanostatic cycling (Figure 3.10a) clearly disproves this hypothesis. The fact that the capacity of PANI/PAAMPSA LbL electrodes declined, even under moderate potentials of 1.5 V to 3.5 V, suggests that PANI/PAAMPSA LbL electrodes are not as intimately mixed as PANI:PAAMPSA complex obtained via template polymerization. Results from cyclic voltammetry also support this idea, Figure 3.8. PANI/PANI:PAAMPSA LbL electrodes

present an intermediate case (Figure 3.10b), where the capacity declines more rapidly than LPEI/PANI:PAAMPSA (Figure 3.10c) but less so than PANI/PAAMPSA LbL electrodes. It can be inferred from these results that PANI:PAAMPSA sustains its electrochemical activity while PANI degrades with repeated cycling.

On the other hand, the LPEI/PANI:PAAMPSA LbL electrode was the most reversible and bore the longest cycle life, albeit with lowest capacity (20 mAh/g of PANI), Figure 3.10c. Because PANI:PAAMPSA‟s reversibility at high potentials was retained within LbL assemblies, it can be concluded that the interactions between PANI and PAAMPSA were maintained and that LPEI did not significantly disrupt the PANI:PAAMPSA structure.[44] Although the LPEI/PANI:PAAMPSA conductivity was quite low, we attribute the low conductivity LPEI which perhaps formed a barrier to charge transport from complex to complex or layer to layer. The fact that a PANI/PANI:PAAMPSA LbL electrode was conductive suggests that PANI:PAAMPSA could maintain a percolative network and would, therefore, be a suitable additive for enhancing conductivity in electroactive LbL assemblies or composites.

Previously, we have shown via UV-vis spectroscopy and density functional theory modeling that PANI and PANI:PAAMPSA convert to pernigraniline base and pernigraniline salt, respectively, following repeated cycling up to 4.5 V in non-aqueous conditions.[44] Reasonably, UV-vis spectra of the three LbL systems can also be used to elucidate PANI‟s oxidation state as a basis for each system‟s stability or instability. UV-vis spectra were collected after the electrode was held at a given potential (1.5, 3.5, and 4.5 V) before and after cycling between 1.5 and 4.5 V(Figure 3.11).

Before cycling, PANI/PAAMPSA and PANI/PANI:PAAMPSA UV-vis spectra were similar to each other, (Figure 3.11a, c). At 1.5 V, an absorbance peak at 335 nm (π-π^* transition) was characteristic of leucoemeraldine base.[148, 196] At 3.5 V, an additional peak appeared at 420 nm as well as a long absorption band (600 nm to 1200 nm), which was typical of conductive emeraldine salt.[148, 167] At 4.5 V, a broad peak appeared at 660 nm appeared, which was the typical characteristic of pernigraniline salt.[145, 224] However, after 1000 cycles (Figure 3.11b, d), both PANI/PAAMPSA and PANI/PANI:PAAMPSA LbL electrodes converted to pernigraniline base (maximum peak ~ 580 nm), regardless of the voltage applied. The fact that the UV-vis spectra remained unchanged regardless of voltage after cycling indicated that the formation of pernigraniline base was irreversible.[44, 196] Conversely, LPEI/PANI:PAAMPSA LbL films exhibited spectra characteristic of emeraldine salt regardless of the applied potential both before and after cycling. The lack of clear electrochromic switching associated with the LPEI/PANI:PAAMPSA LbL film was another indication of its low electrochemical activity.

3.4 CONCLUSIONS

Three different polyaniline-based LbL electrodes (PANI/PAAMPSA, PANI/PANI:PAAMPSA, and LPEI/PANI:PAAMPSA) were successfully constructed for the first time. The nature of charge storage in each system was investigated and compared. PANI:PAAMPSA complex maintained its ability to reversibly store charge (up to 4.5 V vs. Li/Li^+) within the LPEI/PANI:PAAMPSA LbL assembly, which leads

to high cyclability. After 1000 cycles between 1.5 and 4.5 V, no significant decrease in capacity was observed. In contrast, PANI/PAAMPSA and PANI/PANI:PAAMPSA LbL electrodes had larger initial capacities (> 100 mAh/g of PANI) because of their higher PANI content, but these same electrodes suffered from poor cyclability attributed to the irreversible formation of pernigraniline base. Also, the electrochemical reversibility of the PANI:PAAMPSA complex appears to be unique to the method of its synthesis, considering that an analogous LbL assembly of PANI and PAAMPSA was unable to emulate a similar reversibility.

This work has provided general guidelines for the incorporation of PANI:PAAMPSA into LbL assemblies, and it will now be possible to combine PANI:PAAMPSA with other active electrode materials via LbL assembly in the future. Furthermore, PANI:PAAMPSA is a promising candidate for LbL electrodes because it is both conductive and electrochemically active. An example of one such future application could be LbL hybrid electrodes containing non-conductive transition metal oxides.

CHAPTER IV

POLYANILINE NANOFIBER/ELECTROCHEMICALLY REDUCED GRAPHENE OXIDE LAYER-BY-LAYER ELECTRODES FOR ENERGY STORAGE

4.1 INTRODUCTION

Thin film energy storage is growing in importance as demand for micro-power sources in wearable personal electronics, drug delivery, sensors, pacemakers, smart cards, and radio frequency identification (RFID) tags deepens.[225-227] Thin film Li-ion batteries are one such example, in which the electrodes are well below 100 microns in thickness.[228-230] Such examples have been demonstrated in MEMs devices, textiles, acoustic telemetry systems, and conductive paper.[231-234] In some applications, it is desired to integrate multifunctionality (i.e., energy storage capabilities) into a predefined object of interest via advanced coating methods. In this regard, thin film energy is particularly promising. Further, materials utilization is enhanced in thin film electrodes because of the reduced diffusion path for ions involved in the redox process.[230] Here, we present a facile route to produce hybrid cathodes comprised of polyaniline nanofibers and electrochemically reduced graphene oxide via layer-by-layer assembly, a conformal coating technique. The result is a water-processable, porous, binder-free, thin film cathode for energy storage capable of coating a variety of surfaces.

Lithium-ion batteries are widely used in various consumer electronic devices due to their great electrochemical performance such as relatively high capacity and energy density.[3, 235] A typical cathode may contain $LiCoO_2$, a polymeric binder, and carbon

additives; this configuration typical gives a capacity, operating voltage and specific energy of 140 mAh/g, ~4.0 V, and 400-600 mWh/g_{LiCoO2}, respectively.[236,237, 238] Other cathode materials, such as $LiFePO_4$, V_2O_5, polypyrrole, polythiophene, and polyaniline, have been implemented or proposed as alternatives to $LiCoO_2$.[239-243] These alternatives promise safer operation, greater materials availability, and reduced cost.

Carbon materials such as carbon nanotubes and graphene have been explored as active cathode components, owing to their conductivity and – in some cases - pseudocapacitance.[244-249] Graphene, a two-dimensional sheet of sp^2-hybridized carbon often compared to an un-rolled carbon nanotube, is particularly interesting as an electrode material for thin film batteries because of its high electron mobility, excellent mechanical strength, high thermal conductivity, and high surface area (theoretically up to 2630 $m^2\ g^{-1}$).[55-58] Because of these excellent properties, graphene has been explored in various applications including sensors, solar cells, tissue engineering, drug delivery, and energy storage.[57, 250-254] In energy storage systems, graphene has been widely employed as an electrode material itself or as a conductive additive.[27, 57, 250, 254, 255] For example, the conductivity of compressed chemically reduced graphene oxide (CRGO) powder was 200 S/m.[256] Graphene stores charge both via an electric double-layer mechanism and a pseudocapacitive mechanism originating from the rapid redox reaction of oxygen-containing functional groups on the graphene sheet.[63, 94, 125, 249, 257] For example, partially reduced graphene oxide electrodes have reported reversible capacities up to 120-200 mAh/g.[249, 258]

Graphene can be prepared using various methods including mechanical exfoliation, chemical vapor deposition, epitaxial growth, and chemical reduction of graphene oxide.[53, 62, 259-261] Chemical reduction of graphene oxide is a particularly promising method because it offers low-cost, large-scale production of CRGO,[261] but processability has been somewhat limited. For example, CRGO is dispersible in some optimized mixed solvents and basic aqueous conditions, but forms irreversible aggregates in neutral and acidic aqueous conditions.[256, 259, 262] This limited processability, originating from CRGO‟s hydrophobic nature and its relatively low oxygen-containing functional group content, can be circumvented by utilizing graphene oxide (GO) sheets instead. Following GO processing, CRGO product can be obtained using reducing agents such as hydrazine.[262] Recently, the electrochemical reduction of processed GO sheets has been demonstrated, thus eliminating the need for harsh reducing agents.[72, 263]

Polyaniline (PANI), a p-type conjugated polymer, has also been explored as an electrode material for energy storage due to its high theoretical capacity (assuming full doping, neglecting the mass of the anion: 294 mAh g^{-1}), good conductivity, low cost, and ease of synthesis.[13, 56, 58, 239] PANI stores charge through a doping/dedoping mechanism, in which anions transport in and out of the electrode as PANI is oxidized and reduced, respectively. Accordingly, mass transport of the dopant ion is a potential issue, especially for dense PANI electrodes. In this regard, PANI nanofibers (PANI NFs) are promising because they assemble into porous, high surface area electrodes. PANI nanofibers can be synthesized rapidly in water, and remain dispersed in a water-processable state for days.[195, 264] PANI NF electrodes exhibited capacities in the range of

75-165 mAh/g as cathodes in non-aqueous cells, demonstrating their ability to store charge.[265, 266]

Layer-by-layer (LbL) assembly is a conformal coating technique recently demonstrated for the formation of thin film battery and supercapacitor electrodes, [13, 52, 63, 94, 267] and relies upon the alternate adsorption of complementary species from water (or other media).[96] Film properties can be controlled by altering assembly conditions (pH and ionic strength),[268-270] and films can be deposited onto a variety of surfaces (silicon, glass, metal, indium-tin oxide, poly(tetrafluoroethylene)).[52, 271-274] Hammond and Shao-Horn demonstrated high-capacity (200 mAh/g) multiwalled carbon nanotube (MWNT) LbL electrodes, which relied upon charge storage arising from MWNTs‟ oxygen-containing functional groups.[63] Our group has demonstrated PANI/V_2O_5 LbL battery electrodes with high capacity of up to 264 mAh/g.[13, 240] Elsewhere, PANI/ERGO LbL supercapacitor electrodes were investigated.[267] The PANI/ERGO LbL electrodes possessed a high capacitance of 1563 F/cm^3 in aqueous media; although these results are promising, the electrodes presented were 70 nm thick, which is exceedingly thin. There should exist some balance between an electrode‟s total capacity (increases with increasing thickness) and materials utilization (decreases with increasing thickness).

Here, we present assembly of and charge storage in PANI NF/ERGO LbL electrodes for use in non-aqueous thin film batteries. PANI NFs and ERGO sheets both store charge and provide conductivity to the resulting electrode. The PANI NFs produce a porous architecture, thus facilitating mass transport. To date, PANI NF/ERGO LbL electrodes have not been demonstrated nor has their performance as cathodes in non-

aqueous batteries. First, this report describes the LbL assembly of PANI NFs and GO sheets, for which pH is used as a tuning parameter for LbL growth. Assembly with CRGO is compared to GO sheets, and it is shown that GO is far more versatile in LbL processing. The resulting PANI NF/GO LbL films were successfully reduced electrochemically. No additional reducing agents or thermal treatments were required. This report then focuses upon charge storage in PANI NF/ERGO LbL electrodes as battery cathodes in non-aqueous media. Special attention is paid towards charge storage as a function of electrode thickness, in which the highest capacity was 461 mAh/g for a 460 nm film at 0.1 A/g. It is further shown that polyaniline‟s stability is enhanced through interactions with ERGO sheets. The electrodes can be conformally coated onto a variety of surfaces, perhaps presenting a suitable approach toward multifunctional energy storage.

4.2 EXPERIMENTAL SECTION

For materials, Aniline, ammonium peroxydisulfate, propylene carbonate, lithium perchlorate, potassium permanganate, (3-aminopropyl)triethoxysilane (APTES), and sodium nitrate were purchased from Sigma Aldrich. Graphite (SP-1) was purchased from Bay Carbon. Lithium foil and Indium-tin oxide (ITO)-coated glass (resistance < 20 ohms) were purchased from Alfa Aesar and Delta Technologies, respectively. Separator (Celgard 3501) was provided by Celgard.

PANI NFs were synthesized using a previously reported method.[195] Aniline (1.49 g) was dissolved in 1M HCl of 50 ml. Ammonium peroxydisulfate (0.915 g) was

dissolved in 1M HCl of 50 ml, separately. Before synthesis, each solution was purged with nitrogen for more than 30 min. Then, the ammonium peroxydisulfate solution was rapidly mixed with the aniline solution under nitrogen at room temperature. The reaction was performed for 24 h. After polymerization, dialysis against deionized water was employed to remove remaining initiator (ammonium peroxydisulfate) and unreacted monomer (aniline) for at least 24 h. The yield of PANI NFs with respect to aniline monomer was approximately 17 wt%. The concentration was adjusted to 0.5 g/ml by adding deionized water for LbL assembly. The PANI NF dispersion was stable in acidic aqueous solution (pH 2.5) for a week. Therefore, synthesized PANI NFs were used within a few days following dilution. PANI NFs were approximately 50 nm in diameter, Figure 4.1a.

For the synthesis of graphene oxide sheets (GO), first, graphite oxide was synthesized using modified Hummer"s method.[275] Graphite power (SP-1, 3 g) and $NaNO_3$ (2.5 g) were added into concentrated H_2SO_4 (120 ml), and stirred for 5 h in an ice water bath. $KMnO_4$ (15 g) was slowly added to the above mixture for 30 min while stirring. During $KMnO_4$ addition, the temperature of the mixture was maintained below 20 ^oC using ice. Then, the above mixture was stirred at 35 ^oC for 2h, and slowly diluted with 250 ml chilled deionized water. Deionized water (700 ml) was added to the above dispersion in an ice water bath. Then, 30 wt% H_2O_2 (20 ml) was added to the above mixture. In this process, the color of the dispersion changed from black to brown. For washing, the dispersion was mixed with 5 wt% HCl (1 L), and stirred for several hours. It was dried and dialyzed against deionized water for at least three days to remove the

residual salt. Graphite oxide powder was obtained after drying at 60 ^{o}C under vacuum condition. The synthesized graphite powder was dissolved in deionized water and sonicated at 100 W for 30 min to yield GO sheets. The dropcast GO sheets exhibited wrinkled planar structures, Figure 4.1b. Chemically reduced GO (CRGO) was prepared by reduction of GO dispersion using hydrazine in basic aqueous solution. After reduction, dialysis was performed in pH 10 water.

The synthesized PANI NFs and GO sheets were diluted to a concentration of 0.5 mg/ml in deionized water. The pH of the PANI NF dispersion was adjusted to 2.5 using HCl; to prevent aggregation, sonication was carried out for 30 min. The GO dispersion was also diluted to 0.5 mg/ml in deionized water, and HCl and NaOH were used to adjust the pH.

PANI NF/GO LbL films were assembled on APTES-treated ITO-coated glass substrates. For APTES treatment, ITO-coated glass substrates were cleaned by sequential sonication in dichloromethane, acetone, methanol, and deionized water for 15 min each. After washing, ITO-coated glass was dried using high-velocity nitrogen gas and dried in a convection oven. Plasma treatment (Harrick PDC-32G) was carried out on dry ITO-coated glass slides for 5 min; then, they were immediately immersed in 2 vol % APTES in toluene for 30 min at 75 ^{o}C.[52] After APTES treatment, the ITO-coated glass was washed with toluene, ethanol, and deionized water, separately. The APTES-treated slides were dried using high velocity nitrogen followed by heating for 15 min at 110 ^{o}C. For LbL assembly, APTES-treated ITO-coated glass substrates were immersed in graphene oxide dispersion for 15 min, and rinsed with deionized water for 2, 1, and 1

min each. The pH of the rinse baths following GO exposure was matched to that of the pH of the GO dispersion. Then, the substrates were immersed in pH 2.5 PANI NF dispersion for 15 min, and rinsed with pH 2.5 deionized water for 2, 1, and 1 min each. The same procedure was repeated until the desired thickness was achieved. For deposition onto cotton fabric, the fabric was immersed in pH 2 water before LbL assembly. In this case, a wringing step was included between the last washing step and the next immersion in dispersion. Other procedures were kept identical. The resulting films are denoted by (PANI NF_x/GO_y) LbL assemblies, in which the subscripts x and y denote the assembly pH of PANI NF and GO dispersions, respectively.

The thickness of PANI NF/GO LbL films was measured using profilometry (P-6, KLA-Tencor), and at least five different locations were measured and averaged. Quartz crystal microbalance (QCM) was employed to measure the mass of the LbL films. A 5 MHz Ti/Au quartz crystal was plasma-treated for 5 min. Then, the PANI NF/GO LbL film was assembled onto the quartz crystal using the assembly process described previously. Zeta-potential was measured using a Zetasizer (Nano ZS90, Malvern Instruments). UV−vis spectroscopy was performed using a Hitachi U-4100 spectrometer. X-ray photoelectron spectroscopy (XPS), (Kratos Axis Ultra DLD) was employed with a monochromatic Al (10 mA, 12 kV) X-ray source. To remove charging effects, the C 1s peak (284.5 eV) was used as a reference.

After LbL assembly, LbL films were dried in a hood for 24 h, and the vacuum-dried for 10 min. The electrochemical tests were carried out using either a three-electrode cell or a two-electrode sandwich-type cell. For the three-electrode cell, the

LbL-coated ITO slide was used as the working electrode, and lithium ribbons were used as counter and reference electrodes; 0.5 M $LiClO_4$ dissolved in propylene carbonate was used as an electrolyte. For the sandwich-type cell, LbL film on ITO-coated glass and lithium ribbon were used as working electrode and counter/reference electrodes, respectively. A separator was sandwiched between the LbL cathode and lithium anode in order to prevent short circuit, and 1 M $LiClO_4$ dissolved in propylene carbonate was used as an electrolyte.[52] All electrochemical tests were performed at room temperature in an oxygen-free and water-free argon-filled glove box. Electrochemical performance such as capacity, specific energy, and specific power were calculated based on the mass of the LbL film alone. Before measurements, electrochemical reduction at 1.5 V and conditioning (one hundred scans from 1.5 to 4.2 V at 20 mV/s) were conducted. The active area for the two-electrode cell and the three-electrode cell was 2 cm^2. Typical electrode thicknesses for the three-electrode and two-electrode cells ranges from 347 to 1520 nm.

4.3 RESULTS AND DISCUSSION

The LbL assembly of PANI NFs and GO sheets was investigated for various assembly pH values, as it has been shown that pH can strongly affect LbL growth.[71, 268] In this study, two different pH values (3.5 and 10) were chosen for the GO dispersion to control the surface charge of GO sheets, whereas the pH of the PANI NF dispersion was fixed at 2.5. At higher pH, PANI NF dispersion started to form aggregate. Therfore, it is difficult to obtain stable dispersion at higher pH. For LbL assembly, PANI NFs are

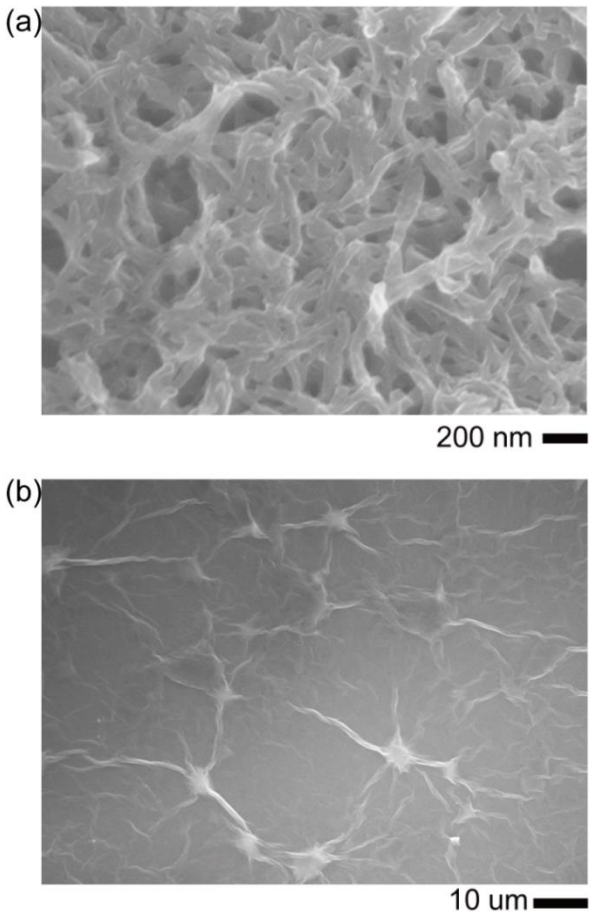

Figure 4.1. SEM images of drop-cast (a) PANI NFs and (b) GO sheets.

known to be only stable under acidic aqueous conditions.[52, 264] The zeta-potential of GO sheets is dependent on pH because of abundant oxygen-containing functional groups such as carboxylic acid and phenolic hydroxyls,[262] Figure 4.2. The zeta-potential of GO at pH values 3.5 and 10 was -31 and -43 mV, respectively, and that of PANI NFs was +35 mV; these values show that the nanomaterials are sufficiently charged for LbL assembly.

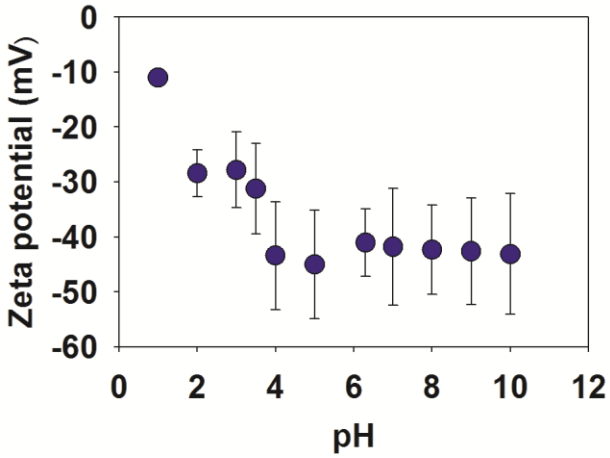

Figure 4.2. Zeta potential of GO dispersion in water at different pH values.

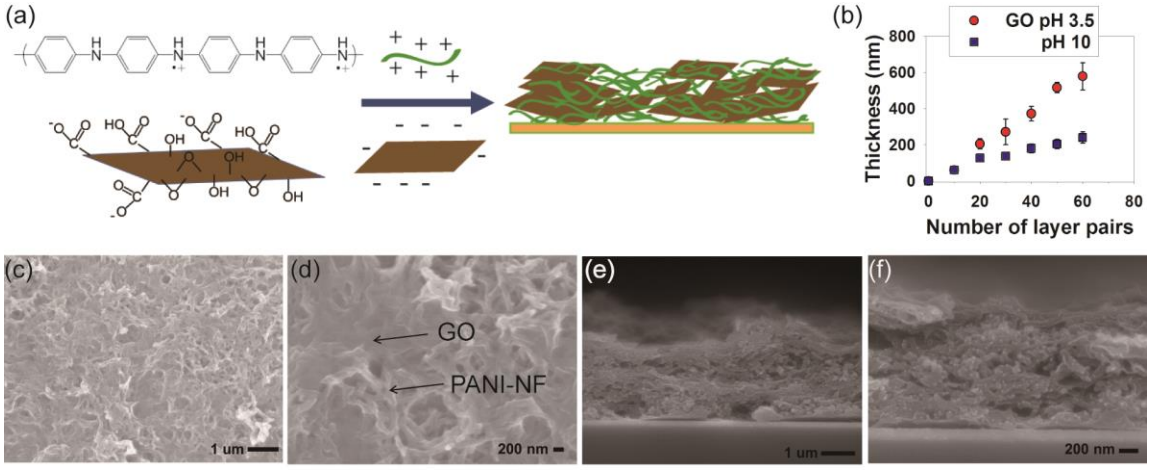

Figure 4.3. (a) LbL assembly of PANI NFs and GO sheets. (b) PANI NF/GO LbL thickness vs. number of layer pairs measured using profilometry for varying GO pH values. The pH of PANI NFs was fixed at 2.5. (c), (d) Top-view and (e), (f) cross-sectional SEM images of (PANI $NF_{2.5}$/$GO_{3.5}$) LbL electrodes.

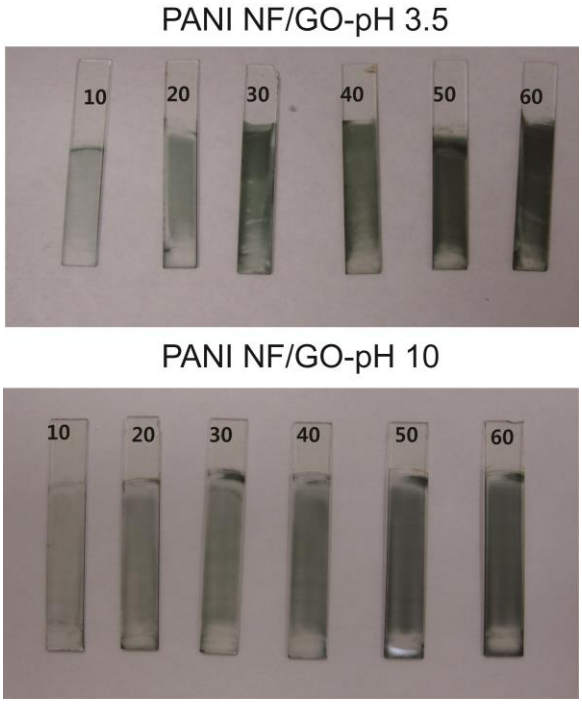

Figure 4.4. Digital images of PANI NF/GO LbL films on ITO-coated glass. The labels denote the number of layer pairs deposited.

PANI NF/GO electrodes were built up via LbL assembly, Figure 4.3a. For both assembly conditions, the electrodes were green in color and became successively darker with further cycles of deposition, Figure 4.4. The green color originated from the conductive emeraldine state of PANI.[52] Successful assembly was further confirmed by the linear increase in thickness per layer pair deposited, Figure 4.3b. Electrodes assembled at GO pH 3.5 exhibited a larger layer pair thickness (9.6 nm/layer pair) as compared to those assembled at GO pH 10 (4.0 nm/layer pair).

The difference in layer pair thickness probably stems from the variation in GO‟s surface charge with pH, as supported by zeta-potential measurements. GO sheets at pH 3.5 are less negatively charged as compared to those at pH 10 because carboxylate and phenolic acid groups are more likely to be ionized at higher pH values.[262] Therefore, in the case of less ionized GO sheets (pH 3.5), a larger amount of GO is required to reverse the surface‟s charge, leading to a larger thickness per layer pair. Similar phenomena have been observed in other LbL systems.[71, 268] For both PANI NF/GO LbL films, the average layer pair thickness was smaller than the PANI NF diameter (ca. 50 nm), which indicates that PANI NF/GO LbL films do not consist of distinctive PANI NF and GO layers. We speculate that this low layer pair thickness originates from patchy adsorption during assembly. The lack of discrete layers, however, may allow for intimate contact between PANI NFs and GO sheets.

The root-mean squared (RMS) roughness was measured using profilometry. Sixty layer pairs of (PANI $NF_{2.5}$/$GO_{3.5}$) exhibited an RMS roughness of 236 nm, whereas the RMS roughness of a comparable film at GO pH 10 was 141 nm. The difference might be attributed to the greater layer pair thickness for (PANI $NF_{2.5}$/$GO_{3.5}$) as compared to (PANI $NF_{2.5}$/GO_{10}) LbL electrodes.

We also attempted LbL assembly of PANI NFs and chemically reduced graphene oxide (CRGO) sheets. In this case, the pH of CRGO was maintained at pH 10 or higher because CRGO forms irreversible aggregates in neutral and acidic conditions.[262] However, during the assembly, film delamination and severe aggregation of CRGO occurred, suggesting that stability during LbL deposition is poor, even at pH 10. This

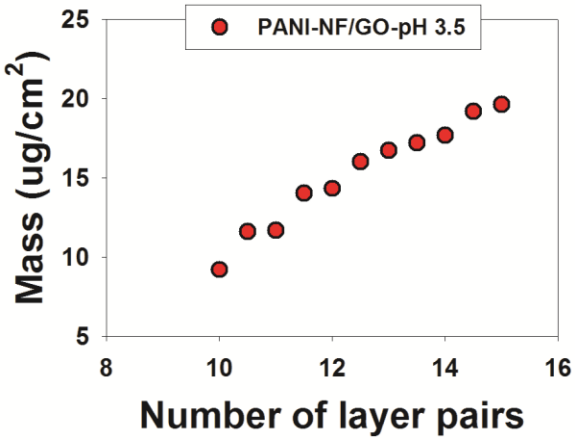

Figure 4.5. Adsorbed mass of (PANI-$NF_{2.5}$/$ERGO_{3.5}$) LbL electrodes measured using quartz crystal microbalance.

finding highlights the apparent challenge of conducting LbL assembly with CRGO sheets. By using GO sheets instead, one can circumvent this challenge.

The composition of PANI NF/GO LbL films was measured using QCM. PANI NFs were the dominant species within (PANI $NF_{2.5}$/$GO_{3.5}$) LbL films (77 wt% PANI NF and 23 wt% of GO), Figure 4.5. For (PANI $NF_{2.5}$/GO_{10}) LbL films, it was difficult to obtain reproducible data due to excessive noise in the data. The composition of the LbL film assembled for GO pH 10 is likely richer in PANI NFs because GO is more negatively charged at pH 10 so less GO is adsorbed. We selected the (PANI $NF_{2.5}$/$GO_{3.5}$) LbL system for further investigation because its layer pair thickness was sufficiently large so as to build up electrodes in a timely fashion.

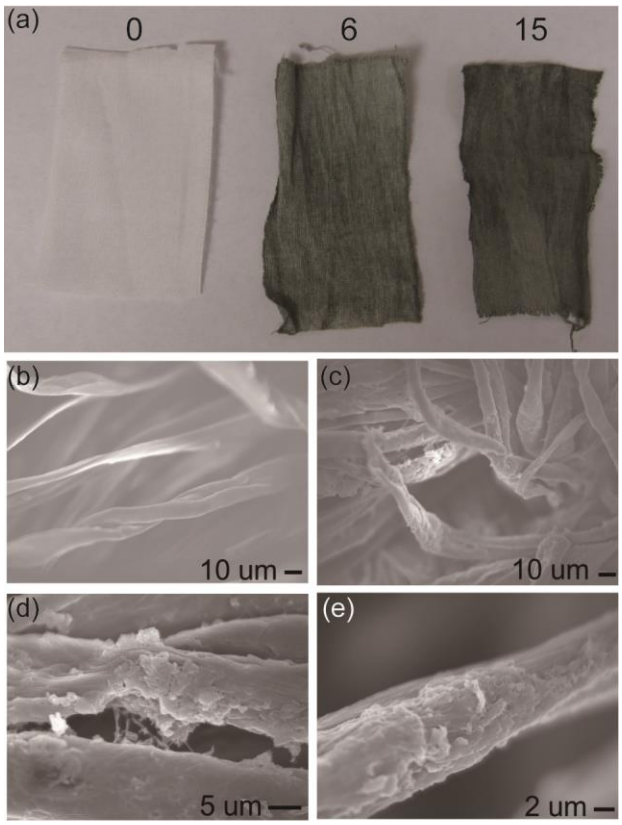

Figure 4.6. (a) Digital image of PANI NF/GO LbL films on cotton fabric, from left to right (0, 6 and 15 layer pairs). SEM images of (b) bare cotton fabric and (c-e) 15 layer pairs of PANI NF/GO on cotton fabric.

SEM images confirm the successful LbL assembly of (PANI $NF_{2.5}/GO_{3.5}$), Figure 4.3c-f. In top-view images, fibrous PANI NFs appear to be intimately mixed with GO sheets. Cross-sectional images of the LbL electrode also exhibit both PANI NFs and GO sheets. No distinguishable stratified layers are observed, consistent with our previous observation of patchy growth, which leads to intimate mixing of the two nanomaterials. The porous nature, arising from the presence of PANI NFs is clearly visible. From QCM

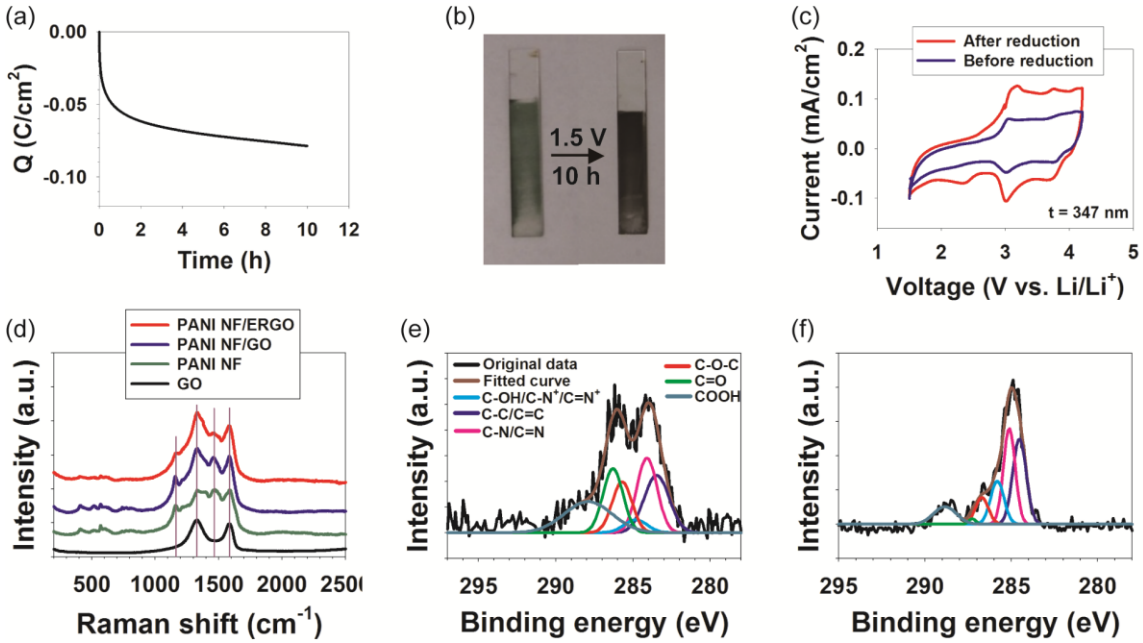

Figure 4.7. (a) Electrochemical reduction of a 271 nm thick (PANI $NF_{2.5}/GO_{3.5}$) LbL film, (b) digital images before and after reduction, (c) cyclic voltammograms of a 347 nm thick LbL electrode before and after reduction, and (d) Raman spectra of PANI NFs, GO sheets, (PANI $NF_{2.5}/GO_{3.5}$), and (PANI $NF_{2.5}/ERGO_{3.5}$) LbL electrodes. XPS spectra of (e) (PANI $NF_{2.5}/GO_{3.5}$) and (f) (PANI $NF_{2.5}/ERGO_{3.5}$) LbL electrodes. The legend in (e) also applies to panel (f).

and profilometry, the density of a 1116 nm thick (PANI $NF_{2.5}/GO_{3.5}$) LbL system was estimated as 0.56 g cm^{-3}, which confirms that the electrodes are very porous. This structure is advantageous for charge storage in that it leads to larger surface area and enhanced ion transport relative to a dense non-porous electrode.

The good processability of PANI NFs and GO sheets is further demonstrated by LbL assembly onto cotton fabric, Figure 4.6. As the number of layer pairs increased, the

cotton fabric grew darker in color indicative of LbL deposition, Figure 4.6a. In SEM images (Figure 4.6c-e), the LbL coating on individual cotton fibers was observable, which is in contrast to the bare fabric (Figure 4.6b), which displayed relatively smooth fiber surfaces.

After assembly, the LbL electrodes were electrochemically reduced at 1.5 V vs. Li/Li^+ in an organic electrolyte (0.5 M $LiClO_4$ in propylene carbonate) for 10 h. The purpose of this treatment was to electrochemically convert GO sheets to electrochemically reduced graphene oxide (ERGO) in the as-assembled electrode. As compared to conventional chemical reduction, no harsh reducing agents or additional purification steps were required. Figure 4.7a presents the charge transferred during the 10 h reduction period. Significant charge transfer was observed within the first hour, after which the amount of charge passed decreased. Upon electrochemical reduction, the LbL film‟s color changed from dark green to black, Figure 4.7b. Cyclic voltammetry of the electrodes before and after reduction indicates a larger current response for the electrochemically reduced electrode, Figure 4.7c. The change in color, coupled with the increased electrochemical activity, suggests that electrochemical reduction successfully converted GO to ERGO.

Raman spectroscopy was performed to further investigate the electrochemical reduction of (PANI $NF_{2.5}/GO_{3.5}$) LbL films, Figure 4.7d. For GO, the peaks centered at 1330 and 1580 cm^{-1} were observed, which were ascribed to D and G bands, respectively. The D band arises from defective carbon structures, and the G band is an indication of ideal graphitic sp^2 carbon.[24, 276] The Raman spectra of PANI NFs contains peaks at 1158,

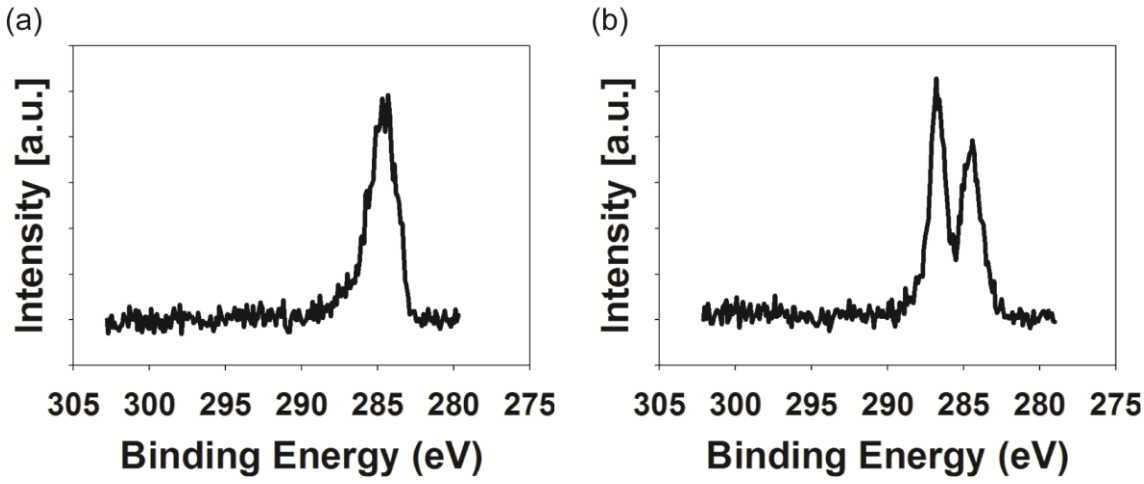

Figure 4.8. XPS of (a) PANI NFs and (b) GO sheets.

Table 4.1. The composition of C 1s peaks for (PANI $NF_{2.5}/GO_{3.5}$) and (PANI $NF_{2.5}/ERGO_{3.5}$) LbL electrodes.

	C-C/C=C 284.5 eV	C-N/ C=N 285.1 eV	C-OH/C-N^+/C=N^+ 285.8 eV	C-O-C 286.7 eV	C=O 287.3 eV	COOH 288.6 eV
PANI NF/GO	20.4 %	21.6 %	4.3 %	14.3 %	18.2 %	21.2 %
PANI NF/ERGO	31.6 %	30.9 %	15.9 %	9.5 %	1.1 %	11 %

1330-1440, 1480 and 1580 cm^{-1}, attributed to C-H bending, C-N^{*+}, C=N, and C-C stretching, respectively.[94, 277] As expected, (PANI $NF_{2.5}/GO_{3.5}$) LbL films had both peaks from PANI NFs and GO sheets. After electrochemical reduction, all peak positions remained the same; however, the ratio of the D to G band intensities increased from 1.14 to 1.24. This trend has been observed with other chemical reduction methods, in which the increased D/G ratio was attributed to a decrease in the size of sp^2 domains.[256, 278 278-280] Here, it can be inferred that electrochemical reduction results in new graphitic sp^2 domains having smaller sizes relative to the starting materials.

XPS was carried out on PANI NFs, GO sheets, (PANI $NF_{2.5}/GO_{3.5}$) and (PANI $NF_{2.5}/ERGO_{3.5}$) electrodes, Figure 4.7e-f and Figure 4.8. The C 1s region for GO sheets had two broad peaks at 284.5 and 286.8 eV, attributed to sp^2 graphitic domains and oxygen-containing functional groups, respectively. In (PANI $NF_{2.5}/GO_{3.5}$) LbL films, similar C 1s peaks were observed, but at reduced intensity for the 286.8 eV peak owing to dilution by the PANI NF component. For the (PANI $NF_{2.5}/GO_{3.5}$) LbL electrode, the C:O atomic ratio increased from 1.97 to 3.76 upon electrochemical reduction of GO to ERGO sheets. The decrease in apparent oxygen content suggests that electrochemical reduction reduces the quantity of oxygen-containing functional groups on the GO sheets.

To further investigate the effect of electrochemical reduction, the C 1s region was deconvoluted into six different Gaussian peaks centered at 284.5, 285.1, 285.8, 286.7, 287.3, and 288.6 eV, attributed to C-C/C=C, C-N/C=N, C-OH/C=N/C-N^+, C-O-C, C=O, and COOH groups, respectively[71, 281-284] (Figure 4.7e-f and Table 4.1). The amount of C-C/C=C (arising from sp^2 graphitic domains) increased while the amount of oxygen-

containing functional groups generally decreased following electrochemical reduction, indicating the restoration of a sp^2 carbon structure. In particular, ketone groups significantly decreased from 18.2 % to 1.1 % and COOH groups decreased from 21.2 to 11 % after electrochemical reduction. The percentage C-OH/C-N^+/C=N^+ increased upon reduction, the origin of which could be related to increased relative polyaniline content in LbL films. It is known that reduction of GO sheets liberates oxygen-containing functional groups in the form of CO, CO_2, H_2O and O_2.[285, 286] This mass loss from graphene oxide could increase the relative PANI content in LbL films. Overall, these XPS results further confirm the electrochemical reduction of PANI NF/GO LbL films, which is in accordance with Raman spectra.

Thin film electrodes for energy storage are promising because they offer high materials utilization without the need for binders or other additives.[230] However, it can become difficult to transport electrons and ions as the electrode's thickness increases. Therefore, we investigated the performance of LbL films of varying thickness, controlled by the number of LbL cycles performed. Further, it has been discussed that performance metrics of thin film electrodes become skewed, trending toward higher values, if reported on a per electrode mass basis; therefore, it is proposed that reporting performance metrics by volume or by area is more appropriate.[227, 287] Here, we present our results in terms of both electrode volume and mass so as to allow proper comparisons with prior literature, some of which reports on a per electrode mass basis.

The electrochemical performance of (PANI $NF_{2.5}$/$ERGO_{3.5}$) LbL electrodes was assessed in three-electrode cells. Before measurements, the electrode was conditioned

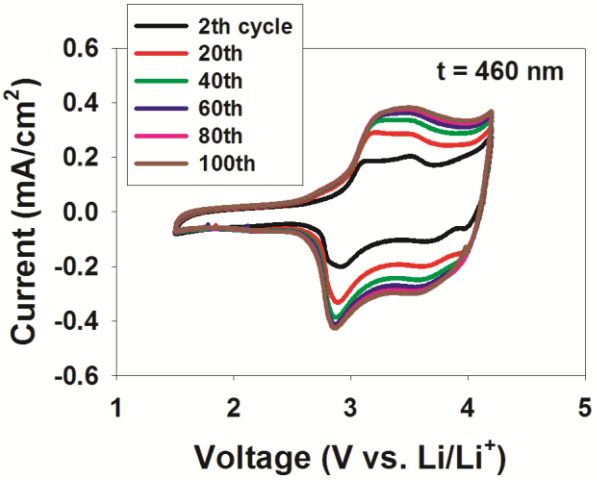

Figure 4.9. Conditioning of a 460 nm thick (PANI-$NF_{2.5}$/$ERGO_{3.5}$) LbL electrode at 20 mV/s.

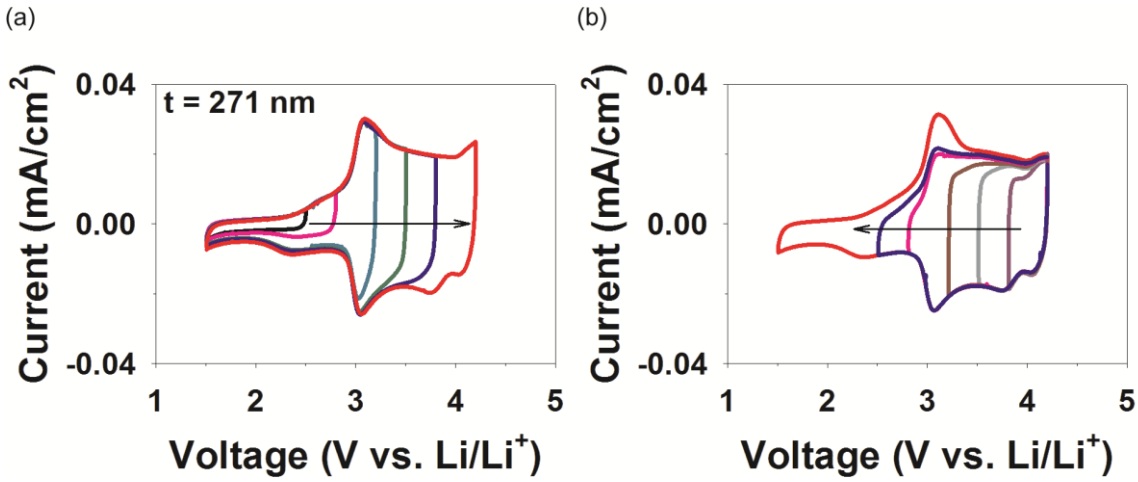

Figure 4.10. (a) Forward and (b) backward scans of cyclic voltammograms for a 271 nm thick (PANI-$NF_{2.5}$/$ERGO_{3.5}$) LbL electrode at 1 mV/s.

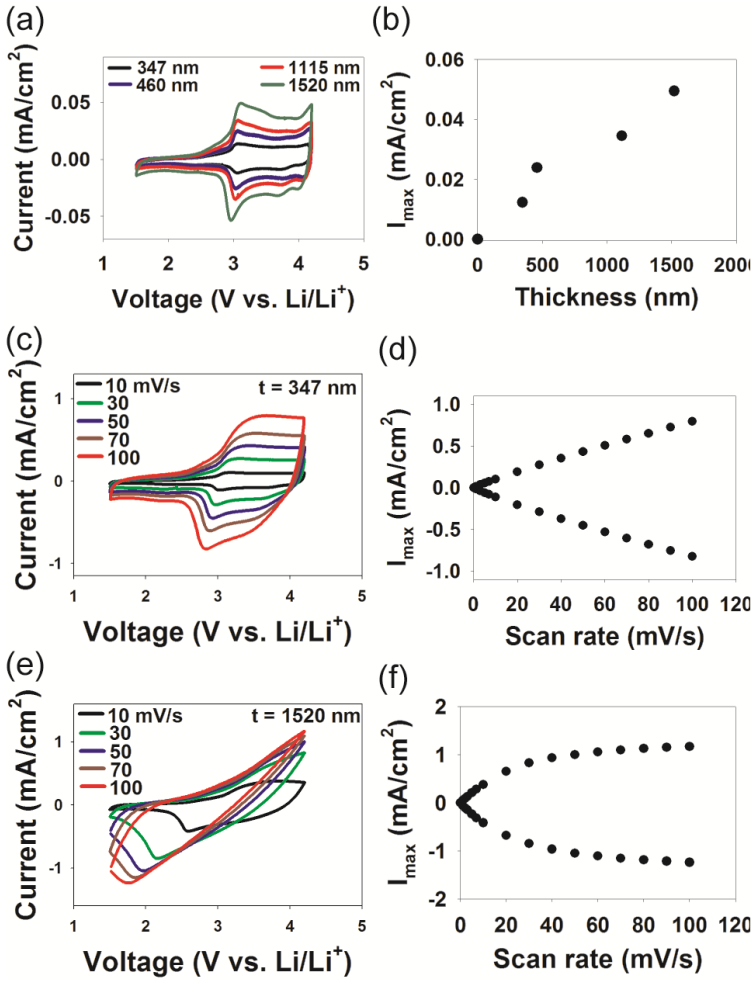

Figure 4.11. (a) Cyclic voltammograms of (PANI $NF_{2.5}$/$ERGO_{3.5}$) LbL electrodes of varying thicknesses at 1 mV/s. (b) Maximum current taken from voltammograms shown in panel (a) vs. electrode thickness. Cyclic voltammograms of (c) 347 nm and (e) 1520 nm thick (PANI $NF_{2.5}$/$ERGO_{3.5}$) LbL electrodes at various scan rates. Maximum current vs. scan rate for (d) 347 nm and (f) 1520 nm thick electrodes taken from the corresponding cyclic voltammograms.

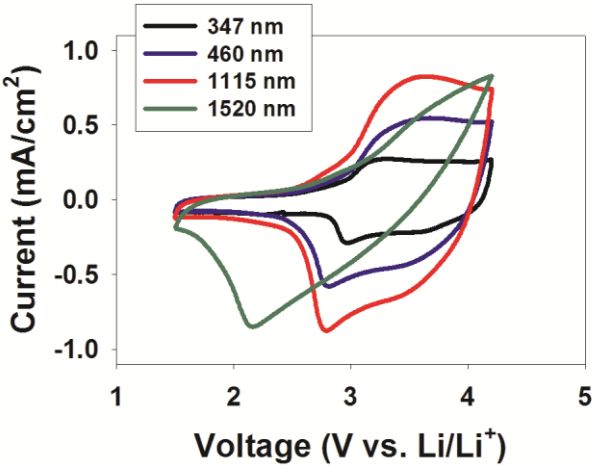

Figure 4.12. Cyclic voltammograms of (PANI-$NF_{2.5}$/$ERGO_{3.5}$) LbL electrodes having various thicknesses at a scan rate of 30 mV/s.

(one hundred cycles of cyclic voltammetry from 1.5 to 4.2 V at 20 mV/s); this process serves to accelerate the penetration of electrolyte into the electrode, Figure 4.9. Overlapping cyclic voltammagrams during forward and backwards sweeps was suggestive of the electrode"s reversibility, Figure 4.10. In cathodic scans, two prominent peaks were observed around 3 V and 3.8 V, which are attributed to pernigraniline/emeraldine and emeraldine/pernigraniline redox reactions.[52] It should be noted that ERGO provides electrical double layer capacitance as well as additional pseudocapacitance over a wide potential range originating from oxygen-containing functional groups even though no distinctive peak was observed.[63, 94, 95, 125]

In comparison to several other polyaniline-based LbL electrodes,[13, 52] the (PANI $NF_{2.5}$/$ERGO_{3.5}$) LbL electrodes exhibit greater electrochemical stability. PANI usually loses its electrochemical activity due to irreversible oxidation beyond 3.5 V (vs. Li/Li^+) in non-aqueous energy storage systems, as observed in PANI/polyacid, PANI/V_2O_5, and PANI NF/V_2O_5 LbL electrodes.[13, 52, 240] Here, (PANI $NF_{2.5}$/$ERGO_{3.5}$) LbL electrodes possessed reversible charge storage over a much wider voltage window (1.5 to 4.2 V vs. Li/Li^+). We suppose that the interaction between PANI NFs and ERGO sheets suppresses the irreversible degradation of PANI. Previously, we observed that strong interactions between PANI and a strong polyacid via template polymerization also induced electrochemical stability up to 4.5 V (vs. Li/Li^+).[52, 288] Elsewhere, PANI NF/MWNT LbL electrodes also could maintain reversible charge storage up to 4.5 V (vs. Li/Li^+) after heat treatment.[94] Here, we observed good reversibility for (PANI $NF_{2.5}$/$ERGO_{3.5}$) LbL electrodes without the need for a heat treatment.

(PANI $NF_{2.5}$/$ERGO_{3.5}$) LbL electrodes of varying thickness were subjected to cyclic voltammetry at 1 mV/s and 30 mV/s in three-electrode cells to assess relationships between charge storage and film thickness, (Figure 4.11a and Figure 4.12, respectively). At a scan rate of 1 mV/s, no significant peak shift was observed in anodic and cathodic peaks as electrode thickness increased, and current response nearly linearly increased with thickness at 1 mV/s, Figure 4.11b. On the contrary, at a scan rate of 30 mV/s, the two cathodic peaks substantially shifted and overlapped as electrode thickness increased, Figure 4.12. This result suggests that all of the electrode material is accessible and that

ion transport is not a limitation at a scan rate of 1 mV/s, but transport limitations arise at scan rates of 30 mV/s.

Cyclic voltammetry was also conducted on 347 and 1520 nm thick (PANI $NF_{2.5}$/$ERGO_{3.5}$) LbL electrodes at varying scan rates (Figure 4.11c and e, respectively). As scan rate increased from 10 to 100 mV/s, little distortion was observed for the 347 nm thick LbL electrode, and the cathodic peak only slightly shifted from 3 to 2.7 V. The maximum anodic and cathodic currents increased linearly with increasing scan rate, which is suggestive of a nondiffusion-controlled redox process, Figure 4.11d. In contrast, cyclic voltammograms of 1520 nm thick LbL electrode became distorted, in which the cathodic peak greatly shifted from 2.6 to 1.76 V; further, the maximum current increased nonlinearly with scan rate, Figure 4.7f. These results are consistent with hindered mass transport in thicker electrodes at high scan rates (100 mV/s). It should be noted that even if the electrode is thick, diffusion limitations can be overcome by charging and discharging at low C-rates.

To further investigate the separate contributions of diffusion-controlled and nondiffusion-controlled charge storage, an additional analysis was performed using following equation:

$$i = av^b \quad (4.1)$$

where ν is the scan rate, i is the current, and a and b are adjustable parameters.[240, 242] If b is 1, the redox process is an ideal nondiffusion-controlled reaction. If b is 0.5, the redox process is an ideal diffusion-controlled process. Intermediate values are indicative of mixed control. The b value was obtained from the slope of a plot of log i vs. log ν using

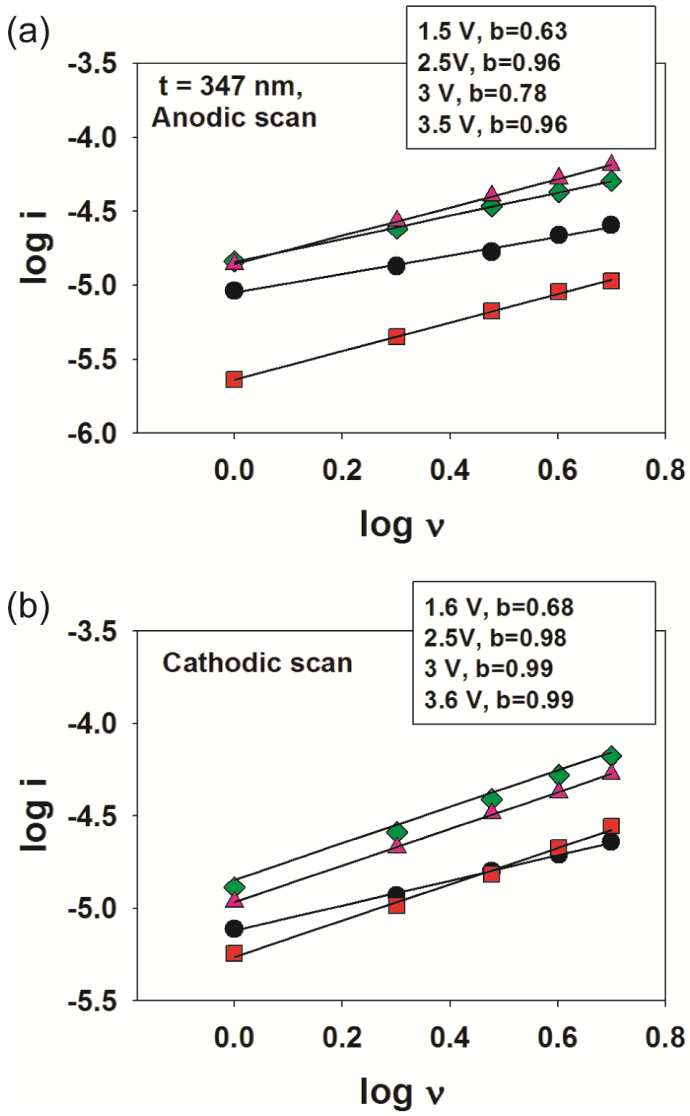

Figure 4.13. Graphs of log i vs. log ν for (a) anodic and (b) cathodic scans of the 347 nm thick (PANI-$NF_{2.5}$/$ERGO_{3.5}$) LbL electrodes used to obtain b values. The calculation was performed using cyclic voltammograms from 1 to 5 mV/s.

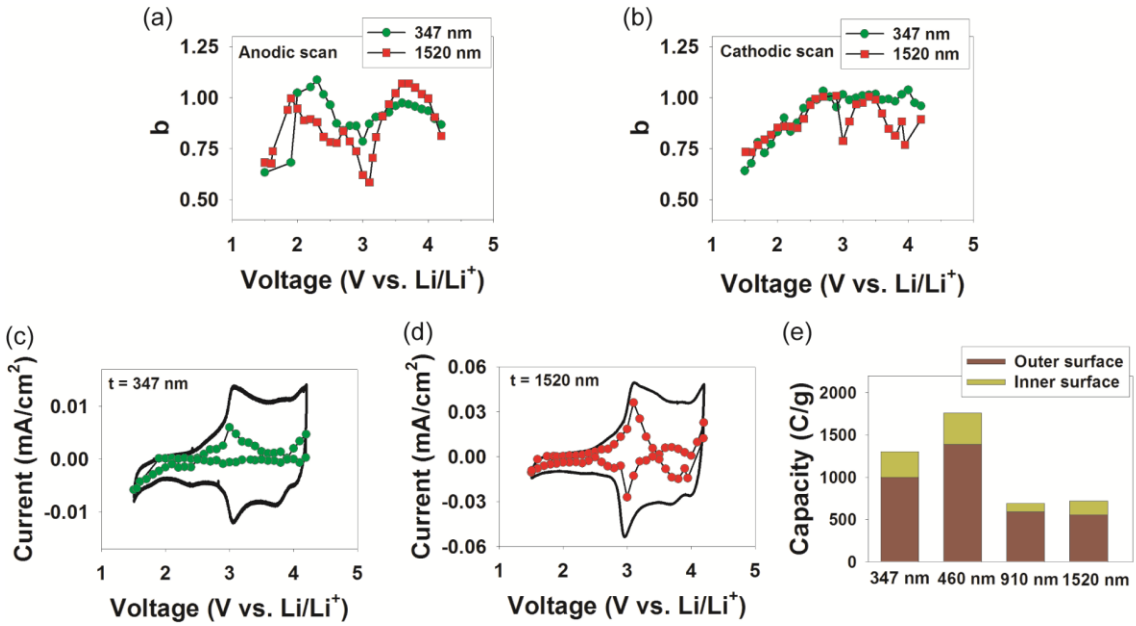

Figure 4.14. Calculated b values for (a) anodic and (b) cathodic scans of 347 nm and 1520 nm thick (PANI $NF_{2.5}$/$ERGO_{3.5}$) LbL electrodes vs. voltage. The diffusion-controlled contribution separated from cyclic voltammograms of (c) 347 nm and (d) 1520 nm thick (PANI $NF_{2.5}$/$ERGO_{3.5}$) LbL electrodes at 1 mV/s. The dotted line indicates the diffusion-controlled redox processes, and the solid line indicates the total current. (e) Inner and outer surface charge storage depending on the electrode thickness.

data from cyclic voltammograms in the range of 1 to 5 mV/s, Figure 4.13. The b values of 347 and 1520 nm thick (PANI $NF_{2.5}$/$ERGO_{3.5}$) LbL electrodes are shown for both anodic and cathodic scans (Figure 4.14a and b, respectively). Both thicknesses showed similar trends in b value. In anodic scans (Figure 4.14a), the b value increased towardsunity and then decreased as voltage increased from 1.5 to 3 V. Around 3 V, b

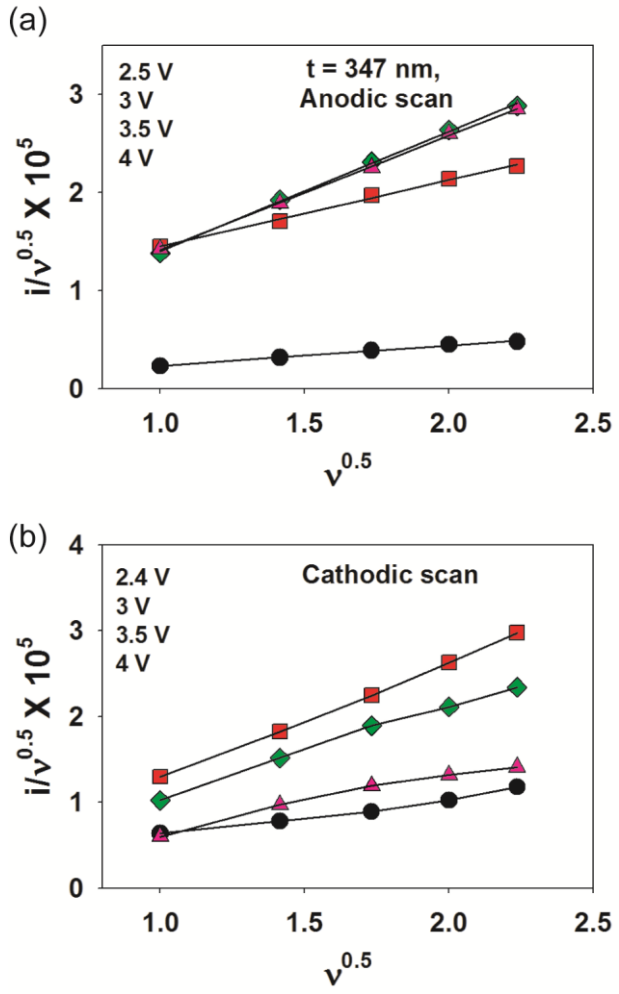

Figure 4.15. Graphs of log i/ $\nu^{0.5}$ vs. $\nu^{0.5}$ for (a) anodic and (b) cathodic scans of the 347 nm thick (PANI-$NF_{2.5}$/$ERGO_{3.5}$) LbL electrode to separate the diffusion-controlled redox processes. The calculation was performed using cyclic voltammograms from 1 to 5 mV/s.

reached minimum values of 0.78 and 0.58 for 347 and 1520 nm thick electrodes, respectively. Above 3 V, b values increased towards unity, which is similar to our previous results for PANI-containing electrodes.[240] In cathodic scans (Figure 4.14b), the trend in b value was more distinctive depending upon electrode thickness. The b value of the 347 nm thick electrode was near unity above 2.6 V. For the 1520 nm thick electrodes, the b valuewas between 0.75 and 1 in the range of 2.6 to 4.2 V, which is suggestive of mixed control upon reduction. These results, overall, are consistent with increased diffusion control in the charge storage process for thicker electrodes.

The relative contributions of nondiffusion-controlled and diffusion-controlled charge storage can be further visualized using the following analysis:

$$i(V) = a_1\nu + a_2\nu^{0.5} \quad (4.2)$$

The parameters a_1 and a_2 represent the relative contributions of nondiffusion-controlled and diffusion-controlled processes, respectively.[240, 242] From the slope and the intercept of plots of $i(V)/\nu^{0.5}$ vs. $\nu^{0.5}$ taken at a specific potential, the parameters a_1 and a_2 were obtained, Figure 4.15. From these parameters, a cyclic voltammogram such as that shown in Figure 4.14c-d was constructed. The solid line represents the combined current for electrodes at 1 mV/s, and the dotted line shows the current attributed to the diffusion-controlled process. The difference between the two yields the nondiffusion-controlled contribution. Upon comparison, the 1520 nm thick LbL electrode had a larger percentage of diffusion-controlled current as compared to the 347 nm thick electrode (31.4 vs. 22.5 %, respectively). This result is in accordance with the results drawn from b value analysis.

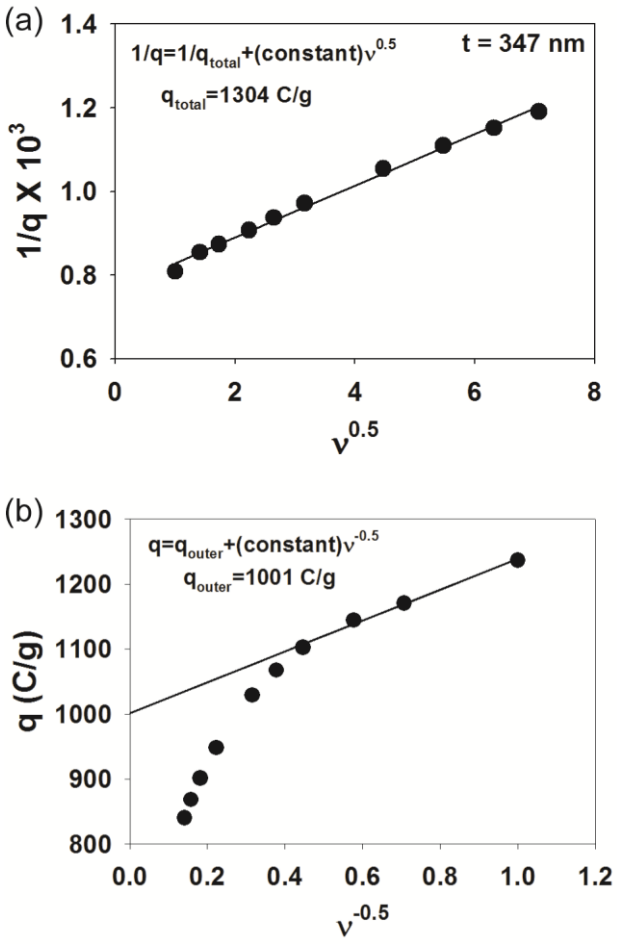

Figure 4.16. Graphs of (a) 1/q vs. $\nu^{0.5}$ for q_{total}, and (b) q vs. $\nu^{-0.5}$ for q_{outer}. The fit presented in panel (b) was executed for low scan rates, as suggested by Sathiya, *J. Am. Chem. Soc.* 2011, 133, 16291-16299

Presumably, nondiffusion control arises from some fraction of material that is not readily accessible. The following analysis allows for the separation of the total maximum charge (q_{total}) that can be stored into charge stored at the inner surface (q_{inner},

difficult to be utilized) and the outer surface (q_{outer}, easy to be utilized) by the following equation:[13, 242, 289]

$$q_{total} = q_{inner} + q_{outer} \quad (4.3)$$

The values of q_{total} and q_{outer} were calculated from the intercept of 1/q vs. $\nu^{0.5}$ and q vs. $\nu^{-0.5}$, respectively, for (PANI $NF_{2.5}$/$ERGO_{3.5}$) LbL electrodes, Figure 4.16. The percentage of charge stored at inner and outer surfaces was not distinctively dependent on electrode thickness (77 to 86 % from outer surfaces, 14 to 23 % from inner surfaces), Figure 4.14e. Instead, q_{total} was strongly influenced by film thickness. For example, the 460 nm thick electrode had a q_{total} of 1761 C/g, which consisted of 1390.5 C/g from outer surfaces (easily accessible) and 370.5 C/g from inner surfaces (not easily accessible). In the case of the 1520 nm thick electrode, the capacity of 721.4 C/g was achieved (557.4 C/g from outer surfaces, and 164 C/g from inner surfaces).

Galvanostatic charge-discharge measurements were performed with varying discharge currents on (PANI $NF_{2.5}$/$ERGO_{3.5}$) LbL electrodes to quantify their capacities and rate capabilities in a three-electrode cell. The charge-discharge profile was typically sloping, a characteristic often observed with conjugated polymers, Figure 4.17a. The capacity generally decreased with increasing discharge current for all thicknesses investigated, Figure 4.17b and Table 4.2. Also, the capacity increased with decreasing thickness, presumably because thinner electrodes are less susceptible to diffusion limitations. Of the electrodes investigated, the 460 nm thick (PANI $NF_{2.5}$/$ERGO_{3.5}$) LbL electrode possessed the highest capacity at 0.1 A/g (461 mAh/g and 184 mAh/cm^3) and maintained good capacity retention up to 10 A/g (368 mAh/g and 147 mAh/cm^3 or 80 %

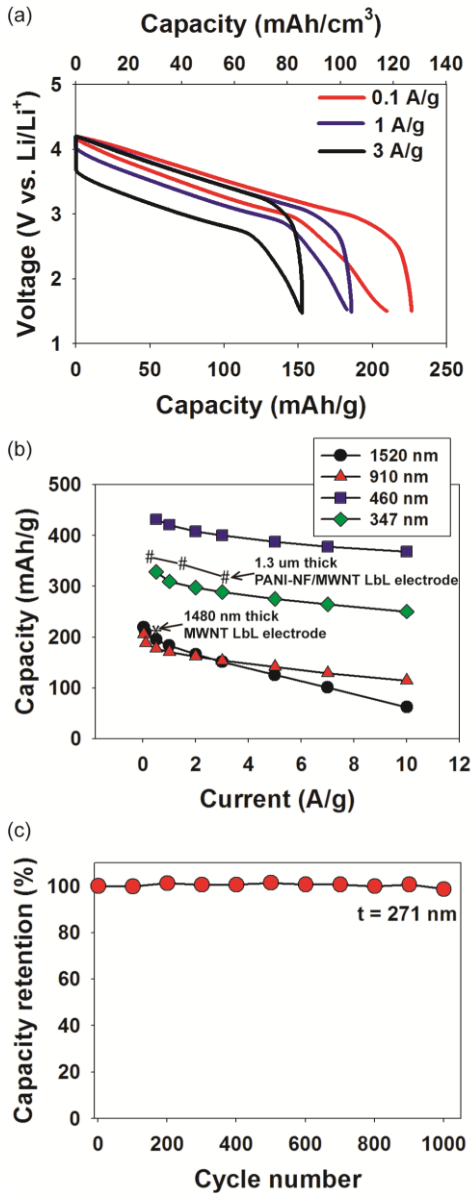

Figure 4.17. (a) Charge-discharge curves for a 1520 nm thick (PANI $NF_{2.5}$/$ERGO_{3.5}$) LbL electrode. (b) Capacity of (PANI $NF_{2.5}$/$ERGO_{3.5}$) LbL electrodes of varying thicknesses vs. discharge current. (c) Accelerated cycling behavior of a 271 nm thick (PANI $NF_{2.5}$/$ERGO_{3.5}$) LbL electrode at 35 A/g. Data in panel (b) are taken from ref.[63, 94] Capacity is based on the LbL mass and volume only.

Table 4.2. Capacity of PANI-NF/ERGO at a different current (mAh/g)

	0.03 A/g	0.05 A/g	0.1 A/g	0.5 A/g	1 A/g	2 A/g	3 A/g	5 A/g	7 A/g	10 A/g
371 nm				328	309	297	289	275	264	250
460 nm			461	432	421	408	400	387	378	368
910 nm	206	195	188	177	171	162	154	141	129	115
1520 nm	220	215	210	195	183	166	151	125	101	62

retention). These specific capacity values are higher than that of a 1.3 um thick PANI NF/MWNT LbL electrode.[94] For the 1520 nm thick LbL electrodes, the capacity decreased from 210 to 62 mAh/g (118 to 35 mAh/cm^3) when discharge current increased from 0.1 to 10 A/g (30% retention). This specific capacity is similar to that of MWNT LbL electrodes of comparable thickness reported by Hammond and Shao-Horn.[63] We attribute the high capacity of the (PANI $NF_{2.5}$/$ERGO_{3.5}$) LbL electrodes to the redox activity of PANI NFs and oxygen-containing functional groups on ERGO. The (PANI $NF_{2.5}$/$ERGO_{3.5}$) LbL electrode also exhibited excellent cycling behavior, Figure 4.17c. After 1000 cycles, 98.7% of the initial capacity was retained.

Galvanostatic charge-discharge measurements were also performed in two-electrode sandwich-type cells, Figure 4.18a. The capacity obtained from 1520 nm thick (PANI $NF_{2.5}$/$ERGO_{3.5}$) LbL electrodes was similar to that observed in the three-electrode configuration. For the sandwich-type cell, the capacity decreased from 199 to 49 mAh/g (112 to 27 mAh/cm^3) as discharge current increased from 0.1 to 10 A/g. After accelerated cycling at 10 A/g, the original capacity of 199 mAh/g was recovered when

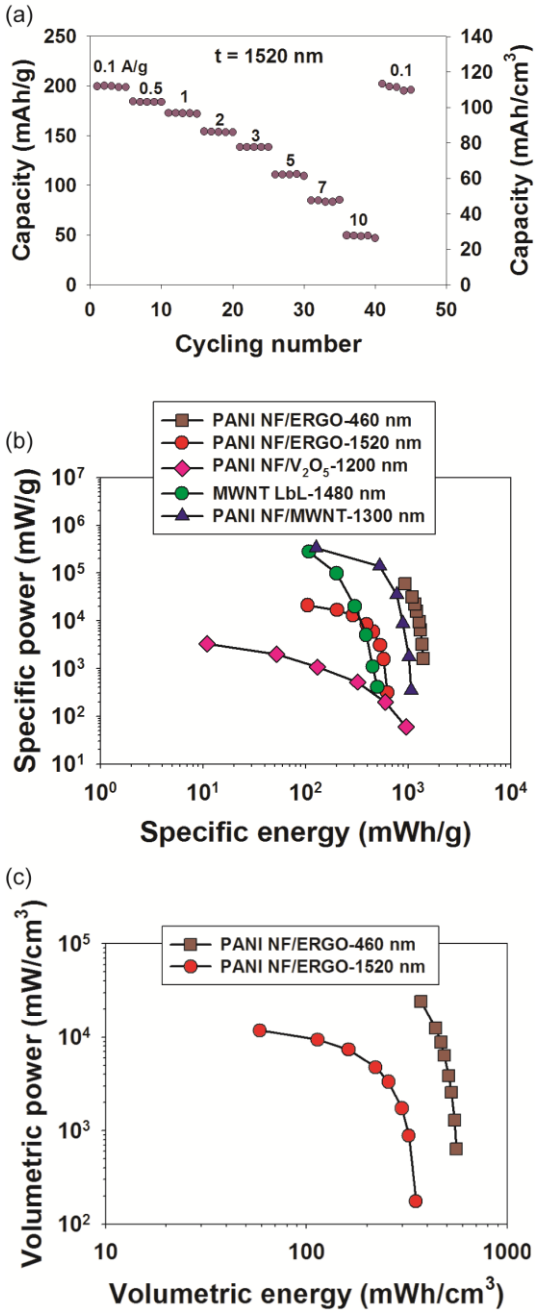

Figure 4.18. (a) Galvanostatic cycling of a 1520 nm thick (PANI $NF_{2.5}$/$ERGO_{3.5}$) LbL electrode in a two-electrode sandwich-type cell and Ragone plot based upon the LbL mass (b) and volume (c). Data in panel (b) were taken from references.[63, 94, 240]

0.1 A/g applied, which highlights the robustness and stability of the (PANI $NF_{2.5}$/$ERGO_{3.5}$) LbL electrodes. Specific energy and power for 460 and 1520 nm thick (PANI $NF_{2.5}$/$ERGO_{3.5}$) LbL electrodes are displayed in a Ragone plot along with other previously reported LbL electrodes, Figure 4.18b.[63, 94, 240] The 460 nm thick electrode possessed higher specific energy and power than the other LbL electrodes. Its maximum specific energy was 1395 mWh/g at a specific power of 1590 mW/g, and a maximum specific power of 60252 mW/g at a specific energy of 927mWh/g. In the case of the 1520 nm thick (PANI $NF_{2.5}$/$ERGO_{3.5}$) LbL electrode, at a given specific power of 313 mW/g, its specific energy was comparable to those of MWNT and PANI NF/V_2O_5 LbL electrodes. The specific power of 1520 nm thick (PANI $NF_{2.5}$/$ERGO_{3.5}$) LbL electrode was higher than that of PANI NF/V_2O_5 LbL electrodes, but lower than that of MWNT LbL electrodes at a given specific energy of 105 mWh/g. Energy and power density of PANI NF/ERGO electrodes were presented in Figure 4.18c. The 460 nm thick electrode had maximum energy density of 558 mWh/cm^3 at a power density of 636 mW/cm^3. The 1520 nm thick electrode showed maximum energy density of 351 mWh/cm^3 at a given power density of 176 mW/cm^3.

These results show that (PANI $NF_{2.5}$/$ERGO_{3.5}$) LbL electrodes are favorable as cathodes for thin film batteries. To improve the performance further, it will be necessary to enhance porosity so as to facilitate mass transport and allow for thicker films. As it will be shown in future work, spray-assisted LbL assembly promises to address this need. Spray-assisted LbL electrodes are under investigation in our lab.

4.4 CONCLUSIONS

The assembly of porous PANI NF/ERGO LbL electrodes was demonstrated herein. Assembly of GO sheets and subsequent electrochemical reduction circumvented the limited processability of CRGO sheets, which exhibited aggregation during LbL assembly. Electrochemical reduction of GO sheets further eliminates the necessity for harsh reducing agents otherwise required for the synthesis of CRGO. LbL assembly of GO sheets at acidic and at basic pH values with complementary PANI NFs was explored, in which acidic conditions were proven to yield the most robust growth (9.6 nm/layer pair). The resulting electrodes exhibited a low density (0.56 g/cm^3), suggestive of a highly porous structure, and consisted of 77 wt% PANI NFs and 23 wt% GO sheets. Subsequent electrochemical reduction yielded ERGO sheets with increased sp^2 graphitic domains, confirmed via Raman and X-ray photoelectron spectroscopy. Electrochemical characterization confirmed the enhanced electrochemical activity brought about by electrochemical reduction. Overall the electrodes were reversible over a potential range of 1.5 to 4.2 V vs. Li/Li$^+$. The 460 nm thick (PANI $NF_{2.5}$/$ERGO_{3.5}$) LbL electrode had one of the highest specific energy and power values (~1395 mWh/g (558 mWh/cm^3) at 1590 mW/g (636 mW/cm^3) measured at 0.5 A/g) among previously reported LbL electrodes; further the capacity was exceptionally high (461 mAh/g (184 mAh/cm^3) at 0.1 A/g), originating from redox activity arising from PANI NFs and oxygen-containing functional groups on ERGO sheets, as well as electrical double layer capacitance. Thicker electrodes showed reduced electrochemical activity, presumably because of ion transport limitations. The 1520 nm thick (PANI $NF_{2.5}$/$ERGO_{3.5}$) LbL electrodes

exhibited a capacity of 220 mAh/g (123 mAh/cm^3) at 0.03 A/g. Upon accelerated cycling, (PANI $NF_{2.5}$/$ERGO_{3.5}$) LbL electrodes retained 98.7% of their initial capacity.

The ease of processing, high capacity, high specific energy and power, and the excellent capacity retention suggest that the (PANI $NF_{2.5}$/$ERGO_{3.5}$) LbL electrode is an excellent electrode candidate for energy storage, especially as compared to other LbL systems. Our future work will translate this system from dip-assisted LbL assembly to spray-assisted LbL assembly, which is suitable for the rapid build-up of these electrodes over large areas onto a variety of substrates.

CHAPTER V

IN SITU ONE-STEP SYNTHESIS OF HIERARCHICAL NITROGEN-DOPED POROUS CARBON FOR HIGH-PERFORMANCE SUPERCAPACITOR*

5.1 INTRODUCTION

Undoped porous carbons have been commonly used as high surface area electrodes in supercapacitors because of their low cost, good processability, and high stability.[290] However, their electrochemical performance has been limited due to the fact that their charge storage mechanism solely depends on the adsorption of electrolyte ions onto the electrode surface.[291] In comparison, nitrogen-doped porous carbons have drawn great attention as electrode materials for energy storage because of their superior electrochemical properties.[292-295] Nitrogen dopants offer an additional mechanism of charge storage known as pseudo-capacitance, in which charge is stored through a rapid surface reaction.[296]

Nitrogen-doped carbons are generally synthesized using complex methods such as chemical vapor deposition (CVD), arc discharge, plasma treatment and thermal annealing with ammonia.[291, 297-299] In another approach, carbon precursors were processed with nitrogen-containing precursors (e.g., $CO(NH_2)_2$ and polypyrrole) to produce nitrogen-doped carbons.[293, 294, 300-302] In these methods, multiple steps were

* Reprinted with permission from "In situ one-step synthesis of hierarchical nitrogen-doped porous carbon for high-performance supercapacitors" by Ju-Won Jeon, Ronish Sharma, Praveen Meduri, Bruce W. Arey, Herbert T. Schaef, Jodie L. Lutkenhaus, John P. Lemmon, Praveen K. Thallapally, Manjula I. Nandasiri, Benard Peter McGrail, and Satish K. Nune, ACS Appl. Mater. Interfaces 2014, 6, 7214-7222, Copyright (2014) American Chemical Society

required to mix the carbon and nitrogen precursors and to form the finished product [298, 296, 300, 301].

One promising approach is to utilize precursors that contain both carbon and nitrogen,[303, 304 305] which reduces the number of steps associated with mixing. Nitrogen-doped carbon has been successfully synthesized using this approach, but there has been limited success in obtaining high surface area product; in one example the surface area was as low as 10 $m^2 g^{-1}$.[304, 305] To increase the surface area, precursor-loaded pore-forming templates were proposed.[306-308] Although promising, this approach required additional materials (the pore-forming template) and steps (acid treatment to remove the template).[306-308] Recently, the synthesis of nitrogen-doped porous carbons using ionic liquid-based precursors via direct carbonization was reported.[309-313] The ionic liquid could play the role of carbon source, nitrogen source, and sacrificial pore-forming template.[309-311] However, typical synthesis of the precursor ionic liquids requires multiple steps, and few have been explored as supercapacitor electrodes.[309, 314, 315]

Crystalline inorganic-organic hybrid materials composed of metal atoms and organic ligands (metal-organic frameworks, or MOFs) have attracted great attention in various applications including gas separations, catalysis, and energy storage due to the MOF‟s tunable porosity, functionality, and high surface area.[316] Recently, MOFs were used as templates for the synthesis of porous carbons in which the carbon-containing ligand provides the raw material for carbonization.[85, 86, 88, 89, 316-319] Importantly, the MOF itself acts as both the template as well as the carbon source, thus, reducing the number of steps required to produce and purify the resulting porous carbon. Conceivably, MOFs

bearing nitrogen and carbon-containing ligands could possess similar advantages in that they serve as the carbon source, the nitrogen source, and the template. Therefore, nitrogen-doped porous carbon obtained through the direct carbonization of MOFs is especially promising because it offers a simple approach free of additives and extraneous steps. In an early report, nitrogen-doped porous carbons were possibly fabricated by the carbonization of nitrogen-containing MOFs,[87] but their nitrogen content was not quantified nor discussed. Motivated by the recent interest in porous carbons for supercapacitors, an improvement in the production of high surface area nitrogen-doped porous carbons is urgently needed.

Herein, we demonstrate the synthesis of nitrogen-doped porous carbons through the direct carbonization of a nitrogen-containing isoreticular MOF (IRMOF-3). The approach detailed here does not require any additional nitrogen or carbon sources nor does it require an extraneous pore-forming template, because IRMOF-3 can act as precursors and self-sacrificial template. Furthermore, the nitrogen content and surface area are simply controlled by altering the carbonization temperature, which was not possible for many prior approaches.[291, 299] Both carbonized IRMOF-3 and MOF-5 are evaluated as supercapacitor electrodes. Carbonized MOF-5, which does not contain nitrogen, provides a convenient control to isolate the pseudocapacitance brought by nitrogen dopants in carbonized IRMOF-3, Figure 1. Our route is scalable in that multi-gram quantities of nitrogen-doped porous carbons are easily produced.

5.2 EXPERIMENTAL SECTION

MOF-5 and IRMOF-3 (isoreticular metal-organic framework-3) were synthesized through simple solvothermal methods reported elsewhere.[320] For the synthesis of MOF-5, zinc nitrate tetrahydrate (3.92 g, 15 mmol) and terephthalic acid (0.83 g, 5 mmol) were added into diethylformamide (150 mL) and sonicated until the solution turned clear. The resulting solution was transferred to an oven held at 105 °C for 24 h. After synthesis, the MOF-5 was washed with diethylformamide several times to remove unreacted precursors.

For IRMOF-3, zinc nitrate tetrahydrate (3.92 g, 15 mmol) and 2-aminobenzene-1, 4,-dicarboxylate (0.905 g, 5 mmol) were added to dimethylformamide (150 mL) and sonicated several minutes. The precursor solution was held at 100°C for 24 h, and then the product was washed with dimethylformamide several times. MOF-5 and IRMOF-3 were immersed in chloroform and stored.

The as-synthesized MOFs were placed in an alumina crucible and then transferred to a tube furnace to undergo carbonization. The furnace was purged with argon gas at room temperature for one hour. Then the temperature was increased at a rate of 5 °C/min up to 200 °C and maintained at 200 °C for five minutes to remove trace adsorbed contaminants. After five minutes, the temperature was increased at a rate of 1 °C/min to the target temperature (600, 700, 800, or 950 °C). Upon reaching the target temperature, the temperature was maintained an additional six hours. Then, the furnace was cooled to room temperature at a rate of 2.6 °C/min in the presence of argon. Throughout the procedure, the furnace was continually purged with argon gas. The flow

rate of argon gas was 12 ±2 sccm. The resulting carbon material was ground into a fine powder using a mortar and pestle. The material was then transferred to a scintillation vial for storage.

SEM images were obtained using an FEI Helios 600 NanoLab FIB-SEM (focused ion beam – scanning electron microscope). Nitrogen adsorption-desorption isotherms were collected using a Quantachrome autosorb-6 automated gas sorption. Brunauer-Emmett-Teller (BET) surface area was calculated from the nitrogen isotherm curves ranging from 0.1 to 0.3 of relative pressure. Pore size distribution was obtained using a density functional theory (DFT) model. This approach allowed for the measurement of pore diameters ranging from 0.4 to 5.5 nm. Pore diameters below 2 nm were attributed to micropores and those above 2 nm were mesopores. X-ray photoelectron spectroscopy (XPS) was performed using a Kratos Axis Ultra DLD spectrometer, which consisted of a high performance Al Kα monochromatic x-ray source (1486.7 eV) and a high-resolution spherical mirror analyzer with an energy resolution of 0.1 eV. The X-ray source was operated at 15 kV with an emission current of 10 mA. The charge neutralizer was used to exclude the surface charging effects and the binding energy of C 1s at 284.6 eV was used as the charge reference for binding energy calculations. The composition was determined based on the peak area of existing elements such as carbon, nitrogen and oxygen using Kratos software. The static contact angle of each electrode was measured using a using a Rame-Hart goniometer.

To obtain the electrochemical performance of MOFs-derived carbons, electrochemical measurements were carried out in two-electrode symmetric coin cells

with 1.0 M sulfuric acid as the aqueous electrolyte. First, the active material was mixed for 30 minutes with poly(vinylidene fluoride) (PVDF) and conductive carbon black (Super carbon 65, MTI) in N-methyl-2-pyrrolidone. The ratio of active materials to conductive carbon black to PVDF was 90: 5: 5 wt %. After mixing, the slurry was coated onto carbon paper using a brush and dried at 120 ℃ under vacuum. The prepared electrodes were cut and each electrode was weighed. Typically, the weight of a pair of electrodes was around 1.5 mg. The diameter of an electrode was 1.27 cm^2. The coin cell consisted of a top and bottom metal covering, spring, spacer, separator, two identical electrodes, and the electrolyte. Before measurements, the capacitor cells were soaked in electrolyte overnight so that the active material could be fully infiltrated by the electrolyte. The primary testing being performed was cyclic voltammetry at different scan rates ranging from 5 to 100 mV s^{-1}. Galvanostatic charge/discharge measurements were also carried out at different current rates from 0.5 A g^{-1} to 10 A g^{-1}.

For galvanostatic measurements, the specific capacitances were obtained by using the following equation[321]: $C = 4I\Delta t/(m\Delta V)$. In this equation, C is a specific capacitance (F g^{-1}), I is a current (A), Δt is discharge time (s), m is the mass of two electrodes (g), and ΔV is the voltage change during discharge. The capacitance was also calculated using cyclic voltammetry. For cyclic voltammetry, the specific capacitance was taken as $C = \frac{2}{m\nu\Delta V}\oint_{V_l}^{V_h} I(V)dV$.[322, 323] In this equation, V_h is the high-voltage cut-off, V_l is the low-voltage cut-off, and ν is the scan rate.

5.3. RESULTS AND DISCUSSION

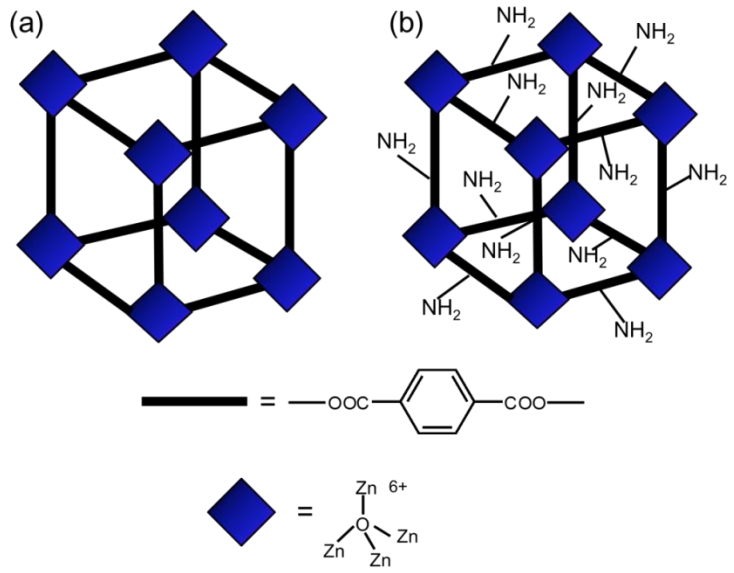

Figure 5.1. Schematic structure of (a) MOF-5 and (b) IRMOF-3. The structure and drawing concept were adapted from reference.[325]

MOFs (IRMOF-3: MOF containing Zn and 2-amino terephthalic acid; MOF-5: MOF containing Zn and terephthalic acid) were prepared using simple solvothermal approaches,[294, 324] in which MOF-5 was selected as a nitrogen-free control. The schematic structures of IRMOF-3 and MOF-5 are shown in Figure 5.1. Based on nitrogen adsorption-desorption measurements, the as-synthesized MOFs possessed high surface areas (MOF-5: 1305 $m^2 g^{-1}$ and IRMOF-3: 1221 $m^2 g^{-1}$); therefore, carbons

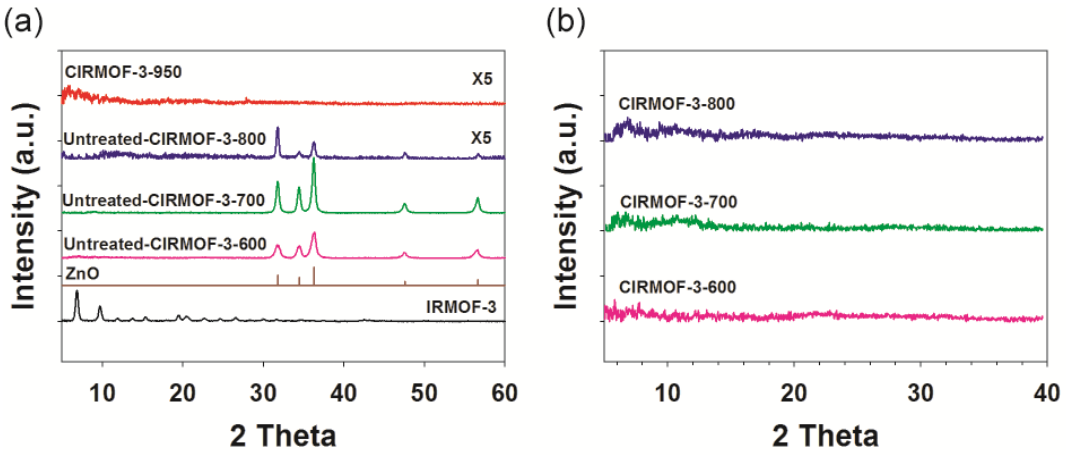

Figure 5.2. XRD patterns of (a) IRMOF, ZnO, Untreated-CIRMOF-3-600, 700, 800, and CIRMOF-950, (b) CIRMOF-3-600, 700, 800 after HCl etching

derived from these MOFs are expected to have high surface areas and significant differences in nitrogen doping.

To investigate the effect of carbonization temperature on nitrogen content, IRMOF-3 was carbonized at 600, 700, 800 or 950 ^{o}C resulting in carbonized-IRMOF-3, or CIRMOF-3s. For nomenclature, the carbonization temperature is referred to such that CIRMOF-3-950 indicates a carbonization temperature of 950 ^{o}C. MOF-5 was carbonized at 950 ^{o}C, resulting in CMOF-5-950. Carbonization of MOFs below 900 ^{o}C led to the formation of impurities such as zinc oxide (ZnO). After carbonization, peaks associated with the crystal structure of IRMOF-3 disappeared and peaks associated with ZnO appeared in XRD patterns (Figure 5.2a). For the CIRMOF-3 containing ZnO carbonized at 600, 700, and 800 ^{o}C, ZnO was removed by HCl etching, Figure5.2b. After HCl

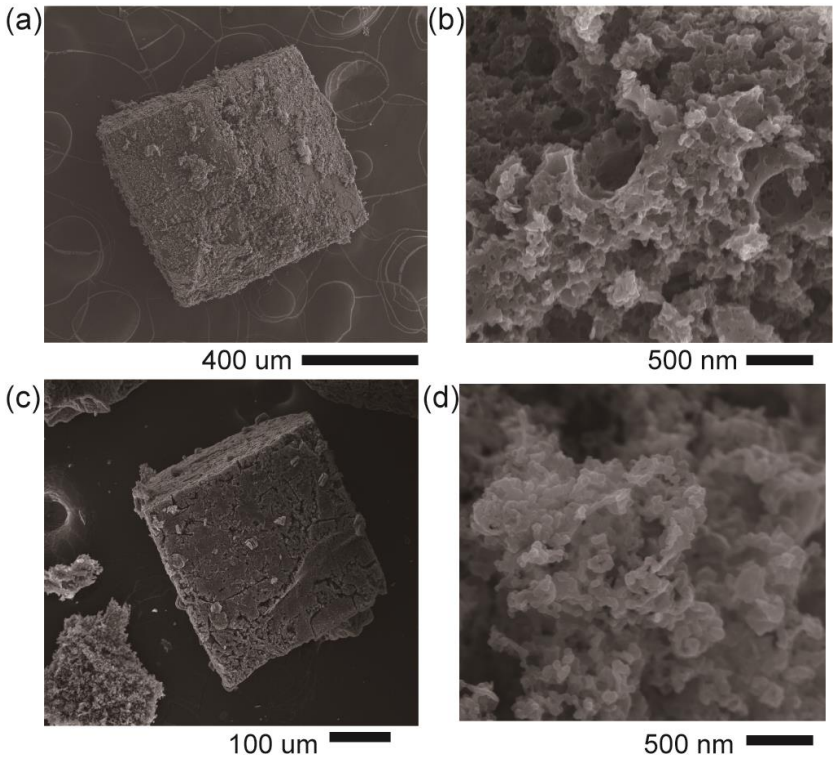

Figure 5.3. SEM images of (a), (b) CIRMOF-3-950 and (c), (d) CMOF-5-950.

etching, the surface area and porosity were greatly increased. This might be due to the fact that pores were generated while ZnO was etched away, possibly acting as an *in-situ* hard template. For carbonization of IRMOF-3 at 950 ^{o}C, peaks associated with ZnO disappeared confirming the sublimation of Zn-impurities resulting in pure carbon. The overall carbon yield of CIRMOF-3-950 was around 17 wt%.

SEM images clearly illustrate the hierarchical porous structure of CIRMOF-3 and CMOF-5, which have a cubic particle shape as well as a porous structure (Figure

Table 5.1. Physicochemical properties of porous carbons.

	S_{BET}[a] $m^2 g^{-1}$	Total pore volume[b] $cm^3 g^{-1}$	Micropore volume[b] $cm^3 g^{-1}$	Mesopore volume[b] $cm^3 g^{-1}$	C %	N %	O %	Contact angle °
IRMOF-3	1221	0.62	0.6	0.02				
CIRMOF-3-950	553	0.34	0.21	0.13	94.9	3.3	2.8	111
CIRMOF-3-800	402	0.24	0.16	0.08	86.1	3.3	10.6	87
CIRMOF-3-700	454	0.29	0.16	0.13	87.3	6	6.7	78
CIRMOF-3-600	391	0.23	0.15	0.08	85.4	7	7.6	22
Untreated-CIRMOF-3-800	124	0.08	0.04	0.04				
Untreated-CIRMOF-3-700	158	0.1	0.05	0.05				
Untreated-CIRMOF-3-600	319	0.2	0.12	0.08				
CMOF-5-950	572	0.33	0.24	0.09	98.1	-	1.9	138

[a]Brunauer-Emmett-Teller (BET) surface area
[b]Density functional theory (DFT)
-Micropore: pore size is less than 2 nm.
-Mesopore: pore size is larger than 2 nm and less than 50 nm. In this table, mesopore whose size is less than 5.5 nm is reported.

5.3). The rectangular shape is unique to the isoreticular metal-organic framework (IRMOFs), which was maintained during the carbonization process. In Figure 5.3b and d,it is clear that cubic CMOF particles are composed of interconnected small carbon particles with diameters less than 100 nm. To further characterize its porous nature, the Brunauer-Emmett-Teller (BET) surface area was determined using nitrogen adsorption-desorption measurements. The nitrogen sorption isotherms and pore size distributions of

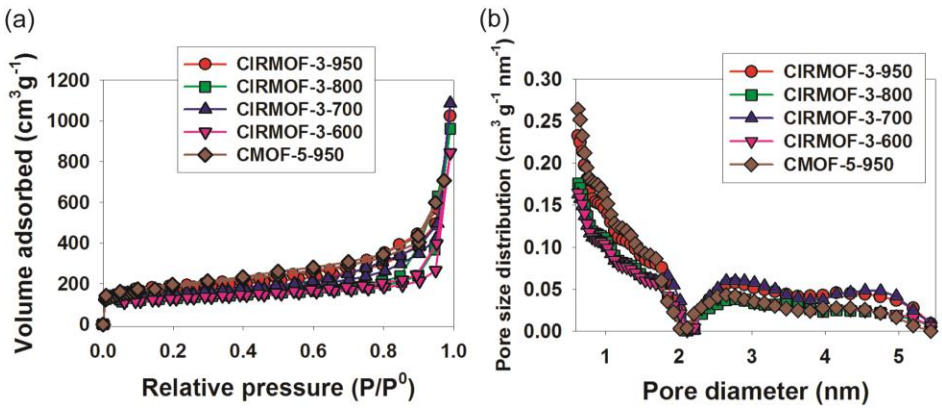

Figure 5.4. (a) Nitrogen adsorption-desorption isotherms, (b) pore size distribution calculated by density functional theory (DFT).

carbons derived from IRMOF-3 and MOF-5 are shown in Figure 5.4. CIRMOF-3-950 and CMOF-5-950 both exhibited type I and type II behavior based on the IUPAC classification.[326, 327] Both CIRMOF-3 and CMOF-5 showed large uptakes of nitrogen at low relative pressure ($P/P^0 < 0.1$), which was indicative of the presence of abundant micropores. This was followed by a plateau region and a steep increase of adsorbed nitrogen at high relative pressure ($P/P^0 > 0.9$), which probably originated from large meso- and macro pores due to interstitial voids between particles.[326, 328]

The pore size distribution was obtained from nitrogen isotherms using density functional theory (DFT).[317, 329] The pore size distribution analysis reveals the presence of micropores (< 2 nm) and a good degree of mesoporosity (2-50 nm), Table 5.1. Both CIRMOF-3-950 and CMOF-950 possess similar total pore volumes (0.34 $cm^3\ g^{-1}$ and 0.33 $cm^3\ g^{-1}$) and surface areas (553 $m^2\ g^{-1}$ and 572 $m^2\ g^{-1}$), respectively. These

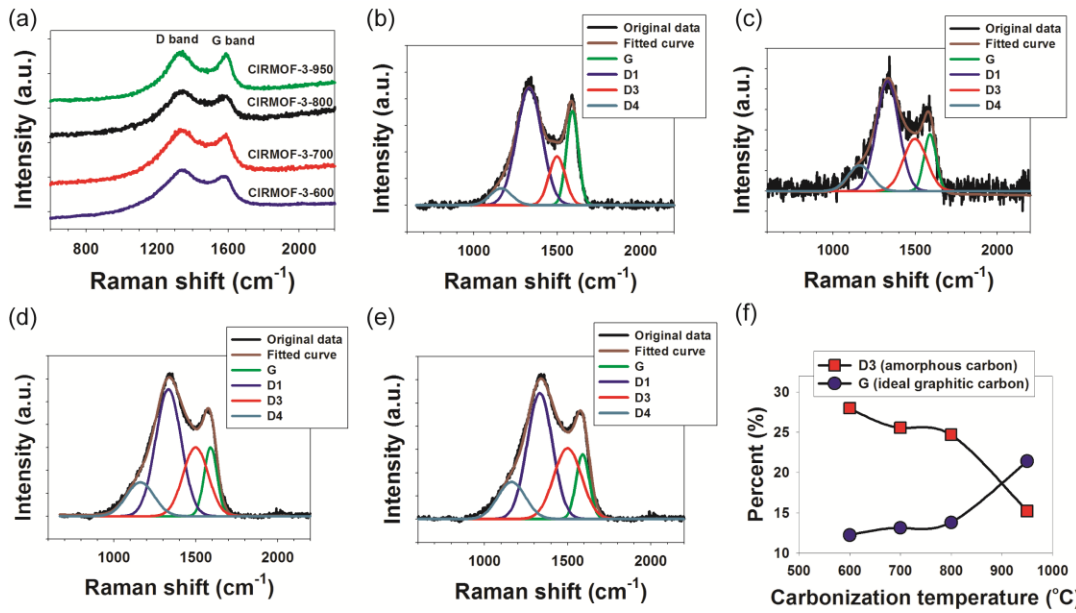

Figure 5.5. Raman spectra of (a) CIRMOF-3, (b) CIRMOF-3-950, (c) CIRMOF-3-800, (d) CIRMOF-3-700, (e) CIRMOF-3-600, and (f) amorphous and ideal graphitic carbon species versus carbonization temperature.

similarities arise from likenesses between the topology and precursors for IRMOF-3 and MOF-5.[330] As for CIRMOF-3, the high carbonization temperature (950 °C) led to highest micro-, meso-, and total pore volume relative to other carbonization temperatures, as well as the highest surface are. It is possible that Zn sublimation and ligand decomposition during carbonization at 950 ^{o}C contributed to the resulting porous structure.[331, 332] At low carbonization temperatures, the carbon network may not be fully developed, resulting in a lower surface area and porosity. As the carbonization

temperature increases, primary carbon particles likely form interconnected hierarchical structures as shown in Figure 5.3b and d.[317]

Raman spectroscopy was used to investigate the nature of carbon within CIRMOF-3. Two distinctive peaks were observed at 1335 and 1590 cm^{-1}, which correspond to D and G bands, respectively (Figure 5.5a). The G band indicates ideal graphitic sp^2 carbons, and the D band corresponds to disordered carbons.[276] The average ratios of G to D band intensities (I_G/I_D) for CIRMOF-3-950, CIRMOF-3-800, CIRMOF-3-700, and CIRMOF-3-600 were 0.98, 0.93, 0.94, and 0.89, respectively. CIRMOF-3-950 had the highest I_G/I_D ratio while CIRMOF-3-600 had the lowest I_G/I_D ratio, suggesting that higher carbonization temperatures contributes to the formation of graphitic sp^2 carbons

To more deeply investigate the structural properties of the porous carbons, the Raman spectra were deconvoluted into four different peaks centered at 1590, 1163, 1332, 1499 cm^{-1}, corresponding to G, D1, D3, and D4 bands, respectively, (Figure5.5b-e). D1 and D4 bands indicate disordered graphitic carbon, whereas the D3 band represents amorphous carbon.[333, 334] The percentage of amorphous carbon and ideal graphitic sp^2 carbon species versus carbonization temperature are shown in Figure 5f. The percentage of amorphous and ideal graphitic sp^2 carbon was greatly affected by carbonization temperature, in which the percentages of amorphous and ideal graphitic sp^2 carbon species decreased and increased, respectively, with increasing carbonization temperature. We speculate that the abrupt increase in degree of graphitization at 950 $^{\circ}C$ is related to Zn sublimation during the carbonization process. For CIRMOF-3-950, during the

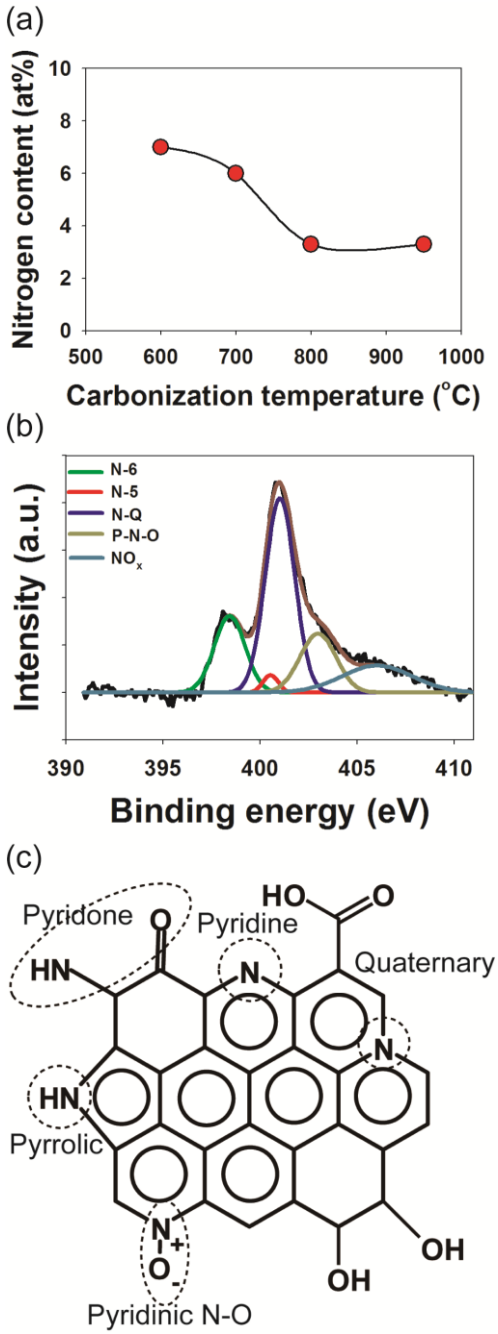

Figure 5.6. (a) Nitrogen content in CIRMOF-3 with respect to carbonization temperature and (b) the nitrogen region for CIRMOF-3-950 from XPS spectra. (c) Schematic illustration of nitrogen-doped carbon and various nitrogen functionalities identified by XPS.

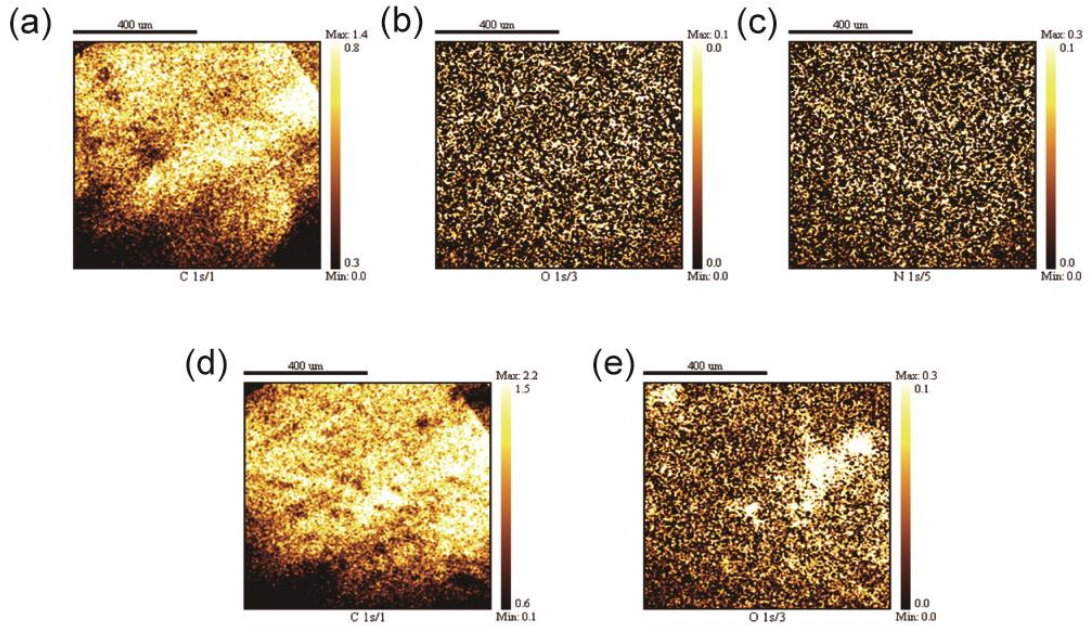

Figure 5.7. X-ray photoelectron spectroscopy (XPS) elemental mapping of (a) carbon, (b) oxygen, and (c) nitrogen in CIRMOF-3-950 and (d) carbon and (e) oxygen in CMOF-5-950.

carbonization, Zn sublimation occurs, which could provide carbons with more degree of freedom for graphitization. For CIRMOF-3-600,700, and 800, during carbonization, Zn exists as an oxide form (ZnO), which could lead to hamper overall graphitization process. The results clearly show that higher carbonization temperatures result in a higher percentage of graphitic carbon.[307, 335, 336]

X-ray photoelectron spectroscopy (XPS) analysis was performed to further quantify the extent of nitrogen doping (Figure 5.6, Table 5.1). As carbonization

temperature increased from 600 to 950 ^{o}C, the nitrogen content decreased from 7 to 3.3 atomic % for CIRMOF-3, in which nitrogen stems from the decomposition of the 2-aminoterephthalic acid ligand. In comparison, CMOF-5-950 bears no detectable levels of nitrogen, which is not surprising considering it does not contain nitrogen-based ligands. Since the bond energies of C-C and C-N bonds are 370 kJ mol^{-1} and 305 kJ,mol^{-1}, respectively, it is highly likely that the C-N bond is more susceptible to cleavage,[337] thus explaining the observed trends with respect to nitrogen content and carbonization temperature. It should also be noted that both MOFs contain oxygen, arising from decomposition of the oxygen-containing ligands.

XPS elemental mapping revealed that nitrogen and oxygen in CIRMOF-3-950 and oxygen in CMOF-5-950 were evenly distributed throughout the porous architecture (Figure 5.7). To further characterize the nature of nitrogen in the porous carbons, the N 1s peak of CIRMOF-3-950 was deconvoluted into five different peaks located at 398.4, 400.5, 401, 403, and 406 eV, which were assigned to pyridinic nitrogen (N-6), pyrrolic nitrogen or pyrridone (N-5), quaternary nitrogen (N-Q), pyridine-N-oxide (P-N-O), and chemisorbed NO_x, respectively (Figure 5.6b and c).[296, 338-340] Nitrogen in CIRMOF-3-950 was composed of 19.1 % of N-6, 2.2 % of N-5, 46.2 % of N-Q, 17.2 % of P-N-O, and 15.3 % of NO_x. N-Q was the dominant form of nitrogen in CIRMOF-3-950 while the content of N-5 was low. Pyrrolic nitrogen (N-5) has been reported to be less thermally stable than other forms of nitrogen, whereas quaternary nitrogen (N-Q) could be generated from other forms of nitrogen such as pyridinic nitrogen (N-6).[338] Hence, the dominance of N-Q is quite reasonable.

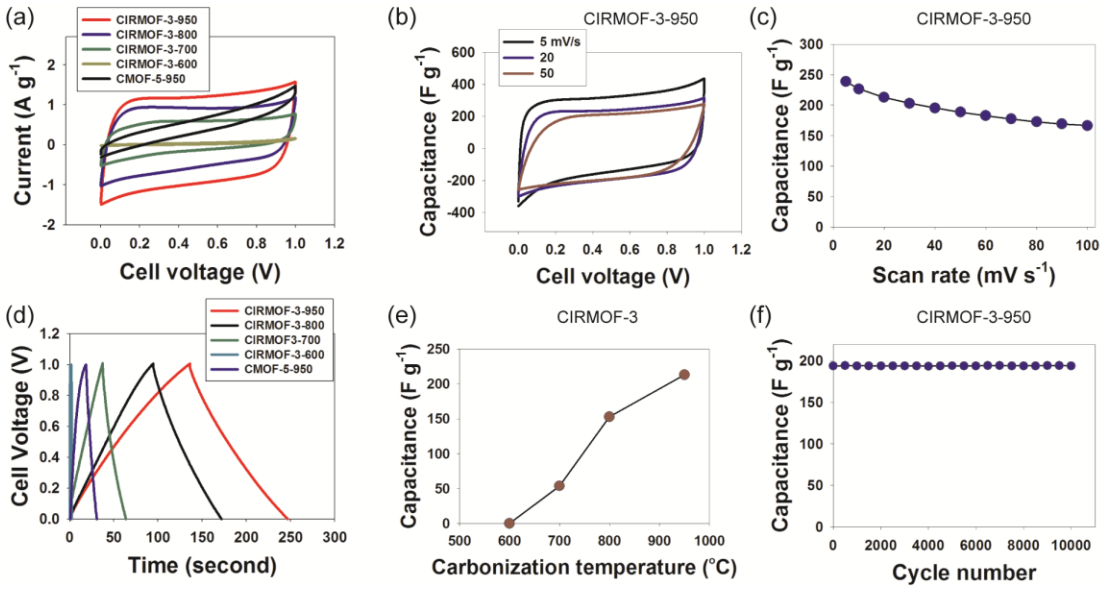

Figure 5.8. (a) Cyclic voltammograms (CVs) of CMOFs at 20 mV s^{-1}, (b) CVs of CIRMOF-3-950 at different scan rates, (c) specific capacitance of CIRMOF-3-950 vs. scan rate, (d) galvanostatic charge/discharge of CMOFs at 0.5 A g^{-1}, (e) capacitance of CIRMOF-3 vs. carbonization temperature, and (f) cycling of CIRMOF-3-950 at 50 mV s^{-1}.

Contact angle measurements were also carried out on CMOF electrodes to assess the wettability of aqueous electrolytes (Table 5.1). The contact angle of CIRMOF-3-950 was much smaller than that of CMOF-5-950 (111 vs. 138°, respectively), clearly indicating that nitrogen doping increases the electrode‟s wettability. Besides nitrogen, oxygen-containing functional groups can also contribute to a surface‟s properties. For

.

Table 5.2. Capacitance of symmetric coin cells with 1 M sulfuric acid electrolyte and at different current density (F g^{-1}).

	0.5A g^{-1}	1 A g^{-1}	2 A g^{-1}	5 A g^{-1}	10 A g^{-1}
CIRMOF-3-950	213	213	194	186	162
CIRMOF-3-800	153	146	136	103	81
CIRMOF-3-700	54	54	46	36	22
CIRMOF-3-600	0.6	0.3	0.6	0.6	0.9
CMOF-5-950	24	22	19	17	21

CIRMOFs, as carbonization temperature increased, the oxygen content first increased and then decreased. It should be noted that the contact angle was lowest for CIRMOF-3-600, which possessed the highest combined oxygen and nitrogen content, and lowest for CIRMOF-3-950, which possessed the lowest combined oxygen and nitrogen content.

To investigate the electrochemical performance of nitrogen-doped CMOFs as supercapacitors, electrodes were prepared using MOF-derived porous carbons. Symmetric coin cells were assembled using 1M sulfuric acid as the electrolyteElectrochemical performance was assessed using cyclic voltammetry and galvanostatic charge/discharge measurements. Figure 5.8a illustrates typical CVs of CMOFs at 20 mV s^{-1}. The cyclic voltammograms for CIRMOF-3 exhibited a nearly rectangular shape, which is typical behavior for supercapacitors[341, 342] for all carbonization temperatures. The CIRMOF-3-950 electrode showed the highest specific capacitance as compared to all other porous carbons investigated even though it had the

lowest nitrogen content; presumably this result arises from both CIRMOF-3-950‟s higher percentage of graphitic carbons as well as its high specific surface area and pore volume.[341] On the other hand, CMOF-5-950 showed distorted CV curves, which might be due to poor electrolyte wettability.[343, 344]

The specific capacitance of CIRMOF-3-950 was calculated from the cyclic voltammograms at various scan rates (Figure 5.8b and c), wherein an excellent specific capacitance of up to 239 F g^{-1} at 5 mV s^{-1} was obtained. Also, the specific capacitance of CIRMOF-3-950 was 189 and 166 F g^{-1} at scan rates 50 and 100 mV s^{-1}, respectively. The good rate capability of CIRMOF-3-950 was attributed to the hierarchical structure, which facilitates electrolyte migration through electrodes.[307]

Galvanostatic charge/discharge measurements were carried out on various CMOFs (Figure 5.8d and e). Capacitances of 213, 153, 54, 0.3, and 24 F g^{-1} were obtained for CIRMOF-3-950, CIRMOF-3-800, CIRMOF-3-700, CIRMOF-3-600, and CMOF-5-950 at 0.5 A g^{-1}, respectively, Table 5.2. Compared to other porous carbons, these values are higher than that of polymerized ionic liquids and lower than that of a nitrogen doped carbon obtained using acetronitrile precursor and zeolite templates.[311, 345] It is noteworthy that the specific capacitance of CMOF-5-950 was only 24 F g^{-1} even though it possessed the highest specific surface area of all CMOFs. The observed electrochemical performance clearly reveals the important role of nitrogen in enhancing electrolyte-electrode interactions and contributing additional pseudocapacitance.[291, 346, 347]

It should be noted that the capacitance of CIRMOF-3-800 is lower than that of CIRMOF-3-950 even though they possess the same nitrogen content. However, CIRMOF-3-950 possesses a higher percentage of graphitic carbon, which leads to a higher capacitance. Even though CIRMOF-3-800 possesses more oxygen-containing functional groups, which can also potentially contribute to the capacitance,[63, 94] far less charge was stored in comparison. This finding suggests that the capacitance depends more on the extent of carbonization than on the oxygen content.

Long-term cycling of CIRMOF-3-950 showed no obvious fade in capacitance even after 10,000 cycles (Figure 5.8f). Its excellent stability indicates that no major changes in physical or chemical structure occur during the cycling process. Further, the high capacitance and stability of CIRMOF-3-950 suggest its potential in other applications such as oxygen reduction, which we are current exploring.

5.4. CONCLUSIONS

In summary, nitrogen-doped porous carbons were synthesized from MOFs using a self-templating approach without any additional carbon or nitrogen sources. A one-step synthetic route was presented in which no additional purification steps, such as acid washing, were required. In this study, nitrogen content and surface area were easily controlled simply by changing carbonization temperature. Of all the MOFs examined, CIRMOF-3-950 possessed the highest capacitance (239 F g^{-1}) due to an enhanced electrolyte-electrode interaction, fewer carbon defects, and additional pseudocapacitance

from nitrogen dopants. These materials present a straightforward approach to produce porous carbon electrodes, and open new avenues for other applications.

CHAPTER VI

CONCLUSIONS AND PERSPECTIVE

In this thesis, several electrode materials including polyaniline (PANI), graphene, nitrogen-doped porous carbon were synthesized and characterized for energy storage applications. For the polyaniline-based electrodes, the oxidative stability was successfully enhanced via template polymerization and secondary interactions. The origin of this increase in oxidative stability was studied using experiments as well as simulation. In situ one-step synthesis of nitrogen-doped porous carbon was also presented through direct carbonization of nitrogen-containing metal-organic frameworks.

In chapter 2, template polymerized polyaniline:polyacid complex was demonstrated as an electrode for energy storage. Polyaniline:poly(2-acrylamido-2-methyl-1-propanesulfonic acid) (PANI:PAAMPSA, containing 25wt% PANI) was successfully synthesized using template polymerization. Due to the excess sulfonic acid groups, PANI:PAAMPSA was negatively charged. PANI:PAAMPSA complex showed a reversible capacity of 230 mAh/g of PANI under a wide voltage range (from 1.5 to 4.5 V vs. Li/Li^+). More importantly, PANI:PAAMPSA complex showed significantly enhanced oxidative stability up to 4.5 V vs. Li/Li^+. PANI:PAAMPSA retained 88.5 % of its original capacity while PANI homopolymer only retained 5.5 %. Electrostatic and hydrogen bonding interactions between PANI and PAAMPSA were able to stabilize the pernigraniline salt form of polyaniline, which is normally highly unstable. As a consequence, by using PANI:PAAMPSA electrodes, we could utilize not only the

reaction between leucoemeraldine base and emeraldine salt, but also the reaction between emeraldine salt and pernigraniline salt by altering the reaction pathway.

In chapter 3, PANI/PAAMPSA, PANI/PANI:PAAMPSA, and linear poly(ethylenimine)/PANI:PAAMPSA (LPEI/PANI:PAAMPSA) electrodes were fabricated using a layer-by-layer (LbL) technique. PANI/PAAMPSA and PANI/PANI:PAAMPSA were composed of nearly 1:1 of polycations and polyanioins (by weight), while LPEI/PANI:PAAMPSA consisted of 8 wt% of LPEI and 92 wt% PANI:PAAMPSA. After LbL assembly, PANI existed in the emeraldine salt form in all LbL films. PANI/PAAMPSA and PANI/PANI:PAAMPSA possessed high initial capacities of ~100 mAh/g of PANI. However, a gradual decrease in capacity was observed for PANI/PAAMPSA and PANI/PANI:PAAMPSA during cycling due to the irreversible oxidation of PANI to pernigraniline base. Even though LPEI/PANI:PAAMPSA had capacity of 26 mAh/g of PANI, it could retain its oxidative stability up to 4.5 V (vs. Li/Li^+) and showed little capacity fade.

In chapter 4, porous polyanline nanofiber/reduced graphene oxide (PANI NF/RGO) hybrid electrodes were fabricated via electrochemical reduction of layer-by-layer (LbL) assembled PANI NF/graphene oxide (GO) films. By using GO for LbL assembly, the limited processability of RGO could be overcome. Growth profiles of PANI NF/GO LbL films can be easily altered by varying the pH of the GO dispersion. PANI NF/GO LbL films were also deposited onto cotton fabric. Porous PANI NF/ERGO LbL electrodes possessed exceptionally high capacity varying from 188 to 461 mAh/g (85 to 184 mAh/cm^3) at 0.1 A/g (from 1.5 to 4.2 V vs. Li/Li^+), depending on

the electrode thickness. This high capacity originated from the redox properties of PANI-NF and oxygen-containing functional groups associated with ERGO as well as electrical double layer capacitance. The effect of electrode thickness on charge storage was thoroughly studied using cyclic voltammetry, indicating that thicker electrodes are more susceptible to diffusion limitation at high current. Interestingly, PANI NF/ERGO LbL electrodes showed great reversibility and cycling stability up to 4.2 V vs. Li/Li^+. Even after 1000 cycles, no significant decrease in capacity was observed.

In chapter 5, hierarchical nitrogen-doped porous carbon was synthesized by one-step carbonization of nitrogen-containing metal-organic framework (IRMOF-3). IRMOF-3 acted as carbon and nitrogen precursors as well as self-sacrificial templates. The nitrogen content in the porous carbon was easily controlled by altering carbonization temperature. High carbonization temperature resulted in more graphitized and less defective porous carbons, leading to higher electrochemical performance. Nitrogen-doped porous carbon derived from IRMOF-3 through carbonization at 950 ^oC possessed capacitance of 239 F/g, which was significantly higher than that of an analogous nitrogen-free porous carbon.

In this thesis, traditional dip-assisted LbL assembly was used to fabricate several PANI-based LbL electrodes. Even though traditional dip-assisted LbL assembly is simple and inexpensive, it is difficult to be used for industrial applications because of its long processing time (~48 minutes a layer pair). Therefore, in the future, alternative methods should be proposed to reduce processing time while maintaining its advantageous properties. Spray-assisted LbL assembly is a good candidate because it

could reduce the processing time dramatically so that it would be more practical to fabricate thick LbL electrodes. For example, in the case of spray PANI NF/GO LbL films, it takes only ~140 seconds per layer pair, which is significantly faster than traditional dip-assisted LbL assembly (~48 minutes a layer pair).[348] Future work will focus on fabricating hybrid electrodes using spray-assisted LbL assembly in place of traditional dip-assisted LbL assembly. Various combinations of electrochemically active materials could be used to fabricate hybrid LbL electrodes including graphene, vanadium pentoxide, and polyaniline using this technique.

In chapter 5, nitrogen-containing MOF (IRMOF-3) was used as a precursor to synthesize nitrogen-doped porous carbons. In the future, other nitrogen-containing MOFs can be directly carbonized for nitrogen-doped porous carbons. For example, zeolitic imidazolate framework (ZIF-8), which contains carbon and nitrogen in its ligand, could be used to synthesize nitrogen-doped porous carbons. Because the nitrogen content and structure of ZIF-8 is quite different from IRMOF-3, the resulting porous carbons are expected to possess different nitrogen content and porous structures. It is also expected that nitrogen content can still be controlled by changing the carbonization temperature of ZIF-8. Even though nitrogen-doped porous carbons can be synthesized from MOFs, the precursors, MOFs are relatively expensive. By using other inexpensive precursors, the cost of porous carbons can be lowered. For example, lignin, one of the most abundant natural polymers, can be used as a carbon precursor to produce porous carbons.

REFERENCES

1. Arico, A. S.; Bruce, P.; Scrosati, B.; Tarascon, J. M.; Van Schalkwijk, W. Nanostructured materials for advanced energy conversion and storage devices. *Nat. Mater.* 2005, 4, 366-377.

2. Wang, G. P.; Zhang, L.; Zhang, J. J. A review of electrode materials for electrochemical supercapacitors. *Chem. Soc. Rev.* 2012, 41, 797-828.

3. Simon, P.; Gogotsi, Y. Materials for electrochemical capacitors. *Nat. Mater.* 2008, 7, 845-854.

4. Wang, Q. S.; Ping, P.; Zhao, X. J.; Chu, G. Q.; Sun, J. H.; Chen, C. H. Thermal runaway caused fire and explosion of lithium ion battery. *J. Power Sources* 2012, 208, 210-224.

5. Vol'fkovich, Y. M.; Serdyuk, T. M. Electrochemical capacitors. *Russ. J. Electrochem.* 2002, 38, 935-958.

6. Winter, M.; Brodd, R. J. What are batteries, fuel cells, and supercapacitors? *Chem. Rev.* 2004, 104, 4245-4269.

7. Wang, Y. G.; He, P.; Zhou, H. S. Olivine LiFePO4: development and future. *Energy Environ. Sci.* 2011, 4, 805-817.

8. Liu, X. M.; Huang, Z. D.; Oh, S. W.; Zhang, B.; Ma, P. C.; Yuen, M. M. F.; Kim, J. K. Carbon nanotube (CNT)-based composites as electrode material for rechargeable Li-ion batteries: A review. *Compos. Sci. Technol.* 2012, 72, 121-144.

9. Kamali, A. R.; Fray, D. J. Review on carbon and silicon based materials asanode materials for lithium Ion batteries. *J. New Mat.Electrochem. Syst.* 2010, 13, 147-160.

10. Fu, L. J.; Liu, H.; Li, C.; Wu, Y. P.; Rahm, E.; Holze, R.; Wu, H. Q. Electrode materials for lithium secondary batteries prepared by sol-gel methods. *Prog. Mater. Sci.* 2005, 50, 881-928.

11. Yang, S. F.; Song, Y. N.; Zavalij, P. Y.; Whittingham, M. S. Reactivity, stability and electrochemical behavior of lithium iron phosphates. *Electrochem. Commun.* 2002, 4, 239-244.

12. Xiao, X. C.; Lu, P.; Ahn, D. Ultrathin multifunctional oxide coatings for lithium Ion batteries. *Adv. Mater.* 2011, 23, 3911-+.

13. Shao, L.; Jeon, J. W.; Lutkenhaus, J. L. Polyaniline/vanadium pentoxide layer-by-layer electrodes for energy storage. *Chem. Mat.* 2012, 24, 181-189.

14. Chan, C. K.; Peng, H. L.; Liu, G.; McIlwrath, K.; Zhang, X. F.; Huggins, R. A.; Cui, Y. High-performance lithium battery anodes using silicon nanowires. *Nat. Nanotechnol.* 2008, 3, 31-35.

15. Landi, B. J.; Ganter, M. J.; Cress, C. D.; DiLeo, R. A.; Raffaelle, R. P. Carbon nanotubes for lithium ion batteries. *Energy Environ. Sci.* 2009, 2, 638-654.

16. Tarascon, J. M.; Armand, M. Issues and challenges facing rechargeable lithium batteries. *Nature* 2001, 414, 359-367.

17. Zhamu, A.; Chen, G. R.; Liu, C. G.; Neff, D.; Fang, Q.; Yu, Z. N.; Xiong, W.; Wang, Y. B.; Wang, X. Q.; Jang, B. Z. Reviving rechargeable lithium metal batteries: enabling next-generation high-energy and high-power cells. *Energy Environ. Sci.* 2012, 5, 5701-5707.

18. Dhameja, S. Electric vehicle batteries. Butterworth-Heinemann, Woburn MA, 2002, ISBN 0-7506-9916-7.

19. Patil, A.; Patil, V.; Shin, D. W.; Choi, J. W.; Paik, D. S.; Yoon, S. J. Issue and challenges facing rechargeable thin film lithium batteries. *Mater. Res. Bull.* 2008, 43, 1913-1942.

20. Snook, G. A.; Kao, P.; Best, A. S. Conducting-polymer-based supercapacitor devices and electrodes. *J. Power Sources* 2011, 196, 1-12.

21. Nishino, A. Capacitors: operating principles, current market and technical trends. *J. Power Sources* 1996, 60, 137-147.

22. Zhai, Y. P.; Dou, Y. Q.; Zhao, D. Y.; Fulvio, P. F.; Mayes, R. T.; Dai, S. Carbon materials for chemical capacitive energy storage. *Adv. Mater.* 2011, 23, 4828-4850.

23. Jayalakshmi, M.; Balasubramanian, K. Simple capacitors to supercapacitors - an overview. *Int. J. Electrochem. Sci.* 2008, 3, 1196-1217.

24. Jeon, J. W.; Sharma, R.; Meduri, P.; Arey, B. W.; Schaef, H. T.; Lutkenhaus, J. L.; Lemmon, J. P.; Thallapally, P. K.; Nandasiri, M. I.; McGrail, B. P.; Nune, S. K. In situ one-step synthesis of hierarchical nitrogen-doped porous carbon for high-performance supercapacitors. *ACS Appl. Mater. Interfaces* 2014, 6, 7214-7222.

25. Pandolfo, A. G.; Hollenkamp, A. F. Carbon properties and their role in supercapacitors. *J. Power Sources* 2006, 157, 11-27.

26. Futaba, D. N.; Hata, K.; Yamada, T.; Hiraoka, T.; Hayamizu, Y.; Kakudate, Y.; Tanaike, O.; Hatori, H.; Yumura, M.; Iijima, S. Shape-engineerable and highly densely packed single-walled carbon nanotubes and their application as super-capacitor electrodes. *Nat. Mater.* 2006, 5, 987-994.

27. Choi, B. G.; Yang, M.; Hong, W. H.; Choi, J. W.; Huh, Y. S. 3D macroporous graphene frameworks for supercapacitors with high energy and power densities. *ACS Nano* 2012, 6, 4020-4028.

28. Zhu, Y. W.; Murali, S.; Stoller, M. D.; Ganesh, K. J.; Cai, W. W.; Ferreira, P. J.; Pirkle, A.; Wallace, R. M.; Cychosz, K. A.; Thommes, M.; Su, D.; Stach, E. A.; Ruoff, R. S. Carbon-based supercapacitors produced by activation of graphene. *Science* 2011, 332, 1537-1541.

29. Wu, N. L. Nanocrystalline oxide supercapacitors. *Mater. Chem. Phys.* 2002, 75, 6-11.

30. Liu, T. C.; Pell, W. G.; Conway, B. E. Self-discharge and potential recovery phenomena at thermally and electrochemically prepared RuO2 supercapacitor electrodes. *Electrochim. Acta* 1997, 42, 3541-3552.

31. Broughton, J. N.; Brett, M. J. Variations in MnO2 electrodeposition for electrochemical capacitors. *Electrochim. Acta* 2005, 50, 4814-4819.

32. Toupin, M.; Brousse, T.; Belanger, D. Charge storage mechanism of MnO_2 electrode used in aqueous electrochemical capacitor. *Chem. Mat.* 2004, 16, 3184-3190.

33. Wang, S. Y.; Ho, K. C.; Kuo, S. L.; Wu, N. L. Investigation on capacitance mechanisms of Fe3O4 electrochemical capacitors. *J. Electrochem. Soc.* 2006, 153, A75-A80.

34. Cheng, Q.; Tang, J.; Ma, J.; Zhang, H.; Shinya, N.; Qin, L. C. Polyaniline-coated electro-etched carbon fiber cloth electrodes for supercapacitors. *J. Phys. Chem. C* 2011, 115, 23584-23590.

35. Ryu, K. S.; Kim, K. M.; Park, N. G.; Park, Y. J.; Chang, S. H. Symmetric redox supercapacitor with conducting polyaniline electrodes. *J. Power Sources* 2002, 103, 305-309.

36. Belanger, D.; Ren, X. M.; Davey, J.; Uribe, F.; Gottesfeld, S. Characterization and long-term performance of polyaniline-based electrochemical capacitors. *J. Electrochem. Soc.* 2000, 147, 2923-2929.

37. Jurewicz, K.; Delpeux, S.; Bertagna, V.; Beguin, F.; Frackowiak, E. Supercapacitors from nanotubes/polypyrrole composites. *Chem. Phys. Lett.* 2001, 347, 36-40.

38. Liu, R.; Il Cho, S.; Lee, S. B. Poly(3,4-ethylenedioxythiophene) nanotubes as electrode materials for a high-powered supercapacitor. *Nanotechnology* 2008, 19.

39. Gallegos, A. K. C.; Rincon, M. E. Carbon nanofiber and PEDOT-PSS bilayer systems as electrodes for symmetric and asymmetric electrochemical capacitor cells. *J. Power Sources* 2006, 162, 743-747.

40. Hsieh, T. F.; Chuang, C. C.; Chen, W. J.; Huang, J. H.; Chen, W. T.; Shu, C. M. Hydrous ruthenium dioxide/multi-walled carbon-nanotube/titanium electrodes for supercapacitors. *Carbon* 2012, 50, 1740-1747.

41. Ghenaatian, H. R.; Mousavi, M. F.; Kazemi, S. H.; Shamsipur, M. Electrochemical investigations of self-doped polyaniline nanofibers as a new electroactive material for high performance redox supercapacitor. *Synth. Met.* 2009, 159, 1717-1722.

42. Du, X.; Wang, C.; Chen, M.; Jiao, Y.; Wang, J. Electrochemical performances of nanoparticle Fe3O4/activated carbon supercapacitor using KOH electrolyte solution. *J. Phys. Chem. C* 2009, 113, 2643-2646.

43. Wang, J.; Xu, Y.; Chen, X.; Du, X. Electrochemical supercapacitor electrode material based on poly(3,4-ethylenedioxythiophene)/polypyrrole composite. *J. Power Sources* 2007, 163, 1120-1125.

44. Jeon, J. W.; Ma, Y. G.; Mike, J. F.; Shao, L.; Balbuena, P. B.; Lutkenhaus, J. L. Oxidatively stable polyaniline:polyacid electrodes for electrochemical energy storage. *Phys. Chem. Chem. Phys.* 2013, 15, 9654-9662.

45. Shimano, J. Y.; MacDiarmid, A. G. Polyaniline, a dynamic block copolymer: key to attaining its intrinsic conductivity? *Synth. Met.* 2001, 123, 251-262.

46. Macdiarmid, A. G.; Yang, L. S.; Huang, W. S.; Humphrey, B. D. Polyaniline - electrochemistry and application to rechargeable batteries. *Synth. Met.* 1987, 18, 393-398.

47. Huang, L. M.; Wang, Z. B.; Wang, H. T.; Cheng, X. L.; Mitra, A.; Yan, Y. S. Polyaniline nanowires by electropolymerization from liquid crystalline phases. *J. Mater. Chem.* 2002, 12, 388-391.

48. Choi, S. J.; Park, S. M. Electrochemical growth of nanosized conducting polymer wires on gold using molecular templates. *Adv. Mater.* 2000, 12, 1547-1549.

49. Liu, J. M.; Yang, S. C. Novel colloidal polyaniline fibrils made by template guided chemical polymerization. *J. Chem. Soc.-Chem. Commun.* 1991, 1529-1531.

50. Huang, J.; Virji, S.; Weiller, B. H.; Kaner, R. B. Polyaniline nanofibers: facile synthesis and chemical sensors. *J. Am. Chem. Soc.* 2002, 125, 314-315.

51. Huang, J.; Kaner, R. B. Nanofiber formation in the chemical polymerization of aniline: a mechanistic study. *Angewandte Chemie International Edition* 2004, 43, 5817-5821.

52. Jeon, J. W.; O'Neal, J.; Shao, L.; Lutkenhaus, J. L. Charge storage in polymer acid-doped polyaniline-based layer-by-layer electrodes. *ACS Appl. Mater. Interfaces* 2013, 5, 10127-10136.

53. Novoselov, K. S.; Geim, A. K.; Morozov, S. V.; Jiang, D.; Zhang, Y.; Dubonos, S. V.; Grigorieva, I. V.; Firsov, A. A. Electric field effect in atomically thin carbon films. *Science* 2004, 306, 666-669.

54. Neto, A. C.; Guinea, F.; Peres, N. M. R. Drawing conclusions from graphene. *Phys. World* 2006, 19, 33-37.

55. Bolotin, K. I.; Sikes, K. J.; Jiang, Z.; Klima, M.; Fudenberg, G.; Hone, J.; Kim, P.; Stormer, H. L. Ultrahigh electron mobility in suspended graphene. *Solid State Commun.* 2008, 146, 351-355.

56. Lee, C.; Wei, X. D.; Kysar, J. W.; Hone, J. Measurement of the elastic properties and intrinsic strength of monolayer graphene. *Science* 2008, 321, 385-388.

57. Stoller, M. D.; Park, S. J.; Zhu, Y. W.; An, J. H.; Ruoff, R. S. Graphene-based ultracapacitors. *Nano Lett.* 2008, 8, 3498-3502.

58. Balandin, A. A.; Ghosh, S.; Bao, W. Z.; Calizo, I.; Teweldebrhan, D.; Miao, F.; Lau, C. N. Superior thermal conductivity of single-layer graphene. *Nano Lett.* 2008, 8, 902-907.

59. Gunlycke, D.; Areshkin, D. A.; Li, J. W.; Mintmire, J. W.; White, C. T. Graphene nanostrip digital memory device. *Nano Lett.* 2007, 7, 3608-3611.

60. Wang, X.; Zhi, L. J.; Mullen, K. Transparent, conductive graphene electrodes for dye-sensitized solar cells. *Nano Lett.* 2008, 8, 323-327.

61. Dong, X. C.; Shi, Y. M.; Huang, W.; Chen, P.; Li, L. J. Electrical detection of DNA hybridization with single-base specificity using transistors based on CVD-grown graphene sheets. *Adv. Mater.* 2010, 22, 1649-+.

62. Kim, K. S.; Zhao, Y.; Jang, H.; Lee, S. Y.; Kim, J. M.; Ahn, J. H.; Kim, P.; Choi, J. Y.; Hong, B. H. Large-scale pattern growth of graphene films for stretchable transparent electrodes. *Nature* 2009, 457, 706-710.

63. Lee, S. W.; Yabuuchi, N.; Gallant, B. M.; Chen, S.; Kim, B. S.; Hammond, P. T.; Shao-Horn, Y. High-power lithium batteries from functionalized carbon-nanotube electrodes. *Nat. Nanotechnol.* 2010, 5, 531-537.

64. Wood, J. D.; Schmucker, S. W.; Lyons, A. S.; Pop, E.; Lyding, J. W. Effects of polycrystalline Cu substrate on graphene growth by chemical vapor deposition. *Nano Lett.* 2011, 11, 4547-4554.

65. Emtsev, K. V.; Bostwick, A.; Horn, K.; Jobst, J.; Kellogg, G. L.; Ley, L.; McChesney, J. L.; Ohta, T.; Reshanov, S. A.; Rohrl, J.; Rotenberg, E.; Schmid, A. K.; Waldmann, D.; Weber, H. B.; Seyller, T. Towards wafer-size graphene layers by atmospheric pressure graphitization of silicon carbide. *Nat. Mater.* 2009, 8, 203-207.

66. Norimatsu, W.; Kusunoki, M. Epitaxial graphene on SiC{0001}: advances and perspectives. *Phys. Chem. Chem. Phys.* 2014, 16, 3501-3511.

67. Wang, G. X.; Yang, J.; Park, J.; Gou, X. L.; Wang, B.; Liu, H.; Yao, J. Facile synthesis and characterization of graphene nanosheets. *J. Phys. Chem. C* 2008, 112, 8192-8195.

68. Bai, H.; Li, C.; Shi, G. Q. Functional Composite Materials Based on Chemically Converted Graphene. *Adv. Mater.* 2011, 23, 1089-1115.

69. Sarker, A. K.; Hong, J. D. Layer-by-layer self-assembled multi layer films composed of graphene/polyaniline bilayers: high-energy electrode materials for supercapacitors. *Langmuir* 2012, 28, 12637-12646.

70. Dua, V.; Surwade, S. P.; Ammu, S.; Agnihotra, S. R.; Jain, S.; Roberts, K. E.; Park, S.; Ruoff, R. S.; Manohar, S. K. All-organic vapor sensor using inkjet-printed reduced graphene oxide. *Angew. Chem.-Int. Edit.* 2010, 49, 2154-2157.

71. Shin, H.-J.; Kim, K. K.; Benayad, A.; Yoon, S.-M.; Park, H. K.; Jung, I.-S.; Jin, M. H.; Jeong, H.-K.; Kim, J. M.; Choi, J.-Y.; Lee, Y. H. Efficient reduction of graphite oxide by sodium borohydride and its effect on electrical conductance. *Adv. Funct. Mater.* 2009, 19, 1987-1992.

72. Guo, H. L.; Wang, X. F.; Qian, Q. Y.; Wang, F. B.; Xia, X. H. A green approach to the synthesis of graphene nanosheets. *ACS Nano* 2009, 3, 2653-2659.

73. Becerril, H. A.; Stoltenberg, R. M.; Tang, M. L.; Roberts, M. E.; Liu, Z.; Chen, Y.; Kim, D. H.; Lee, B.-L.; Lee, S.; Bao, Z. Fabrication and evaluation of solution-processed reduced graphene oxide electrodes for p- and n-channel bottom-contact organic thin-film transistors. *ACS Nano* 2010, 4, 6343-6352.

74. Koinuma, M.; Ogata, C.; Kamei, Y.; Hatakeyama, K.; Tateishi, H.; Watanabe, Y.; Taniguchi, T.; Gezuhara, K.; Hayami, S.; Funatsu, A.; Sakata, M.; Kuwahara, Y.; Kurihara, S.; Matsumoto, Y. Photochemical engineering of graphene oxide nanosheets. *J. Phys. Chem. C* 2012, 116, 19822-19827.

75. Chen, B. L.; Xiang, S. C.; Qian, G. D. Metal-organic frameworks with functional pores for recognition of small molecules. *Accounts Chem. Res.* 2010, 43, 1115-1124.

76. Li, J. R.; Kuppler, R. J.; Zhou, H. C. Selective gas adsorption and separation in metal-organic frameworks. *Chem. Soc. Rev.* 2009, 38, 1477-1504.

77. Kitagawa, S.; Kitaura, R.; Noro, S.-i. Functional porous coordination polymers. *Angew. Chem.-Int. Edit.* 2004, 43, 2334-2375.

78. Czaja, A. U.; Trukhan, N.; Muller, U. Industrial applications of metal-organic frameworks. *Chem. Soc. Rev.* 2009, 38, 1284-1293.

79. Burd, S. D.; Ma, S.; Perman, J. A.; Sikora, B. J.; Snurr, R. Q.; Thallapally, P. K.; Tian, J.; Wojtas, L.; Zaworotko, M. J. Highly selective carbon dioxide uptake by [Cu(bpy-n)2(SiF6)] (bpy-1 = 4,4′-Bipyridine; bpy-2 = 1,2-Bis(4-pyridyl)ethene). *J. Am. Chem. Soc.* 2012, 134, 3663-3666.

80. Xiang, Z. H.; Cao, D. P.; Lan, J. H.; Wang, W. C.; Broom, D. P. Multiscale simulation and modelling of adsorptive processes for energy gas storage and

carbon dioxide capture in porous coordination frameworks. *Energy Environ. Sci.* 2010, 3, 1469-1487.

81. Mueller, U.; Schubert, M.; Teich, F.; Puetter, H.; Schierle-Arndt, K.; Pastre, J. Metal-organic frameworks - prospective industrial applications. *J. Mater. Chem.* 2006, 16, 626-636.

82. Wu, C. D.; Hu, A.; Zhang, L.; Lin, W. B. Homochiral porous metal-organic framework for highly enantioselective heterogeneous asymmetric catalysis. *J. Am. Chem. Soc.* 2005, 127, 8940-8941.

83. Matsuda, R.; Kitaura, R.; Kitagawa, S.; Kubota, Y.; Belosludov, R. V.; Kobayashi, T. C.; Sakamoto, H.; Chiba, T.; Takata, M.; Kawazoe, Y.; Mita, Y. Highly controlled acetylene accommodation in a metal-organic microporous material. *Nature* 2005, 436, 238-241.

84. Kwon, H. T.; Jeong, H. K. In situ synthesis of thin zeolitic-imidazolate framework ZIF-8 membranes exhibiting exceptionally high propylene/propane separation. *J. Am. Chem. Soc.* 2013, 135, 10763-10768.

85. Liu, B.; Shioyama, H.; Jiang, H. L.; Zhang, X. B.; Xu, Q. Metal-organic framework (MOF) as a template for syntheses of nanoporous carbons as electrode materials for supercapacitor. *Carbon* 2010, 48, 456-463.

86. Liu, B.; Shioyama, H.; Akita, T.; Xu, Q. Metal-organic framework as a template for porous carbon synthesis. *J. Am. Chem. Soc.* 2008, 130, 5390-+.

87. Jiang, H.-L.; Liu, B.; Lan, Y.-Q.; Kuratani, K.; Akita, T.; Shioyama, H.; Zong, F.; Xu, Q. From metal–organic framework to nanoporous carbon: toward a very high surface area and hydrogen uptake. *J. Am. Chem. Soc.* 2011, 133, 11854-11857.

88. Xia, W.; Qiu, B.; Xia, D. G.; Zou, R. Q. Facile preparation of hierarchically porous carbons from metal-organic gels and their application in energy storage. *Sci Rep* 2013, 3.

89. Torad, N. L.; Hu, M.; Kamachi, Y.; Takai, K.; Imura, M.; Naito, M.; Yamauchi, Y. Facile synthesis of nanoporous carbons with controlled particle sizes by direct carbonization of monodispersed ZIF-8 crystals. *Chem. Commun.* 2013, 49, 2521-2523.

90. Decher, G.; Hong, J. D.; Schmitt, J. Buildup of ultrathin multilayer films by a self-assembly process .3. consecutively alternating adsorption of anionic and cationic polyelectrolytes on charged surfaces. *Thin Solid Films* 1992, 210, 831-835.

91. Tang, Z.; Wang, Y.; Podsiadlo, P.; Kotov, N. A. Biomedical applications of layer-by-layer assembly: from biomimetics to tissue engineering. *Adv. Mater.* 2006, 18, 3203-3224.

92. Ariga, K.; Hill, J. P.; Ji, Q. M. Layer-by-layer assembly as a versatile bottom-up nanofabrication technique for exploratory research and realistic application. *Phys. Chem. Chem. Phys.* 2007, 9, 2319-2340.

93. Chiarelli, P. A.; Johal, M. S.; Casson, J. L.; Roberts, J. B.; Robinson, J. M.; Wang, H. L. Controlled fabrication of polyelectrolyte multilayer thin films using spin-assembly. *Adv. Mater.* 2001, 13, 1167-+.

94. Hyder, M. N.; Lee, S. W.; Cebeci, F. C.; Schmidt, D. J.; Shao-Horn, Y.; Hammond, P. T. Layer-by-layer assembled polyaniline nanofiber/multiwall carbon nanotube thin film electrodes for high-power and high-energy storage applications. *ACS Nano* 2011, 5, 8552-8561.

95. Kim, S. Y.; Hong, J.; Kavian, R.; Lee, S. W.; Hyder, M. N.; Shao-Horn, Y.; Hammond, P. T. Rapid fabrication of thick spray-layer-by-layer carbon nanotube electrodes for high power and energy devices. *Energy Environ. Sci.* 2013, 6, 888-897.

96. Decher, G. Fuzzy nanoassemblies: toward layered polymeric multicomposites. *Science* 1997, 277, 1232-1237.

97. Yang, Y. H.; Bolling, L.; Priolo, M. A.; Grunlan, J. C. Super gas barrier and selectivity of graphene oxide-polymer multilayer thin films. *Adv. Mater.* 2013, 25, 503-508.

98. Andres, C. M.; Kotov, N. A. Inkjet deposition of layer-by-layer assembled films. *J. Am. Chem. Soc.* 2010, 132, 14496-14502.

99. He, J. A.; Valluzzi, R.; Yang, K.; Dolukhanyan, T.; Sung, C. M.; Kumar, J.; Tripathy, S. K.; Samuelson, L.; Balogh, L.; Tomalia, D. A. Electrostatic multilayer deposition of a gold-dendrimer nanocomposite. *Chem. Mat.* 1999, 11, 3268-3274.

100. Lvov, Y.; Ariga, K.; Ichinose, I.; Kunitake, T. Assembly of multicomponent protein films by means of electrostatic layer-by-layer adsorption. *J. Am. Chem. Soc.* 1995, 117, 6117-6123.

101. Lvov, Y.; Decher, G.; Sukhorukov, G. Assembly of thin-films by means of successive deposition of alternate layers of DNA and poly(allylamine). *Macromolecules* 1993, 26, 5396-5399.

102. Cheung, J. H.; Stockton, W. B.; Rubner, M. F. Molecular-level processing of conjugated polymers .3. layer-by-layer manipulation of polyaniline via electrostatic interactions. *Macromolecules* 1997, 30, 2712-2716.

103. Briscoe, J.; Gallardo, D. E.; Hatch, S.; Lesnyak, V.; Gaponik, N.; Dunn, S. Enhanced quantum dot deposition on ZnO nanorods for photovoltaics through layer-by-layer processing. *J. Mater. Chem.* 2011, 21, 2517-2523.

104. Choi, S.; Jin, H.; Bang, J.; Kim, S. Layer-by-layer quantum dot assemblies for the enhanced energy transfers and their applications toward efficient solar cells. *J. Phys. Chem. Lett.* 2012, 3, 3442-3447.

105. Lee, D.; Omolade, D.; Cohen, R. E.; Rubner, M. F. pH-Dependent structure and properties of TiO_2/SiO_2 nanoparticle multilayer thin films. *Chem. Mat.* 2007, 19, 1427-1433.

106. Hyder, M. N.; Gallant, B. M.; Shah, N. J.; Shao-Horn, Y.; Hammond, P. T. Synthesis of highly stable sub-8 nm TiO2 nanoparticles and their multilayer electrodes of TiO2/MWNT for electrochemical applications. *Nano Lett.* 2013, 13, 4610-4619.

107. Lutkenhaus, J. L.; McEnnis, K.; Hammond, P. T. Tuning the glass transition of and ion transport within hydrogen-bonded layer-by-layer assemblies. *Macromolecules* 2007, 40, 8367-8373.

108. Shimazaki, Y.; Mitsuishi, M.; Ito, S.; Yamamoto, M. Preparation of the layer-by-layer deposited ultrathin film based on the charge-transfer interaction. *Langmuir* 1997, 13, 1385-1387.

109. Lojou, É.; Bianco, P. Buildup of polyelectrolyte−protein multilayer assemblies on gold electrodes. role of the hydrophobic effect. *Langmuir* 2004, 20, 748-755.

110. Joseph, N.; Ahmadiannamini, P.; Hoogenboom, R.; Vankelecom, I. F. J. Layer-by-layer preparation of polyelectrolyte multilayer membranes for separation. *Polymer Chemistry* 2014, 5, 1817-1831.

111. Lutkenhaus, J. L.; Hammond, P. T. Electrochemically enabled polyelectrolyte multilayer devices: from fuel cells to sensors. *Soft Matter* 2007, 3, 804-816.

112. Bieker, P.; Sch nh off, M. Linear and exponential growth regimes of multilayers of weak polyelectrolytes in dependence on pH. *Macromolecules* 2010, 43, 5052-5059.

113. Alonso, T.; Irigoyen, J.; Iturri, J. J.; larena, I. L.; Moya, S. E. Study of the multilayer assembly and complex formation of poly(diallyldimethylammonium chloride) (PDADMAC) and poly(acrylic acid) (PAA) as a function of pH. *Soft Matter* 2013, 9, 1920-1928.

114. Cho, C.; Jeon, J. W.; Lutkenhaus, J.; Zacharia, N. S. Electric field induced morphological transitions in polyelectrolyte multilayers. *ACS Appl. Mater. Interfaces* 2013, 5, 4930-4936.

115. Hsu, B. B.; Hagerman, S. R.; Jamieson, K.; Veselinovic, J.; O'Neill, N.; Holler, E.; Ljubimova, J. Y.; Hammond, P. T. Multi layer films assembled from naturally-derived materials for controlled protein release. *Biomacromolecules* 2014, 15, 2049-2057.

116. Wood, K. C.; Boedicker, J. Q.; Lynn, D. M.; Hammond, P. T. Tunable drug release from hydrolytically degradable layer-by-layer thin films. *Langmuir* 2005, 21, 1603-1609.

117. Raoufi, N.; Surre, F.; Sun, T.; Rajarajan, M.; Grattan, K. T. V. Wavelength dependent pH optical sensor using the layer-by-layer technique. *Sensors and Actuators B: Chemical* 2012, 169, 374-381.

118. Zhang, B.; Cui, T. An ultrasensitive and low-cost graphene sensor based on layer-by-layer nano self-assembly. *Appl. Phys. Lett.* 2011, 98, -.

119. Lee, H.; Alcaraz, M. L.; Rubner, M. F.; Cohen, R. E. Zwitter-wettability and antifogging coatings with frost-resisting capabilities. *ACS Nano* 2013, 7, 2172-2185.

120. Chevallier, P.; Turgeon, S. p.; Sarra-Bournet, C.; Turcotte, R. l.; Laroche, G. t. Characterization of multilayer anti-fog coatings. *ACS Appl. Mater. Interfaces* 2011, 3, 750-758.

121. Podsiadlo, P.; Paternel, S.; Rouillard, J. M.; Zhang, Z. F.; Lee, J.; Lee, J. W.; Gulari, L.; Kotov, N. A. Layer-by-layer assembly of nacre-like nanostructured composites with antimicrobial properties. *Langmuir* 2005, 21, 11915-11921.

122. Onitsuka, O.; Fou, A. C.; Ferreira, M.; Hsieh, B. R.; Rubner, M. F. Enhancement of light emitting diodes based on self-assembled heterostructures of poly(p-phenylene vinylene). *J. Appl. Phys.* 1996, 80, 4067-4071.

123. Shchukin, D. G.; Zheludkevich, M.; Yasakau, K.; Lamaka, S.; Ferreira, M. G. S.; Mohwald, H. Layer-by-layer assembled nanocontainers for self-healing corrosion protection. *Adv. Mater.* 2006, 18, 1672-+.

124. Zheludkevich, M. L.; Shchukin, D. G.; Yasakau, K. A.; Mohwald, H.; Ferreira, M. G. S. Anticorrosion coatings with self-healing effect based on nanocontainers impregnated with corrosion inhibitor. *Chem. Mat.* 2007, 19, 402-411.

125. Byon, H. R.; Lee, S. W.; Chen, S.; Hammond, P. T.; Shao-Horn, Y. Thin films of carbon nanotubes and chemically reduced graphenes for electrochemical micro-capacitors. *Carbon* 2011, 49, 457-467.

126. Lee, S. W.; Kim, J.; Chen, S.; Hammond, P. T.; Shao-Horn, Y. Carbon nanotube/manganese oxide ultrathin film electrodes for electrochemical capacitors. *ACS Nano* 2010, 4, 3889-3896.

127. Lee, S. W.; Kim, B. S.; Chen, S.; Shao-Horn, Y.; Hammond, P. T. Layer-by-layer assembly of all carbon nanotube ultrathin films for electrochemical applications. *J. Am. Chem. Soc.* 2009, 131, 671-679.

128. Virji, S.; Huang, J. X.; Kaner, R. B.; Weiller, B. H. Polyaniline nanofiber gas sensors: examination of response mechanisms. *Nano Lett.* 2004, 4, 491-496.

129. Tseng, R. J.; Huang, J. X.; Ouyang, J.; Kaner, R. B.; Yang, Y. Polyaniline nanofiber/gold nanoparticle nonvolatile memory. *Nano Lett.* 2005, 5, 1077-1080.

130. Pandey, R. K.; Lakshminarayanan, V. Electro-oxidation of formic acid, methanol, and ethanol on electrodeposited pd-polyaniline nanofiber films in acidic and alkaline medium. *J. Phys. Chem. C* 2009, 113, 21596-21603.

131. Genies, E. M.; Hany, P.; Santier, C. A rechargeable battery of the type polyaniline propylene carbonate - $LiClO_4$-Li-Al. *J. Appl. Electrochem.* 1988, 18, 751-756.

132. Ran, F.; Tan, Y. T.; Liu, J.; Zhao, L.; Kong, L. B.; Luo, Y. C.; Kang, L. Preparation of hierarchical polyaniline nanotubes based on self-assembly and its electrochemical capacitance. *Polym. Adv. Technol.* 2012, 23, 1297-1301.

133. Shaikh, S. F.; Lim, J. Y.; Mane, R. S.; Han, S. H.; Ambade, S. B.; Joo, O. S. Wet-chemical polyaniline nanorice mass-production for electrochemical supercapacitors. *Synth. Met.* 2012, 162, 1303-1307.

134. Gupta, V.; Miura, N. High performance electrochemical supercapacitor from electrochemically synthesized nanostructured polyaniline. *Mater. Lett.* 2006, 60, 1466-1469.

135. Sivakkumar, S. R.; Oh, J. S.; Kim, D. W. Polyaniline nanofibres as a cathode material for rechargeable lithium-polymer cells assembled with gel polymer electrolyte. *J. Power Sources* 2006, 163, 573-577.

136. Gowda, S. R.; Reddy, A.; Zhan, X. B.; Ajayan, P. M. Building energy storage device on a single nanowire. *Nano Lett.* 2011, 11, 3329-3333.

137. Mazeikiene, R.; Malinauskas, A. Electrochemical stability of polyaniline. *Eur. Polym. J.* 2002, 38, 1947-1952.

138. Simoes, F. R.; Pocrifka, L. A.; Marchesi, L.; Pereira, E. C. Investigation of electrochemical degradation process in polyaniline/polystyrene sulfonated self-assembly films by impedance spectroscopy. *J. Phys. Chem. B* 2011, 115, 11092-11097.

139. Manuel, J.; Raghavan, P.; Shin, C.; Heo, M. Y.; Ahn, J. H.; Noh, J. P.; Cho, G. B.; Ryu, H. S.; Ahn, H. J. Electrosprayed polyaniline as cathode material for lithium secondary batteries. *Mater. Res. Bull.* 2010, 45, 265-268.

140. Oyama, N.; Tatsuma, T.; Sato, T.; Sotomura, T. Dimercaptan-polyaniline composite electrodes for lithium batteries with high-energy density. *Nature* 1995, 373, 598-600.

141. Genies, E. M.; Lapkowski, M.; Santier, C.; Vieil, E. Polyaniline, spectroelectrochemistry, display and battery. *Synth. Met.* 1987, 18, 631-636.

142. Hung, P. J.; Chang, K. H.; Lee, Y. F.; Hu, C. C.; Lin, K. M. Ideal asymmetric supercapacitors consisting of polyaniline nanofibers and graphene nanosheets with proper complementary potential windows. *Electrochim. Acta* 2010, 55, 6015-6021.

143. He, B. L.; Dong, B.; Wang, W.; Li, H. L. Performance of polyaniline/multi-walled carbon nanotubes composites as cathode for rechargeable lithium batteries. *Mater. Chem. Phys.* 2009, 114, 371-375.

144. Daprano, G.; Leclerc, M.; Zotti, G. Stabilization and characterization of pernigraniline salt - the acid-doped form of fully oxidized polyanilines. *Macromolecules* 1992, 25, 2145-2150.

145. Bazito, F. F. C.; Silveira, L. T.; Torresi, R. M.; de Torresi, S. I. C. On the stabilization of conducting pernigraniline salt by the synthesis and oxidation of polyaniline in hydrophobic ionic liquids. *Phys. Chem. Chem. Phys.* 2008, 10, 1457-1462.

146. Lu, W.; Fadeev, A. G.; Qi, B. H.; Mattes, B. R. Fabricating conducting polymer electrochromic devices using ionic liquids. *J. Electrochem. Soc.* 2004, 151, H33-H39.

147. Tsutsumi, H.; Fukuzawa, S.; Ishikawa, M.; Morita, M.; Matsuda, Y. Polyaniline-poly p-styrenesulfonic acid-co-methoxy-oliga(ethylene glycol)acrylate composite electrode for all-solid-state rechargeable lithium battery. *J. Electrochem. Soc.* 1995, 142, L168-L170.

148. Tarver, J.; Yoo, J. E.; Dennes, T. J.; Schwartz, J.; Loo, Y. L. Polymer acid doped polyaniline is electrochemically stable beyond pH 9. *Chem. Mat.* 2009, 21, 280-286.

149. Bucholz, T.; Sun, Y. M.; Loo, Y. L. Near-monodispersed polyaniline particles through template synthesis and simultaneous doping with diblock copolymers of PMA and PAAMPSA. *J. Mater. Chem.* 2008, 18, 5835-5842.

150. Sun, L. F.; Liu, H. B.; Clark, R.; Yang, S. C. Double-strand polyaniline. *Synth. Met.* 1997, 84, 67-68.

151. Lee, K. S.; Blanchet, G. B.; Gao, F.; Loo, Y. L. Direct patterning of conductive water-soluble polyaniline for thin-film organic electronics. *Appl. Phys. Lett.* 2005, 86.

152. Lee, K. S.; Smith, T. J.; Dickey, K. C.; Yoo, J. E.; Stevenson, K. J.; Loo, Y. L. High-resolution characterization of pentacene/polyaniline interfaces in thin-film transistors. *Adv. Funct. Mater.* 2006, 16, 2409-2414.

153. Mano, N.; Yoo, J. E.; Tarver, J.; Loo, Y. L.; Heller, A. An electron-conducting cross-linked polyaniline-based redox hydrogel, formed in one step at pH 7.2, wires glucose oxidase. *J. Am. Chem. Soc.* 2007, 129, 7006-+.

154. Yoo, J. E.; Cross, J. L.; Bucholz, T. L.; Lee, K. S.; Espe, M. P.; Loo, Y. L. Improving the electrical conductivity of polymer acid-doped polyaniline by controlling the template molecular weight. *J. Mater. Chem.* 2007, 17, 1268-1275.

155. Yoo, J. E.; Bucholz, T. L.; Jung, S. Y.; Loo, Y. L. Narrowing the size distribution of the polymer acid improves PANI conductivity. *J. Mater. Chem.* 2008, 18, 3129-3135.

156. Yoo, J. E.; Krekelberg, W. P.; Sun, Y. M.; Tarver, J. D.; Truskett, T. M.; Loo, Y. L. Polymer conductivity through particle connectivity. *Chem. Mat.* 2009, 21, 1948-1954.

157. Tarver, J.; Yoo, J. E.; Loo, Y. L. Polyaniline exhibiting stable and reversible switching in the visible extending into the near-IR in aqueous media. *Chemistry of Materials* 2010, 22, 2333-2340.

158. Yoo, J. E.; Lee, K. S.; Garcia, A.; Tarver, J.; Gomez, E. D.; Baldwin, K.; Sun, Y. M.; Meng, H.; Nguyen, T. Q.; Loo, Y. L. Directly patternable, highly conducting polymers for broad applications in organic electronics. *Proc. Natl. Acad. Sci. U. S. A.* 2010, 107, 5712-5717.

159. Chiang, J. C.; Macdiarmid, A. G. Polyaniline - protonic acid doping of the emeraldine form to the metallic regime. *Synth. Met.* 1986, 13, 193-205.

160. Huang, W. S.; Humphrey, B. D.; Macdiarmid, A. G. Polyaniline, a novel conducting polymer - mophology and chemistry of its oxidation and reduction in aqueous-electrolytes. *J. Chem. Soc., Faraday Trans.* 1986, 82, 2385-2400.

161. Wang, Y.; Qian, W. P.; Tan, Y.; Ding, S. H.; Zhang, H. Q. Direct electrochemistry and electroanalysis of hemoglobin adsorbed in self-assembled films of gold nanoshells. *Talanta* 2007, 72, 1134-1140.

162. Becke, A. D. Density-functional thermochemistry .3. the role of exact exchange. *J. Chem. Phys.* 1993, 98, 5648-5652.

163. Lee, C. T.; Yang, W. T.; Parr, R. G. Development of the colle-salvetti correlation-energy formula into a functional of the electron-density. *Phys. Rev. B* 1988, 37, 785-789.

164. Breneman, C. M.; Wiberg, K. B. Determining atom-centered monopoles from molecular electrostatic potentials - the need for high sampling density in formamide conformational-analysis. *J. Comput. Chem.* 1990, 11, 361-373.

165. Kirkpatrick, S.; Gelatt, C. D.; Vecchi, M. P. Optimization by simulated annealing. *Science* 1983, 220, 671-680.

166. Mayo, S. L.; Olafson, B. D.; Goddard, W. A. Dreiding - a generic force-field for molecular simulations. *J. Phys. Chem.* 1990, 94, 8897-8909.

167. Murthy, A.; Manthiram, A. Highly water-dispersible, mixed ionic-electronic conducting, polymer acid-doped polyanilines as ionomers for direct methanol fuel cells. *Chem. Commun.* 2011, 47, 6882-6884.

168. Kontou, E.; Anthoulis, G. The effect of silica nanoparticles on the thermomechanical properties of polystyrene. *J. Appl. Polym. Sci.* 2007, 105, 1723-1731.

169. Arasi, A. Y.; Jeyakumari, J. J. L.; Sundaresan, B.; Dhanalakshmi, V.; Anbarasan, R. The structural properties of poly(aniline)-analysis via FTIR spectroscopy. *Spectroc. Acta Pt. A-Molec. Biomolec. Spectr.* 2009, 74, 1229-1234.

170. Trchova, M.; Sedenkova, I.; Tobolkova, E.; Stejskal, J. FTIR spectroscopic and conductivity study of the thermal degradation of polyaniline films. *Polym. Degrad. Stabil.* 2004, 86, 179-185.

171. Silverstein, R. M., Webster F. X. Spectrometric identification of organic compounds. *John Wiley & Sons, Inc.* 1998.

172. Yue, J.; Epstein, A. J. XPS study of self-doped conducting polyaniline and parent systems. *Macromolecules* 1991, 24, 4441-4445.

173. Kim, J. Y.; Jung, J. H.; Lee, D. E.; Joo, J. Enhancement of electrical conductivity of poly(3,4-ethylenedioxythiophene)/poly(4-styrenesulfonate) by a change of solvents. *Synth. Met.* 2002, 126, 311-316.

174. Morita, M.; Miyazaki, S.; Tanoue, H.; Ishikawa, M.; Matsuda, Y. Electrochemical-behavior of polyaniline-poly(styrene sulfonate) composite films in organic electrolyte-solutions. *J. Electrochem. Soc.* 1994, 141, 1409-1413.

175. Morita, M.; Miyazaki, S.; Ishikawa, M.; Matsuda, Y.; Tajima, H.; Adachi, K.; Anan, F. Charge discharge characteristics of polyaniline-based polymer composite positives for rechargeable lithium batteries. *J. Power Sources* 1995, 54, 214-217.

176. Osaka, T.; Momma, T.; Nishimura, K. Electroactivity change of electropolymerized polypyrrole polystyrenesulfonate composite film in some organic electrolytes. *Chem. Lett.* 1992, 1787-1790.

177. Heinze, J.; Dietrich, M.; Mortensen, J. On the redox properties of conducting polymers. *Makromolekulare Chemie-Macromolecular Symposia* 1987, 8, 73-81.

178. Rossberg, K.; Paasch, G.; Dunsch, L.; Ludwig, S. The influence of porosity and the nature of the charge storage capacitance on the impedance behaviour of electropolymerized polyaniline films. *J. Electroanal. Chem.* 1998, 443, 49-62.

179. Smyrl, W. H. L., M. Applications of electroactive polymers. *ed. B. Scrosati, Chapman & Hall, London* 1993, 29-74.

180. Krishnan, R.; Lu, T.-M.; Koratkar, N. Functionally strain-graded nanoscoops for high power Li-ion battery anodes. *Nano Lett.* 2010, 11, 377-384.

181. Dudney, J. N. Thin film micro-batteries. *Electrochem. Soc. Interface* 2008, 17, 44-48.

182. Krishnan, R.; Lu, T. M.; Koratkar, N. Functionally strain-graded nanoscoops for high power Li-ion battery anodes. *Nano Lett.* 2011, 11, 377-384.

183. Stejskal, J.; Spirkova, M.; Kratochvil, P. Polyaniline dispersions .4. polymerization seeded by polyaniline particles. *Acta Polym.* 1994, 45, 385-388.

184. Cao, Y.; Smith, P.; Heeger, A. J. Spectroscopic studies of polyaniline in solution and in spin-cast films. *Synth. Met.* 1989, 32, 263-281.

185. Nekrasov, A. A.; Ivanov, V. F.; Vannikov, A. V. Analysis of the structure of polyaniline absorption spectra based on spectroelectrochemical data. *J. Electroanal. Chem.* 2000, 482, 11-17.

186. Sun, Y.; Macdiarmid, A. G.; Epstein, A. J. Polyaniline - synthesis and characterization of pernigraniline base. *J. Chem. Soc.-Chem. Commun.* 1990, 529-531.

187. Song, H. K.; Palmore, G. T. R. Redox-active polypyrrole: Toward polymer-based batteries. *Adv. Mater.* 2006, 18, 1764-+.

188. Laforgue, A.; Simon, P.; Sarrazin, C.; Fauvarque, J. F. Polythiophene-based supercapacitors. *J. Power Sources* 1999, 80, 142-148.

189. Macinnes, D.; Druy, M. A.; Nigrey, P. J.; Nairns, D. P.; Macdiarmid, A. G.; Heeger, A. J. Organic batteries - reversible n-type and p-type electrochemical doping of polyacetylene, (CH)x. *J. Chem. Soc.-Chem. Commun.* 1981, 317-319.

190. Fusalba, F.; Gouerec, P.; Villers, D.; Belanger, D. Electrochemical characterization of polyaniline in nonaqueous electrolyte and its evaluation as electrode material for electrochemical supercapacitors. *J. Electrochem. Soc.* 2001, 148, A1-A6.

191. Kitani, A.; Kaya, M.; Sasaki, K. Performance study of aqueous polyaniline batteries. *J. Electrochem. Soc.* 1986, 133, 1069-1073.

192. Ghenaatian, H. R.; Mousavi, M. F.; Rahmanifar, M. S. High performance hybrid supercapacitor based on two nanostructured conducting polymers: Self-doped polyaniline and polypyrrole nanofibers. *Electrochim. Acta* 2012, 78, 212-222.

193. Cao, Y.; Smith, P.; Heeger, A. J. Counterion induced processibility of conducting polyaniline and of conducting polyblends of polyaniline in bulk polymers. *Synth. Met.* 1992, 48, 91-97.

194. Kang, E. T.; Neoh, K. G.; Tan, K. L. Polyaniline: A polymer with many interesting intrinsic redox states. *Prog. Polym. Sci.* 1998, 23, 277-324.

195. Huang, J. X.; Kaner, R. B. Nanofiber formation in the chemical polymerization of aniline: A mechanistic study. *Angew. Chem.-Int. Edit.* 2004, 43, 5817-5821.

196. Shao, L.; Jeon, J.-W.; Lutkenhaus, J. L. Polyaniline/Vanadium Pentoxide Layer-by-Layer Electrodes for Energy Storage. *Chem. Mat.* 2011, 24, 181-189.

197. Mike, J. F.; Lutkenhaus, J. L. Electrochemically active polymers for electrochemical energy storage: opportunities and challenges. *ACS Macro Letters* 2013, 839-844.

198. Heller, A.; Feldman, B. J.; Mano, N.; Loo, Y.-L. Crosslinked adduct of polyaniline and polymer acid containing redox enzyme for electrochemical sensor. US 08080385, Dec 20 2011.

199. Vidyasagar, A.; Sung, C.; Gamble, R.; Lutkenhaus, J. L. Thermal transitions in dry and hydrated layer-by-layer assemblies exhibiting linear and exponential growth. *ACS Nano* 2012, 6, 6174-6184.

200. Tang, Z. Y.; Wang, Y.; Podsiadlo, P.; Kotov, N. A. Biomedical applications of layer-by-layer assembly: From biomimetics to tissue engineering. *Adv. Mater.* 2006, 18, 3203-3224.

201. Cho, J.; Char, K.; Hong, J. D.; Lee, K. B. Fabrication of highly ordered multilayer films using a spin self-assembly method. *Adv. Mater.* 2001, 13, 1076-+.

202. Schlenoff, J. B.; Dubas, S. T.; Farhat, T. Sprayed polyelectrolyte multilayers. *Langmuir* 2000, 16, 9968-9969.

203. DeLongchamp, D. M.; Kastantin, M.; Hammond, P. T. High-contrast electrochromism from layer-by-layer polymer films. *Chem. Mat.* 2003, 15, 1575-1586.

204. DeLongchamp, D.; Hammond, P. T. Layer-by-layer assembly of PEDOT/polyaniline electrochromic devices. *Adv. Mater.* 2001, 13, 1455-+.

205. Sung, C.; Vidyasagar, A.; Hearn, K.; Lutkenhaus, J. L. Effect of thickness on the thermal properties of hydrogen-bonded LbL assemblies. *Langmuir* 2012, 28, 8100-8109.

206. Gu, X. K.; Knorr, D. B.; Wang, G. J.; Overney, R. M. Local thermal-mechanical analysis of ultrathin interfacially mixed poly(ethylene oxide)/poly(acrylic acid) layer-by-layer electrolyte assemblies. *Thin Solid Films* 2011, 519, 5955-5961.

207. Laufer, G.; Kirkland, C.; Cain, A. A.; Grunlan, J. C. Clay-chitosan nanobrick walls: completely renewable gas barrier and flame-retardant nanocoatings. *ACS Appl. Mater. Interfaces* 2012, 4, 1643-1649.

208. Yang, Y. H.; Haile, M.; Park, Y. T.; Malek, F. A.; Grunlan, J. C. Super gas barrier of all-polymer multilayer thin films. *Macromolecules* 2011, 44, 1450-1459.

209. Zakharova, L. Y.; Ibragimova, A. R.; Valeeva, F. G.; Zakharov, A. V.; Mustafina, A. R.; Kudryavtseva, L. A.; Harlampidi, H. E.; Konovalov, A. I. Nanosized reactors based on polyethyleneimines: From microheterogeneous systems to immobilized catalysts. *Langmuir* 2007, 23, 3214-3224.

210. Tarachiwin, L.; Kiattibutr, P.; Ruangchuay, L.; Sirivat, A.; Schwank, J. Electrical conductivity response of polyaniline films to ethanol-water mixtures. *Synth. Met.* 2002, 129, 303-308.

211. Chen, R.; Benicewicz, B. C. Substituted oligoanilines: synthesis and characterization. *Synth. Met.* 2004, 146, 133-137.

212. Huang, W. S.; Macdiarmid, A. G. Optical-properties of polyaniline. *Polymer* 1993, 34, 1833-1845.

213. Vaschetto, M. E.; Retamal, B. A. Substituents effect on the electronic properties of aniline and oligoanilines. *J. Phys. Chem. A* 1997, 101, 6945-6950.

214. Xia, Y. N.; Wiesinger, J. M.; Macdiarmid, A. G.; Epstein, A. J. Camphorsulfonic acid fully doped polyaniline emeraldine salt - conformations in different solvents studied by an ultraviolet-visible near-infrared spectroscopic method. *Chem. Mat.* 1995, 7, 443-445.

215. Macdiarmid, A. G.; Epstein, A. J. The concept of secondary doping as applied to polyaniline. *Synth. Met.* 1994, 65, 103-116.

216. Ping, Z. In situ FTIR-attenuated total reflection spectroscopic investigations on the base-acid transitions of polyaniline. Base-acid transition in the emeraldine form of polyaniline. *J. Chem.Soc.-Faraday T.* 1996, 92, 3063-3067.

217. Baibarac, M.; Baltog, I.; Lefrant, S.; Mevellec, J. Y.; Chauvet, O. Polyaniline and carbon nanotubes based composites containing whole units and fragments of nanotubes. *Chem. Mat.* 2003, 15, 4149-4156.

218. Murugan, A. V.; Muraliganth, T.; Manthiram, A. Rapid, facile microwave-solvothermal synthesis of graphene nanosheets and their polyaniline nanocomposites for energy strorage. *Chem. Mat.* 2009, 21, 5004-5006.

219. Silverstein, R. M.; Webster, F. X. *Spectrometric identification of organic compounds*. 6th ed.; John Wiley & Sons, Inc., Hoboken, New Jersey, 1998.

220. Li, J.; Zhu, L. H.; Wu, Y. H.; Harima, Y.; Zhang, A. Q.; Tang, H. Q. Hybrid composites of conductive polyaniline and nanocrystalline titanium oxide prepared via self-assembling and graft polymerization. *Polymer* 2006, 47, 7361-7367.

221. Hao, Q. L.; Wang, H. L.; Yang, X. J.; Lu, L. D.; Wang, X. Morphology-controlled fabrication of sulfonated graphene/polyaniline nanocomposites by liquid/liquid interfacial polymerization and investigation of their electrochemical properties. *Nano Res.* 2011, 4, 323-333.

222. Liu, L.; Tian, F. H.; Zhou, M.; Guo, H. P.; Wang, X. Y. Aqueous rechargeable lithium battery based on polyaniline and LiMn2O4 with good cycling performance. *Electrochim. Acta* 2012, 70, 360-364.

223. Cutler, C. A.; Bouguettaya, M.; Reynolds, J. R. PEDOT polyelectrolyte based electrochromic films via electrostatic adsorption. *Adv. Mater.* 2002, 14, 684-688.

224. D'Aprano, G.; Leclerc, M.; Zotti, G. Stabilization and characterization of pernigraniline salt - the acid-doped form of fully oxidized polyanilines. *Macromolecules* 1992, 25, 2145-2150.

225. Nathan, M. Microbattery technologies for miniaturized implantable medical devices. *Curr. Pharm. Biotechnol.* 2010, 11, 404-410.

226. Koo, M.; Park, K.-I.; Lee, S. H.; Suh, M.; Jeon, D. Y.; Choi, J. W.; Kang, K.; Lee, K. J. Bendable inorganic thin-film battery for fully flexible electronic systems. *Nano Lett.* 2012, 12, 4810-4816.

227. Beidaghi, M.; Gogotsi, Y. Capacitive energy storage in micro-scale devices: recent advances in design and fabrication of micro-supercapacitors. *Energy Environ. Sci.* 2014, 7, 867-884.

228. Dudney, N. J.; Neudecker, B. J. Solid state thin-film lithium battery systems. *Curr. Opin. Solid State Mater. Sci.* 1999, 4, 479-482.

229. Bates, J. B.; Dudney, N. J.; Neudecker, B.; Ueda, A.; Evans, C. D. Thin-film lithium and lithium-ion batteries. *Solid State Ionics* 2000, 135, 33-45.

230. Zhou, Y.-N.; Xue, M.-Z.; Fu, Z.-W. Nanostructured thin film electrodes for lithium storage and all-solid-state thin-film lithium batteries. *J. Power Sources* 2013, 234, 310-332.

231. Chen, H. H.; Cartmell, S.; Wang, Q.; Lozano, T.; Deng, Z. D.; Li, H. D.; Chen, X. L.; Yuan, Y.; Gross, M. E.; Carlson, T. J.; Xiao, J. Micro-battery development for juvenile salmon acoustic telemetry system applications. *Sci Rep* 2014, 4.

232. Albano, F.; Lin, Y. S.; Blaauw, D.; Sylvester, D. M.; Wise, K. D.; Sastry, A. M. A fully integrated microbattery for an implantable microelectromechanical system. *J. Power Sources* 2008, 185, 1524-1532.

233. Hu, L. B.; Pasta, M.; La Mantia, F.; Cui, L. F.; Jeong, S.; Deshazer, H. D.; Choi, J. W.; Han, S. M.; Cui, Y. Stretchable, porous, and conductive energy textiles. *Nano Lett.* 2010, 10, 708-714.

234. Hu, L. B.; Choi, J. W.; Yang, Y.; Jeong, S.; La Mantia, F.; Cui, L. F.; Cui, Y. Highly conductive paper for energy-storage devices. *Proc. Natl. Acad. Sci. U. S. A.* 2009, 106, 21490-21494.

235. Islam, M. S.; Fisher, C. A. J. Lithium and sodium battery cathode materials: computational insights into voltage, diffusion and nanostructural properties. *Chem. Soc. Rev.* 2014, 43, 185-204.

236. Du Pasquier, A.; Plitz, I.; Menocal, S.; Amatucci, G. A comparative study of Li-ion battery, supercapacitor and nonaqueous asymmetric hybrid devices for automotive applications. *J. Power Sources* 2003, 115, 171-178.

237. Ohzuku, T.; Ueda, A. Solid-state redox reactions of LiCoO2 (R(3)over-Bar-M) for 4 volt secondary lithium cells. *J. Electrochem. Soc.* 1994, 141, 2972-2977.

238. Manthiram, A.; Vadivel Murugan, A.; Sarkar, A.; Muraliganth, T. Nanostructured electrode materials for electrochemical energy storage and conversion. *Energy Environ. Sci.* 2008, 1, 621-638.

239. Mike, J. F.; Lutkenhaus, J. L. Recent advances in conjugated polymer energy storage. *J. Polym. Sci. Pt. B-Polym. Phys.* 2013, 51, 468-480.

240. Shao, L.; Jeon, J. W.; Lutkenhaus, J. L. Porous polyaniline nanofiber/vanadium pentoxide layer-by-layer electrodes for energy storage. *J. Mater. Chem. A* 2013, 1, 7648-7656.

241. Yamada, A.; Chung, S. C.; Hinokuma, K. Optimized LiFePO4 for lithium battery cathodes. *J. Electrochem. Soc.* 2001, 148, A224-A229.

242. Sathiya, M.; Prakash, A. S.; Ramesha, K.; Tarascon, J. M.; Shukla, A. K. V2O5-anchored carbon nanotubes for enhanced electrochemical energy storage. *J. Am. Chem. Soc.* 2011, 133, 16291-16299.

243. Nyholm, L.; Nyström, G.; Mihranyan, A.; Strømme, M. Toward flexible polymer and paper-based energy storage devices. *Adv. Mater.* 2011, 23, 3751-3769.

244. Zhou, G. M.; Wang, D. W.; Li, F.; Zhang, L. L.; Li, N.; Wu, Z. S.; Wen, L.; Lu, G. Q.; Cheng, H. M. Graphene-wrapped Fe_3O_4 anode material with improved reversible capacity and cyclic stability for lithium ion batteries. *Chem. Mat.* 2010, 22, 5306-5313.

245. Yu, R. X.; Zhang, C. F.; Meng, Q.; Chen, Z. X.; Liu, H. K.; Guo, Z. P. Facile synthesis of hierarchical networks composed of highly interconnected V_2O_5 nanosheets assembled on carbon nanotubes and their superior lithium storage properties. *ACS Appl. Mater. Interfaces* 2013, 5, 12394-12399.

246. Reddy, A. L. M.; Shaijumon, M. M.; Gowda, S. R.; Ajayan, P. M. Coaxial MnO2/carbon nanotube array electrodes for high-performance lithium batteries. *Nano Lett.* 2009, 9, 1002-1006.

247. Zhou, X. F.; Wang, F.; Zhu, Y. M.; Liu, Z. P. Graphene modified $LiFePO_4$ cathode materials for high power lithium ion batteries. *J. Mater. Chem.* 2011, 21, 3353-3358.

248. Wang, H. L.; Yang, Y.; Liang, Y. Y.; Cui, L. F.; Casalongue, H. S.; Li, Y. G.; Hong, G. S.; Cui, Y.; Dai, H. J. $LiMn_{1-x}FexPO_4$ nanorods grown on graphene sheets for ultrahigh-rate-performance lithium ion batteries. *Angew. Chem.-Int. Edit.* 2011, 50, 7364-7368.

249. Ha, S. H.; Jeong, Y. S.; Lee, Y. J. Free standing reduced graphene oxide film cathodes for lithium ion batteries. *ACS Appl. Mater. Interfaces* 2013, 5, 12295-12303.

250. Schedin, F.; Geim, A. K.; Morozov, S. V.; Hill, E. W.; Blake, P.; Katsnelson, M. I.; Novoselov, K. S. Detection of individual gas molecules adsorbed on graphene. *Nat. Mater.* 2007, 6, 652-655.

251. Jang, S. Y.; Kim, Y. G.; Kim, D. Y.; Kim, H. G.; Jo, S. M. Electrodynamically sprayed thin films of aqueous dispersible graphene nanosheets: highly efficient cathodes for dye-sensitized solar cells. *ACS Appl. Mater. Interfaces* 2012, 4, 3500-3507.

252. Goenka, S.; Sant, V.; Sant, S. Graphene-based nanomaterials for drug delivery and tissue engineering. *J. Control. Release* 2014, 173, 75-88.

253. Yoo, E.; Kim, J.; Hosono, E.; Zhou, H.; Kudo, T.; Honma, I. Large reversible li storage of graphene nanosheet families for use in rechargeable lithium ion batteries. *Nano Lett.* 2008, 8, 2277-2282.

254. Wang, D. H.; Choi, D. W.; Li, J.; Yang, Z. G.; Nie, Z. M.; Kou, R.; Hu, D. H.; Wang, C. M.; Saraf, L. V.; Zhang, J. G.; Aksay, I. A.; Liu, J. Self-assembled TiO_2-graphene hybrid nanostructures for enhanced Li-ion insertion. *ACS Nano* 2009, 3, 907-914.

255. Ji, H. X.; Zhang, L. L.; Pettes, M. T.; Li, H. F.; Chen, S. S.; Shi, L.; Piner, R.; Ruoff, R. S. Ultrathin graphite foam: a three-dimensional conductive network for battery electrodes. *Nano Lett.* 2012, 12, 2446-2451.

256. Stankovich, S.; Dikin, D. A.; Piner, R. D.; Kohlhaas, K. A.; Kleinhammes, A.; Jia, Y.; Wu, Y.; Nguyen, S. T.; Ruoff, R. S. Synthesis of graphene-based nanosheets via chemical reduction of exfoliated graphite oxide. *Carbon* 2007, 45, 1558-1565.

257. Lee, S. W.; Gallant, B. M.; Byon, H. R.; Hammond, P. T.; Shao-Horn, Y. Nanostructured carbon-based electrodes: bridging the gap between thin-film lithium-ion batteries and electrochemical capacitors. *Energy Environ. Sci.* 2011, 4, 1972-1985.

258. Kim, H.; Park, K.-Y.; Hong, J.; Kang, K. All-graphene-battery: bridging the gap between supercapacitors and lithium ion batteries. *Sci. Rep.* 2014, 4.

259. Park, S.; An, J. H.; Jung, I. W.; Piner, R. D.; An, S. J.; Li, X. S.; Velamakanni, A.; Ruoff, R. S. Colloidal suspensions of highly reduced graphene oxide in a wide variety of organic solvents. *Nano Lett.* 2009, 9, 1593-1597.

260. Yang, X. Y.; Dou, X.; Rouhanipour, A.; Zhi, L. J.; Rader, H. J.; Mullen, K. Two-dimensional graphene nanoribbons. *J. Am. Chem. Soc.* 2008, 130, 4216-+.

261. Su, Y.; Gao, X.; Zhao, J. Reaction mechanisms of graphene oxide chemical reduction by sulfur-containing compounds. *Carbon* 2014, 67, 146-155.

262. Li, D.; Muller, M. B.; Gilje, S.; Kaner, R. B.; Wallace, G. G. Processable aqueous dispersions of graphene nanosheets. *Nat. Nanotechnol.* 2008, 3, 101-105.

263. Shao, Y.; Wang, J.; Engelhard, M.; Wang, C.; Lin, Y. Facile and controllable electrochemical reduction of graphene oxide and its applications. *J. Mater. Chem.* 2010, 20, 743-748.

264. Li, D.; Kaner, R. B. Processable stabilizer-free polyaniline nanofiber aqueous colloids. *Chem. Commun.* 2005, 3286-3288.

265. Cheng, F.; Tang, W.; Li, C.; Chen, J.; Liu, H.; Shen, P.; Dou, S. Conducting poly(aniline) nanotubes and nanofibers: controlled synthesis and application in lithium/poly(aniline) rechargeable batteries. *Chem. Eur. J.* 2006, 12, 3082-3088.

266. Taguchi, S.; Tanaka, T. Fibrous polyaniline as positive active material in lithium secondary batteries. *J. Power Sources* 1987, 20, 249-252.

267. Sarker, A. K.; Hong, J. D. electrochemical reduction of ultrathin graphene oxide/polyaniline films for supercapacitor electrodes with a high specific capacitance. *Colloid Surf. A-Physicochem. Eng. Asp.* 2013, 436, 967-974.

268. Shiratori, S. S.; Rubner, M. F. pH-Dependent thickness behavior of sequentially adsorbed layers of weak polyelectrolytes. *Macromolecules* 2000, 33, 4213-4219.

269. Dubas, S. T.; Schlenoff, J. B. Factors controlling the growth of polyelectrolyte multilayers. *Macromolecules* 1999, 32, 8153-8160.

270. Müller, K.; Quinn, J. F.; Johnston, A. P. R.; Becker, M.; Greiner, A.; Caruso, F. Polyelectrolyte functionalization of electrospun fibers. *Chem. Mat.* 2006, 18, 2397-2403.

271. Sung, C.; Hearn, K.; Reid, D. K.; Vidyasagar, A.; Lutkenhaus, J. L. A comparison of thermal transitions in dip- and spray-assisted layer-by-layer assemblies. *Langmuir* 2013, 29, 8907-8913.

272. Lutkenhaus, J. L.; Hrabak, K. D.; McEnnis, K.; Hammond, P. T. Elastomeric flexible free-standing hydrogen-bonded nanoscale assemblies. *J. Am. Chem. Soc.* 2005, 127, 17228-17234.

273. Cho, C. Y.; Valverde, L.; Ozin, G. A.; Zacharia, N. S. Reactive wet stamping for patterning of polyelectrolyte multilayers. *Langmuir* 2010, 26, 13637-13643.

274. Li, X.; Hu, D.; Huang, K.; Yang, C. Hierarchical rough surfaces formed by LBL self-assembly for oil-water separation. *J. Mater. Chem. A* 2014, 2, 11830-11838.

275. Hummers, W. S.; Offeman, R. E. Preparation of graphitic oxide. *J. Am. Chem. Soc.* 1958, 80, 1339-1339.

276. Dresselhaus, M. S.; Jorio, A.; Hofmann, M.; Dresselhaus, G.; Saito, R. Perspectives on carbon nanotubes and graphene Raman spectroscopy. *Nano Lett.* 2010, 10, 751-758.

277. Wang, H. L.; Hao, Q. L.; Yang, X. J.; Lu, L. D.; Wang, X. A nanostructured graphene/polyaniline hybrid material for supercapacitors. *Nanoscale* 2010, 2, 2164-2170.

278. Choi, E. Y.; Han, T. H.; Hong, J. H.; Kim, J. E.; Lee, S. H.; Kim, H. W.; Kim, S. O. Noncovalent functionalization of graphene with end-functional polymers. *J. Mater. Chem.* 2010, 20, 1907-1912.

279. Bak, S. M.; Nam, K. W.; Lee, C. W.; Kim, K. H.; Jung, H. C.; Yang, X. Q.; Kim, K. B. Spinel LiMn2O4/reduced graphene oxide hybrid for high rate lithium ion batteries. *J. Mater. Chem.* 2011, 21, 17309-17315.

280. Che, J. F.; Shen, L. Y.; Xiao, Y. H. A new approach to fabricate graphene nanosheets in organic medium: combination of reduction and dispersion. *J. Mater. Chem.* 2010, 20, 1722-1727.

281. Jeong, H. K.; Lee, Y. P.; Lahaye, R.; Park, M. H.; An, K. H.; Kim, I. J.; Yang, C. W.; Park, C. Y.; Ruoff, R. S.; Lee, Y. H. Evidence of graphitic AB stacking order of graphite oxides. *J. Am. Chem. Soc.* 2008, 130, 1362-1366.

282. Szabó, T.; Berkesi, O.; Forgó, P.; Josepovits, K.; Sanakis, Y.; Petridis, D.; Dékány, I. Evolution of surface functional groups in a series of progressively oxidized graphite oxides. *Chem. Mat.* 2006, 18, 2740-2749.

283. Golczak, S.; Kanciurzewska, A.; Fahlman, M.; Langer, K.; Langer, J. J. Comparative XPS surface study of polyaniline thin films. *Solid State Ionics* 2008, 179, 2234-2239.

284. Jiang, X. Q.; Setodoi, S.; Fukumoto, S.; Imae, I.; Komaguchi, K.; Yano, J.; Mizota, H.; Harima, Y. An easy one-step electrosynthesis of graphene/polyaniline composites and electrochemical capacitor. *Carbon* 2014, 67, 662-672.

285. Jung, I.; Field, D. A.; Clark, N. J.; Zhu, Y. W.; Yang, D. X.; Piner, R. D.; Stankovich, S.; Dikin, D. A.; Geisler, H.; Ventrice, C. A.; Ruoff, R. S. Reduction kinetics of graphene oxide determined by electrical transport measurements and temperature programmed desorption. *J. Phys. Chem. C* 2009, 113, 18480-18486.

286. Ganguly, A.; Sharma, S.; Papakonstantinou, P.; Hamilton, J. Probing the thermal deoxygenation of graphene oxide using high-resolution in situ x-ray-based spectroscopies. *J. Phys. Chem. C* 2011, 115, 17009-17019.

287. Gogotsi, Y.; Simon, P. True performance metrics in electrochemical energy storage. *Science* 2011, 334, 917-918.

288. Jeon, J.-W.; Ma, Y.; Mike, J. F.; Shao, L.; Balbuena, P. B.; Lutkenhaus, J. L. Oxidatively stable polyaniline:polyacid electrodes for electrochemical energy storage. *Phys. Chem. Chem. Phys.* 2013, 15, 9654-9662.

289. Ardizzone, S.; Fregonara, G.; Trasatti, S. Inner and outer active surface of RuO_2 electrodes. *Electrochim. Acta* 1990, 35, 263-267.

290. Frackowiak, E.; Beguin, F. Carbon materials for the electrochemical storage of energy in capacitors. *Carbon* 2001, 39, 937-950.

291. Jeong, H. M.; Lee, J. W.; Shin, W. H.; Choi, Y. J.; Shin, H. J.; Kang, J. K.; Choi, J. W. Nitrogen-doped graphene for high-performance ultracapacitors and the importance of nitrogen-doped sites at basal planes. *Nano Lett.* 2011, 11, 2472-2477.

292. Chen, L. F.; Zhang, X. D.; Liang, H. W.; Kong, M. G.; Guan, Q. F.; Chen, P.; Wu, Z. Y.; Yu, S. H. Synthesis of nitrogen-doped porous carbon nanofibers as an efficient electrode material for supercapacitors. *ACS Nano* 2012, 6, 7092.

293. Wen, Z. H.; Wang, X. C.; Mao, S.; Bo, Z.; Kim, H.; Cui, S. M.; Lu, G. H.; Feng, X. L.; Chen, J. H. Crumpled nitrogen-doped graphene nanosheets with ultrahigh pore volume for high-performance supercapacitor. *Adv. Mater.* 2012, 24, 5610-5616.

294. Lee, Y. H.; Chang, K. H.; Hu, C. C. Differentiate the pseudocapacitance and double-layer capacitance contributions for nitrogen-doped reduced graphene oxide in acidic and alkaline electrolytes. *J. Power Sources* 2013, 227, 300-308.

295. Nasini, U. B.; Gopal Bairi, V.; Kumar Ramasahayam, S.; Bourdo, S. E.; Viswanathan, T.; Shaikh, A. U. Oxygen reduction reaction studies of phosphorus and nitrogen co-doped mesoporous carbon synthesized via microwave technique. *ChemElectroChem* 2013, n/a-n/a.

296. Hulicova-Jurcakova, D.; Kodama, M.; Shiraishi, S.; Hatori, H.; Zhu, Z. H.; Lu, G. Q. Nitrogen-enriched nonporous carbon electrodes with extraordinary supercapacitance. *Adv. Funct. Mater.* 2009, 19, 1800-1809.

297. Wang, X. R.; Li, X. L.; Zhang, L.; Yoon, Y.; Weber, P. K.; Wang, H. L.; Guo, J.; Dai, H. J. N-doping of graphene through electrothermal reactions with ammonia. *Science* 2009, 324, 768-771.

298. Wei, D.; Liu, Y.; Wang, Y.; Zhang, H.; Huang, L.; Yu, G. Synthesis of N-doped graphene by chemical vapor deposition and its electrical properties. *Nano Lett.* 2009, 9, 1752-1758.

299. Panchokarla, L. S.; Subrahmanyam, K. S.; Saha, S. K.; Govindaraj, A.; Krishnamurthy, H. R.; Waghmare, U. V.; Rao, C. N. R. Synthesis, structure, and properties of boron- and nitrogen-doped graphene. *Adv. Mater.* 2009, 21, 4726-4730.

300. Chen, X. Y.; Xie, D. H.; Chen, C.; Liu, J. W. High-performance supercapacitor based on nitrogen-doped porous carbon derived from zinc(ii)-bis(8-hydroxyquinoline) coordination polymer. *J. Colloid Interf. Sci.* 2013, 393, 241-248.

301. Hulicova, D.; Yamashita, J.; Soneda, Y.; Hatori, H.; Kodama, M. Supercapacitors prepared from melamine-based carbon. *Chem. Mat.* 2005, 17, 1241-1247.

302. Beguin, F.; Szostak, K.; Lota, G.; Frackowiak, E. A self-supporting electrode for supercapacitors prepared by one-step pyrolysis of carbon nanotube/polyacrylonitrile blends. *Adv. Mater.* 2005, 17, 2380-2384.

303. Zhao, L.; Baccile, N.; Gross, S.; Zhang, Y. J.; Wei, W.; Sun, Y. H.; Antonietti, M.; Titirici, M. M. Sustainable nitrogen-doped carbonaceous materials from biomass derivatives. *Carbon* 2010, 48, 3778-3787.

304. Zhao, L.; Fan, L. Z.; Zhou, M. Q.; Guan, H.; Qiao, S. Y.; Antonietti, M.; Titirici, M. M. Nitrogen-containing hydrothermal carbons with superior performance in supercapacitors. *Adv. Mater.* 2010, 22, 5202-5206.

305. Kucinska, A.; Cyganiuk, A.; Lukaszewicz, J. P. A microporous and high surface area active carbon obtained by the heat-treatment of chitosan. *Carbon* 2012, 50, 3098-3101.

306. Olejniczak, A.; Lezanska, M.; Wloch, J.; Kucinska, A.; Lukaszewicz, J. P. Novel nitrogen-containing mesoporous carbons prepared from chitosan. *J. Mater. Chem. A* 2013, 1, 8961-8967.

307. Li, Z.; Xu, Z. W.; Tan, X. H.; Wang, H. L.; Holt, C. M. B.; Stephenson, T.; Olsen, B. C.; Mitlin, D. Mesoporous nitrogen-rich carbons derived from protein for ultra-high capacity battery anodes and supercapacitors. *Energy Environ. Sci.* 2013, 6, 871.

308. Zhu, X.; Hillesheim, P. C.; Mahurin, S. M.; Wang, C. M.; Tian, C. C.; Brown, S.; Luo, H. M.; Veith, G. M.; Han, K. S.; Hagaman, E. W.; Liu, H. L.; Dai, S. Efficient CO_2 capture by porous, nitrogen-doped carbonaceous adsorbents derived from task-specific ionic liquids. *ChemSusChem* 2012, 5, 1912-1917.

309. Lee, J. S.; Wang, X. Q.; Luo, H. M.; Dai, S. Fluidic carbon precursors for formation of functional carbon under ambient pressure based on ionic liquids. *Adv. Mater.* 2010, 22, 1004-1007.

310. Lee, J. S.; Wang, X. Q.; Luo, H. M.; Baker, G. A.; Dai, S. Facile ionothermal synthesis of microporous and mesoporous carbons from task specific ionic liquids. *J. Am. Chem. Soc.* 2009, 131, 4596-4597.

311. Fulvio, P. F.; Hillesheim, P. C.; Oyola, Y.; Mahurin, S. M.; Veith, G. M.; Dai, S. A new family of fluidic precursors for the self-templated synthesis of hierarchical nanoporous carbons. *Chem. Commun.* 2013, 49, 7289-7291.

312. Yuan, J.; Marquez, A. G.; Reinacher, J.; Giordano, C.; Janek, J.; Antonietti, M. Nitrogen-doped carbon fibers and membranes by carbonization of electrospun poly(ionic liquid)s. *Polym. Chem.* 2011, 2, 1654-1657.

313. Zhao, Q.; Fellinger, T. P.; Antonietti, M.; Yuan, J. Y. A novel polymeric precursor for micro/mesoporous nitrogen-doped carbons. *J. Mater. Chem. A* 2013, 1, 5113-5120.

314. Fei, Z. F.; Zhao, D. B.; Pieraccini, D.; Ang, W. H.; Geldbach, T. J.; Scopelliti, R.; Chiappe, C.; Dyson, P. J. Development of nitrile-functionalized ionic liquids for c-c coupling reactions: implication of carbene and nanoparticle catalysts. *Organometallics* 2007, 26, 1588-1598.

315. Fei, Z.; Geldbach, T. J.; Zhao, D.; Dyson, P. J. From dysfunction to bis-function: on the design and applications of functionalised ionic liquids. *Chem. Eur. J.* 2006, 12, 2122-2130.

316. Li, S.-L.; Xu, Q. Metal-organic frameworks as platforms for clean energy. *Energy Environ. Sci.* 2013, 6, 1656-1683.

317. Chaikittisilp, W.; Hu, M.; Wang, H. J.; Huang, H. S.; Fujita, T.; Wu, K. C. W.; Chen, L. C.; Yamauchi, Y.; Ariga, K. Nanoporous carbons through direct carbonization of a zeolitic imidazolate framework for supercapacitor electrodes. *Chem. Commun.* 2012, 48, 7259-7261.

318. Xu, G.; Ding, B.; Shen, L.; Nie, P.; Han, J.; Zhang, X. Sulfur embedded in metal organic framework-derived hierarchically porous carbon nanoplates for high performance lithium-sulfur battery. *J. Mater. Chem. A* 2013, 1, 4490-4496.

319. Amali, A. J.; Sun, J.-K.; Xu, Q. From assembled metal-organic framework nanoparticles to hierarchically porous carbon for electrochemical energy storage. *Chem. Commun.* 2014, 50, 1519-1522.

320. Yang, S. J.; Kim, T.; Im, J. H.; Kim, Y. S.; Lee, K.; Jung, H.; Park, C. R. MOF-derived hierarchically porous carbon with exceptional porosity and hydrogen storage capacity. *Chem. Mat.* 2012, 24, 464-470.

321. Zhao, X.; Zhang, L. L.; Murali, S.; Stoller, M. D.; Zhang, Q. H.; Zhu, Y. W.; Ruoff, R. S. Incorporation of manganese dioxide within ultraporous activated graphene for high-performance electrochemical capacitors. *ACS Nano* 2012, 6, 5404-5412.

322. Bao, L. H.; Zang, J. F.; Li, X. D. Flexible Zn_2SnO_4/MnO_2 core/shell nanocable-carbon microfiber hybrid composites for high-performance supercapacitor electrodes. *Nano Lett.* 2011, 11, 1215-1220.

323. Stoller, M. D.; Ruoff, R. S. Best practice methods for determining an electrode material's performance for ultracapacitors. *Energy Environ. Sci.* 2010, 3, 1294-1301.

324. Nune, S. K.; Thallapally, P. K.; Dohnalkova, A.; Wang, C. M.; Liu, J.; Exarhos, G. J. Synthesis and properties of nano zeolitic imidazolate frameworks. *Chem. Commun.* 2010, 46, 4878-4880.

325. Ranocchiari, M.; van Bokhoven, J. A. Catalysis by metal-organic frameworks: fundamentals and opportunities. *Phys. Chem. Chem. Phys.* 2011, 13, 6388-6396.

326. Li, B. Y.; Yang, X. J.; Xia, L. L.; Majeed, M. I.; Tan, B. Hollow microporous organic capsules. *Sci. Rep-UK* 2013, 3.

327. Sing, K. S. W.; Everett, D. H.; Haul, R. A. W.; Moscou, L.; Pierotti, R. A.; Rouquerol, J.; Siemieniewska, T. Reporting physisorption data for gas soild systems with special reference to the determination of surface-area and porosity (recommendations 1984). *Pure Appl. Chem.* 1985, 57, 603-619.

328. Wang, G.; Dong, Q.; Ling, Z.; Pan, C.; Yu, C.; Qiu, J. S. Hierarchical activated carbon nanofiber webs with tuned structure fabricated by electrospinning for capacitive deionization. *J. Mater. Chem.* 2012, 22, 21819-21823.

329. Zhang, P.; Sun, F.; Xiang, Z.; Shen, Z.; Yun, J.; Cao, D. ZIF-derived in situ nitrogen-doped porous carbons as efficient metal-free electrocatalysts for oxygen reduction reaction. *Energy Environ. Sci.* 2014, 7, 442-450.

330. Eddaoudi, M.; Kim, J.; Rosi, N.; Vodak, D.; Wachter, J.; O'Keeffe, M.; Yaghi, O. M. Systematic design of pore size and functionality in isoreticular MOFs and their application in methane storage. *Science* 2002, 295, 469-472.

331. Khezami, L.; Chetouani, A.; Taouk, B.; Capart, R. Production and characterisation of activated carbon from wood components in powder: cellulose, lignin, xylan. *Powder Technol.* 2005, 157, 48-56.

332. Sharma, R. K.; Wooten, J. B.; Baliga, V. L.; Lin, X. H.; Chan, W. G.; Hajaligol, M. R. Characterization of chars from pyrolysis of lignin. *Fuel* 2004, 83, 1469-1482.

333. Yang, Z.; Guo, J.; Das, S. K.; Yu, Y.; Zhou, Z.; Abruna, H. D.; Archer, L. A. In situ synthesis of lithium sulfide-carbon composites as cathode materials for rechargeable lithium batteries. *J. Mater. Chem. A* 2013, 1, 1433-1440.

334. Sadezky, A.; Muckenhuber, H.; Grothe, H.; Niessner, R.; Poschl, U. Raman micro spectroscopy of soot and related carbonaceous materials: spectral analysis and structural information. *Carbon* 2005, 43, 1731-1742.

335. Kudin, K. N.; Ozbas, B.; Schniepp, H. C.; Prud'homme, R. K.; Aksay, I. A.; Car, R. Raman spectra of graphite oxide and functionalized graphene sheets. *Nano Lett.* 2008, 8, 36-41.

336. Bai, Y. C.; Rakhi, R. B.; Chen, W.; Alshareef, H. N. Effect of pH-induced chemical modification of hydrothermally reduced graphene oxide on supercapacitor performance. *J. Power Sources* 2013, 233, 313-319.

337. Liu, J. W.; Webster, S.; Carroll, D. L. Temperature and flow rate of NH3 effects on nitrogen content and doping environments of carbon nanotubes grown by injection CVD method. *J. Phys. Chem. B* 2005, 109, 15769-15774.

338. Shrestha, S.; Asheghi, S.; Timbro, J.; Mustain, W. E. Temperature controlled surface chemistry of nitrogen-doped mesoporous carbon and its influence on Pt ORR activity. *Appl. Catal. A-Gen* 2013, 464–465, 233-242.

339. Chen, H. C.; Sun, F. G.; Wang, J. T.; Li, W. C.; Qiao, W. M.; Ling, L. C.; Long, D. H. Nitrogen doping effects on the physical and chemical properties of mesoporous carbons. *J. Phys. Chem. C* 2013, 117, 8318-8328.

340. Shen, J. M.; Liu, A. D.; Tu, Y.; Foo, G. S.; Yeo, C. B.; Chan-Park, M. B.; Jiang, R. R.; Chen, Y. How carboxylic groups improve the performance of single-walled carbon nanotube electrochemical capacitors? *Energy Environ. Sci.* 2011, 4, 4220-4229.

341. Rakhi, R. B.; Chen, W.; Cha, D.; Alshareef, H. N. Nanostructured ternary electrodes for energy-storage applications. *Adv Energy Mater* 2012, 2, 381-389.

342. Rakhi, R. B.; Chen, W.; Cha, D. K.; Alshareef, H. N. High performance supercapacitors using metal oxide anchored graphene nanosheet electrodes. *J. Mater. Chem.* 2011, 21, 16197-16204.

343. Shaijumon, M. M.; Ou, F. S.; Ci, L. J.; Ajayan, P. M. Synthesis of hybrid nanowire arrays and their application as high power supercapacitor electrodes. *Chem. Commun.* 2008, 44, 2373-2375.

344. Li, X.; Rong, J.; Wei, B. electrochemical behavior of single-walled carbon nanotube supercapacitors under compressive stress. *ACS Nano* 2010, 4, 6039-6049.

345. Ania, C. O.; Khomenko, V.; Raymundo-Piñero, E.; Parra, J. B.; Béguin, F. The large electrochemical capacitance of microporous doped carbon obtained by using a zeolite template. *Adv. Funct. Mater.* 2007, 17, 1828-1836.

346. Biel, B.; Blase, X.; Triozon, F.; Roche, S. Anomalous doping effects on charge transport in graphene nanoribbons. *Phys. Rev. Lett.* 2009, 102.

347. Hou, J. B.; Shao, Y. Y.; Ellis, M. W.; Moore, R. B.; Yi, B. L. Graphene-based electrochemical energy conversion and storage: fuel cells, supercapacitors and lithium ion batteries. *Phys. Chem. Chem. Phys.* 2011, 13, 15384-15402.

348. Shao, L.; Jeon, J.-W.; Lutkenhaus, J. L. Polyaniline nanofiber/vanadium pentoxide sprayed layer-by-layer electrodes for energy storage. *J. Mater. Chem. A* 2014, 2, 14421-14428.